NTNU – Trondheim
Norwegian University of
Science and Technology

Hydrothermal synthesis of materials for intermediate band solar cells

Ragni Fjellgaard Mikalsen

Chemistry
Submission date: May 2013
Supervisor: Karina Mathisen, IKJ
Co-supervisor: Fride Vullum, IMT

Norwegian University of Science and Technology
Department of Chemistry

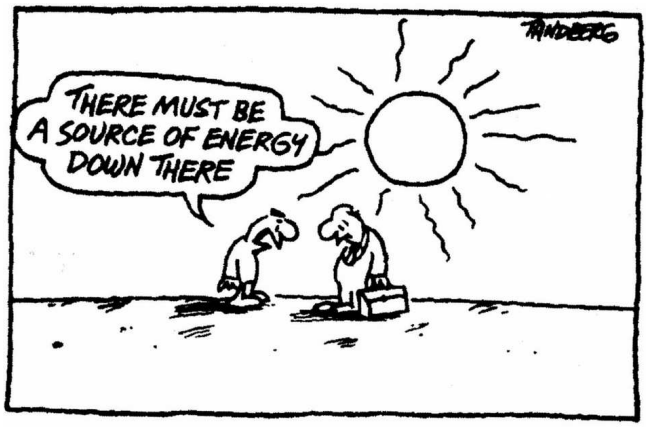

Ron Tandberg, cartoonist

Acknowledgements

The experimental work in this thesis has been carried out at NanoLab at the Norwegian University of Science and Technology (NTNU), Trondheim, Norway. Characterization and other work has been carried out at the Department of Chemistry (IKJ) and at the Department of Materials Science and Engineering (IMT), NTNU.

First, I would like to express my deepest gratitude towards my supervisors Associate Professor Karina Mathisen (IKJ), Associate Professor Fride Vullum-Bruer (IMT) and Senior Researcher Anita Fossdal (SINTEF Materials and Chemistry). Your wise, patient and encouraging guidance has been most appreciated and I could not have completed my thesis without you.

Thanks to Ida Noddeland and the rest of the staff at NTNU Nanolab for listening to my many requests and to Dr. Julian "Jools" Tolchard for the many hours spent teaching me x-ray analysis. To Professor Thor Bernt Melø, Department of Physics, thank you for kindly helping me with reflectance measurements. I also would like to thank members of the two research groups at IKJ and IMT who I have had the privilege of meeting every week. Thea Berg Fines (IKJ) also deserves a big hug for being so helpful, especially during my semester in Zürich.

To my many friends here in Trondheim, back home and abroad- especially "faddergruppe 3", "kveldsmatgjengen" and the people in "lesesalen" and in Überlandstrasse - thank you for being there for me whenever I needed advice, encouragement and a laugh! The many coffee breaks, lunches and "kveldsmat", skiing trips and barbecues (in the rain) have really made these past five years a wonderful time. A special thanks to Kaja and Heidi for proofreading my thesis, to Henrik for being my stand-by technical support with oceans of patience and to Karsten and Thomas for, well, for being you.

I would like to thank my parents, brother and grandparents for supporting me and showing an interest in what I do. Last, but not least I would like to thank my boyfriend Åge. You have been a rock in my life these past six years, and words can not describe how much your support has meant to me. Thank you for your enthusiasm, encouragement, humour and for always saying that it'll all work out in the end.

Abstract

Solar energy is an abundant energy source that may provide an environmentally friendly alternative to fossil fuels. The utilization of the solar energy have so far been limited by various energy losses in the photovoltaic devices. Intermediate band solar cells use a three photon absorption process to take advantage of a larger range of photon energies compared to conventional solar cells, increasing the maximum efficiency of the solar cell. Iron substituted copper gallium disulphide (CGFS) has been proposed as one of the most promising systems, based on efficiency calculations. Recently a CGFS with promising absorption properties has been synthesized, suggesting that an intermediate band may indeed be introduced to the $CuGaS_2$ band gap.

In this thesis, hydrothermal synthesis is used to make a parameter study of the unsubstituted $CuGaS_2$ to optimize the phase purity. Iron substitution into the lattice has been attempted and a preliminary study of the reaction mechanisms has been made. Phase identification of the products has been made using x-ray diffraction (XRD) and the diffractograms have been analysed using Rietveld and Pawley refinements to determine phase composition, lattice parameters and crystallite sizes. The microstructure of the products has been characterized using scanning electron microscopy (SEM), and energy dispersive spectroscopy analysis (EDS) has been used to determine the composition of the different microstructures. Reflectance spectroscopy has been attempted to find absorption properties of the material.

The major findings are that a parameter combination of 200-250 °C reaction temperature, 30 hour reaction time and a copper and gallium precursor concentration of 0.15M or higher gives the most phase pure product of ca. 95 atomic percent $CuGaS_2$. Degree of filling of the autoclave was not found to have a large effect on the product, though extreme fill factors were not tested. It is suggested that the $CuGaS_2$ crystallites grow by a continuous reaction between the precipitated secondary phases and the unreacted precursors in the solution. A reaction temperature above 160 °C or a reaction time over 1 hour is needed for nucleation of $CuGaS_2$. Indications of iron substitution into the $CuGaS_2$ lattice by hydrothermal synthesis were found, which has not been previously reported. The obtained products were not phase pure enough to make accurate refinements on lattice positions.

Sammendrag

Solenergi har blitt foreslått som et miljøvennlig alternativ til fossile brennstoff. Utnyttelsen av sollyset har til nå vært begrenset av ulike energitap i dagens fotovoltaiske enheter. Mellombåndshalvledere utnytter en større andel av solspekteret sammenlignet med konvensjonelle solceller. Dette skjer gjennom absorpsjon av fotoner med flere ulike energier, noe som øker den maksimale effektiviteten til solcellen. Jernsubstituert kobber gallium disulfid (CGFS) er foreslått som en av de mest lovende systemene for mellombåndshalvledere, basert på effektivitetsberegninger. En CGFS med lovende absorpsjonsegenskaper har nylig blitt syntetisert, noe som indikerer at et mellombånd faktisk kan introduseres i båndgapet til $CuGaS_2$.

I denne oppgaven har hydroterm syntese blitt brukt i en parameterstudie av usubstituert $CuGaS_2$ for å optimalisere faserenheten. Jernsubstitusjon har blitt utprøvd, og et introduserende studie av reaksjonsmekanismene i systemet har blitt gjort. Faseindentifikasjon av produktene har blitt undersøkt ved røntgendiffraksjon (XRD) og fasesammensetningen, gitterparametre og krystallstørrelser har blitt undersøkt ved Rietveld og Pawley raffinering. Mikrostrukturen har blitt undersøkt ved elektronmikroskopi (SEM), og sammensetningen av de ulike mikrostrukturene har blitt bestemt ved energidispersiv spektroskopi (EDS). Refleksjons-spektroskopi har blitt brukt i et forsøk på å undersøke absorpsjonsegenskapene til materialet.

De viktigste resultatene viste at parameterkombinasjonen 200-250 °C reaksjonstemperatur, 30 timer reaksjonstid og en forløperkonsentrasjon av kobber og gallium over 0.15 M gir høyeste faserenhet av $CuGaS_2$, rundt 95 atomprosent. Det ble funnet liten effekt av varierende fyllingsgrad av autoklaven, men ekstremt høye fyllingsgrader ble ikke utprøvd. Det foreslås at $CuGaS_2$ krystallene vokser gjennom en kontinuerlig reaksjon mellom utfelte sekundærfaser og ureagerte forløpere i løsningen. En reaksjonstemperatur over 160 °C eller reaksjonstid lengre enn 1 time er nødvendig for korndannelse av $CuGaS_2$. Det ble funnet indikasjoner på at jernsubstitusjon i $CuGaS_2$-gitteret er mulig ved hydroterm syntese, noe som ikke er rapportert tidligere. Høyere faserenhet av produktene er nødvendig for å kunne gjøre nøyaktige beregninger på eventuell jernsubstitusjon.

Abbreviations and symbols

$^{\circ}$C	Degrees Celsius
η	Efficiency of the cell
α	Absorption coefficient (cm^{-1})
δ	Pyrite (FeS_2), in the phase diagram fig. 2.22
η	Pyrrhotite ($Fe_{1-\gamma}S$), in the phase diagram fig. 2.22
μ**m**	Micrometer
$\alpha, \zeta, \gamma, \omega$	Cu:Ga phases, in the phase diagram fig. 2.16
$\alpha_n, \alpha_m, \beta$	Cu:Ga:Fe:S phases, in the phase diagram fig. 2.22
σ_{SL}	Surface tension
ΔG_{nuc}	Nucleation barrier
R^*	Nucleation radii
2θ	Bragg angle in X-ray diffraction
A	Absorbance
AFM	Atomic force microscopy
AM1.5	Air Mass 1.5 irradiation spectrum
BB	Black body
C	Concentration
$\mathbf{C}_{eq}$	Concentration at equilibrium
CB	Conduction band
CGFS	Iron substituted copper gallium disulphide ($CuGaS_2$)
cv	Covellite (CuS)
d	Lattice spacing in crystal
D	Dark background
DFT	Density functional theory
dg	Digenite (Cu_2S)
DOS	Density of states
$\mathbf{E}_H$	Sub-band gap with highest energy
$\mathbf{E}_L$	Sub-band gap with lowest energy
EDS	Energy dispersive X-ray spectroscopy
Eg/ $\mathbf{E}_G$	Band gap
eV	Electron volt
FF	Fill factor in efficiency calculations
gal	Gallite ($CuGaS_2$)
h	Hour
h k l	Miller indices in lattice
$\mathbf{I}_m$	Maximum current of a cell

I_{SC}	Short circuit current
IB	Intermediate band
IBSC	Intermediate band solar cell
IKJ	Department of Chemistry
IMT	Department of Materials Science and Engineering
JCPDS	Joint Commitee on Powder Diffraction Standards
$K_{\alpha 1}$, $K_{\alpha 2}$	Copper X-ray irradiation energies
keV	Kilo electron volt
L	Liquid phase
L-cystine	Organic molecule ($C_6H_{12}N_2O_4S_2$)
Meth.	Method
mL	Milliliter
n- type	Negative type material
nm	Nanometer
NTNU	Norwegian University of Science and Technology
P_m	Output power of the solar cell
P_{sun}	Incoming power of the sun
p- type	Positive type material
PTFE	Polymer Tetrafluoroethylene
QFL	Quantum- Fermi level
R	Reflectance
R*	Critical radii for nucleation
REC	Renewable Energy Corporation
Rwp	R-weighted pattern
S	Reflectance from sample
S_{ref}	Reflectance from white reference
S_{sat}	Level of supersaturation
SEM	Scanning electron microscopy
T	Temperature
Tu	Thiourea ($SC(NH_2)_2$)
UV-vis	Ultraviolet- visible
V	Voltage
V_m	Maximum voltage of a cell
V_{OC}	Open circuit voltage
VB	Valence band
W	Watt
XRD	X-ray diffraction

Contents

1 Introduction

1.1 Motivation

With the world's fossil fuels storages decreasing, there is a need to look forward and find new sources of energy. Solar energy has been proposed as an abundant, environmentally friendly but challenging alternative. Developing new generations of solar cells include increasing the power output, reducing production costs and providing adequate energy storage options.[1]

During the last decades significant developments have been made in the solar energy field, encouraged by the UN, the EU and several international climate organizations.[2,3] Solar cells have yet to be realized as a realistic full-scale alternative to fossil fuels due to many challenges in the field. However, the socio-economical and environmental benefits of taking advantage of the solar energy may make the effort of further development worth while.

1.2 Goal

The main goal of this thesis is develop a hydrothermal synthesis route to make a phase pure iron substituted copper gallium sulfide (Fe:$CuGaS_2$) semiconductor with an intermediate band in the band gap, intended for the application as a third generation solar cell.

This main goal is divided into several minor goals. Firstly is to reproduce an unsubstituted $CuGaS_2$ with 93 at% purity made in the master thesis by Sortland.[4] Secondly a systematic parameter study of an unsubstituted $CuGaS_2$ host will be made targeting a phase pure product. Thirdly iron substitution will be attempted, using the same synthesis procedure as for the unsubstituted host. Various characterization techniques will be applied to attempt to determine whether or not iron is substituted into the lattice, and whether this gave the target intermediate band structure or not. Finally, a parameter study will be done to further optimize the synthesis and obtain preliminary information on the reaction mechanisms in the system.

2 Theory

2.1 Solar cells

2.1.1 History and current status

Since the accidental discovery of the modern silicon based solar cell in the 1940's,[5] great efforts have been made towards utilizing the solar energy. The motivation for developing and improving new energy sources, hereunder biomass, wind, geothermal and solar energy, lies in finding an environmentally friendly, clean alternative to fossil fuels.[2] As the fossil fuels stores have decreased during the 20'th century, the renewable energy industries including the solar cell industry have grown.

Despite the decades passed since their discovery, modern solar cells are far away from exploiting the full potential of the energy of the sun. While being an environmentally friendly source of energy, solar energy is still not an adequately cost-efficient alternative to fossil energy sources, with high costs per kilo watt hour produced.[6]

The photovoltaic industry has long been dominated by silicon based solar cells.[7] As the technology has developed, the cost margins have decreased, which has taken its toll on several solar cell industries worldwide. The Norwegian Renewable Energy Corporation (REC) has recently discontinued all of their Norwegian production,[8] much due to high international competition, and small cost margins. The turmoil in the world's solar cell marked poses many questions regarding the sustainability of the industry.

Future continuation of the solar cell industry, nationally and internationally, will depend heavily on the development of technologies for more cost efficient solar cells. Some of the main challenges in the solar industry lie in the development of technologies to give a lower cost to power output ratio, including materials for energy conversion and for harvesting the photons from the sun.[9]

2.1.2 Working principle and design

To understand how the development of better solar cells may be done an introduction to the working principle and design of a solar cell will be given. A conventional solar cell consists of a single junction semiconductor with a given band gap.[1] The semiconductor absorbs photons with energy equal to or greater than the band gap. For every absorbed photon an electron is excited from the valence band to the conduction band of the semiconductor, giving an excited

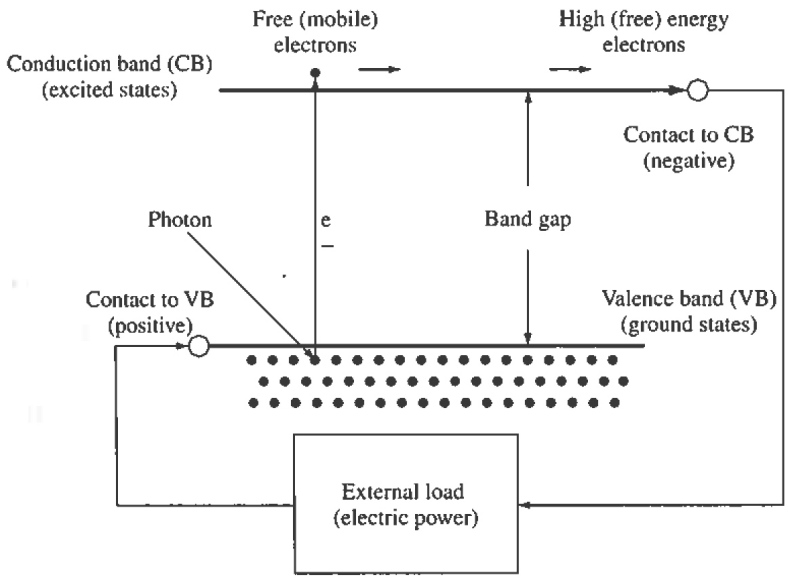

Figure 2.1: The basic principle of photon absorption in a conventional solar cell device.[1]

electron in the conduction band and a positive hole in the valence band, as shown in figure 2.1.

Efficient electron and hole separation is important for the performance of the cell. To avoid recombination of the two the semiconductor is sandwiched between a material of n-type (excess of free electrons) and of p-type (excess of free holes), providing a junction where electrons and holes separate spontaneously. The electrons in the conduction band will wander towards the negative n-type material and the holes in the valence band will wander towards the positive p-type material. The charge carriers are collected through electronically conducting contacts and this constitutes the electric current produced by the solar cell.[1] In conventional solar cells the pn-materials often function as contacts, and their electrochemical potentials are tailored for the selective collection of charge carriers.[10]

The external electric current may be used right away or be collected and stored. When the extra potential energy of the excited electrons has been used

to perform work the electron is restored to its original position in the valence band, ready to absorb another photon.

One of the major energy loss challenges in this circle is recombination of electron and hole. This occurs when an excited electron relaxes back to the valence band instead of wandering to the contacts, leaving the system with no external electric current. There are two modes of recombination: radiative and non-radiative.

Radiative recombination is the release of excess energy through the emission of photons. Radiative recombinations are electronic transitions between delocalized states in the semiconductor lattice, for example direct relaxation from the conduction band to the valence band. As photon absorption is a process that occurs simultaneously to photon emission, this process can not be avoided, even in perfect materials.[11]

Non-radiative recombination is in most cases the release of energy as heat via a multi-phonon release mechanism in the lattice[10] called a Shockley-Read-Hall recombination.[12] Because it most likely occurs for electronic transitions from a delocalized state to a localized state, this type of recombination is strongly related to imperfections in the lattice, as imperfections represent localized states.[10] To avoid non-radiative recombination, it is important to avoid states that have localized wavefunctions, which can be obtained by making defect free semiconductors.[12] The design of a traditional solar cell should thus include a close to defect-free single crystalline semiconductor.

To make a traditional solar cell, the semiconductor is cut into wafers and is sandwiched between a pn-junction and connected to contacts at both ends. To maximize the area exposed to sunlight the contacts at the front of the solar cell is often designed as a grid, instead of as a plate. The reason is that most conventional contacts are metallic and would reflect too much of the sunlight had they been larger. To further avoid reflecting the sunlight, an antireflecting layer is often placed beneath the front contact, and is why conventional solar cells appear blue. The silicon wafers themselves are grey. The layout of a conventional solar cell is illustrated in figure 2.2.

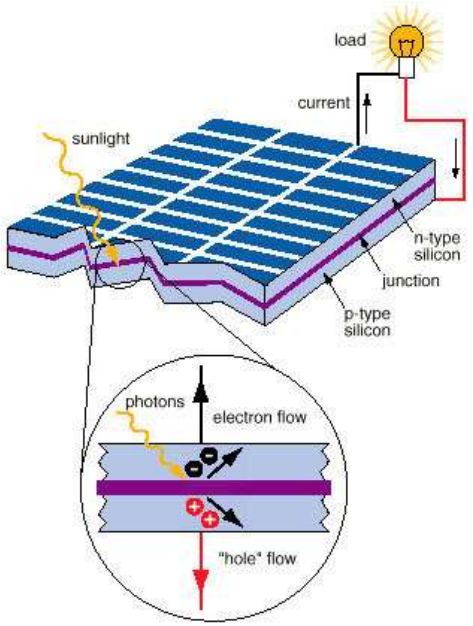

Figure 2.2: Design and working principle of a coventional solar cell. The junction where the p-type and n-type silicon meet is enlarged. The top contact of the cell is a metal grid, with a blue antireflecting coating underneath.[13]

2.1.3 Efficiency calculations

An ideal solar cell produce as much electric power per incoming photon as possible. To enable comparison of different solar cell technologies it is important to have a common basis for comparison. One way to compare solar cells is to calculate and compare their efficiencies. One of the most common efficiency model used is based on the principle of detailed balance by Boltzman. This states that "At equilibrium, each elementary process should be equilibrated by its reverse process".[14]

The scientific community uses these efficiency calculations as a measure of their performance in a worldwide context. Solar cell efficiency records are announced annually and are important to motivate further research. For each improvement of the efficiency, a more thorough understanding of the mechanisms in the system is made.[15]

A short introduction to efficiency calculations based on the detailed balance principles will be given to enable the reader to distinguish between different approaches.

In a solar cell the charge separation of the electron and hole creates a chemical potential gradient across the cell. The chemical potential difference is represented by the voltage, often called photovoltage of the cell,[11] which drives the current. The power delivered by the cell is given by the product of the current and the voltage of the cell. A current-voltage plot, see figure 2.3, can be used to optimize the operation point of a cell to the point where the cell gives the most power per incoming photon. In equation (1) the short circuit current (I_{SC}) and the open circuit voltage (V_{OC}) are compared to the maximum current (I_m) and voltage (V_m) of the cell.[13] The relation gives the Fill Factor (FF), which is ideally 1.

$$FF = \frac{V_m I_m}{V_{OC} I_{SC}} \tag{1}$$

$$\eta = \frac{P_m}{P_{sun}} = \frac{V_m I_m}{P_{sun}} = FF \frac{V_{OC} I_{SC}}{P_{sun}} \tag{2}$$

The efficiency of the solar cell is calculated using the Fill Factor, see equation (2). P_{sun} represents the incoming power from the sun, and P_m represents the maximum delivered electric power of the cell. The efficiency of a solar cell is defined as the fraction of the incoming photons that the cell absorbs and converts into electric power. The efficiency can never be 100 % due to the unavoidable radiative recombinations as described in section 2.1.2.

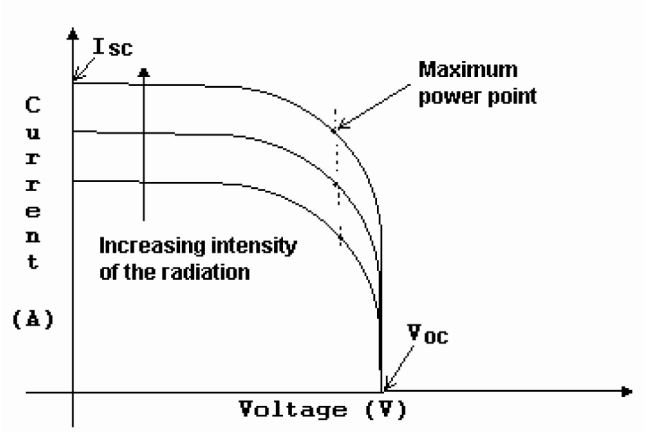

Figure 2.3: The current- voltage plot for a solar cell.[13]

The efficiency of a solar cell is mainly determined by the band structure of the semiconductor, as the size of the band gap corresponds to the photovoltage used in the efficiency calculations. For a given band gap, the calculated efficiency may vary depending on the calculation parameters used. The most important calculation parameter to be aware of is the light concentration used. This is most commonly set to either full sun irradiation (46050 suns) or 1 sun.[16] The nature of the irradiation accounted for in the calculations must also be considered, since there is a difference between black body irradiation and the spectrum that arrives at earth. For the latter, standards such as the Air-Mass-1.5 (AM1.5) is often used.[17] The chosen temperature of the sun and the temperature of the cell, usually set to 6000 K and 300 K respectively, will also affect the efficiency calculated. Other factors that affect the efficiency calculations is to what extent non-radiative recombination and absorption coefficient overlap is accounted for.[18] Naturally, a comparison of different efficiencies should be based on the same parameters.

2.2 Increasing the efficiency

For single junction silicon solar cells the maximum theoretical efficiency, called the Shockley-Queisser limit, is 41 %.[19] * The low efficiency is due to the high

*For full sun irradiation of 46050 suns. The number is 33% for 1 sun irradiation.

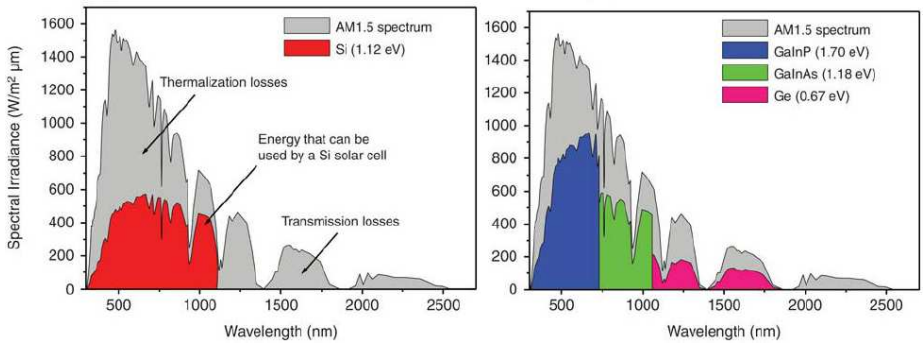

Figure 2.4: Comparison of the spectral match of the solar spectrum and a first generation silicon based single junction solar cell (left) and a third generation multijunction solar cell (right).[13]

spectral mismatch between photons from the sun and the band gap of silicon,[6] given in figure 2.4. The spectral mismatch causes the majority of the solar energy to be lost.

Low maximum efficiency limits combined with relatively high cost of conventional silicon solar cells makes it clear that an alternative is desirable.[6,20] Different approaches to deal with the problem have been categorized into different generations of solar cells, following the silicon-based first generation.

The cost efficiency of a conventional solar cell may be improved by decreasing the production costs per cell, an approach that has been named second generation solar cells. Here, the solar cells consists of low-price materials such as polymers. Their main disadvantage is that the materials used have very low efficiencies.[21]

Another alternative is to make solar cells with a higher theoretical maximal efficiency limit than that of conventional single-junction silicon solar cell, meaning that more of the photon energy normally lost to heat is converted into usable free energy.[22] Any solar cell that meet this requirement is called a third generation solar cell.[1] An example of the improved spectral match of a third generation solar cell is shown in figure 2.4. Due to higher efficiency, less material is needed for every energy unit the cell produce, which in turn reduces the material costs per area unit of the cell. A comparison of the efficiency limit and material costs of the different generations of solar cells is given in figure 2.5.

To make a third generation solar cell, a larger percentage of the solar spectrum must be utilized. This can be done in two ways; by adapting the incoming

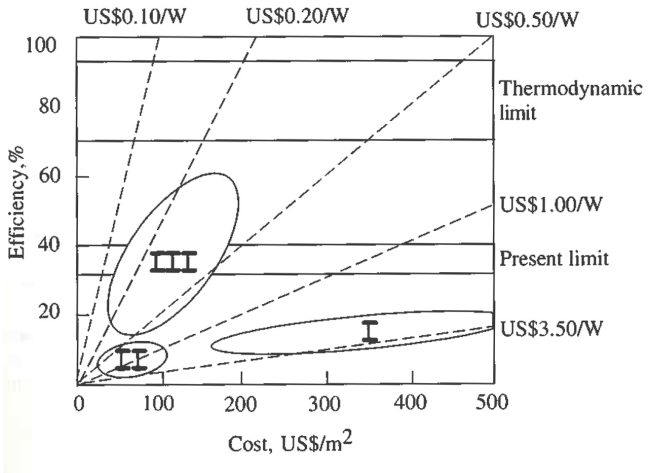

Figure 2.5: An overview of the differences between first, second and third generation solar cells. It is seen that 3. generation solar cells have low costs and high efficiencies, as opposed to 1. generation solar cells.[21]

photons from the sun or by adapting the solar cell itself.[6] Adapting the sun irradiation to better fit the electronic structure of a solar cell will include a narrowing of the solar spectrum to decrease the spectral mismatch. Doing the opposite will allow the solar panel itself to be well matched to the natural sun irradiation.[21] Research is currently being done in both areas, this thesis will focus on the latter approach.

Modifying the solar cell can include changing the layout of the cell, modifying the semiconductor, or a combination of the two. Both are aiming for a better spectral match, so that the solar cell can absorb a larger percentage of the solar energy. The layout of the cell may be altered by stacking solar cells of different absorption ranges, creating a tandem cell[23] that absorbs a broader energy range than single cells would.

Much solar cell research has been made in the field of developing a material that can do what a tandem cell can in a single cell. This would give less loss of energy to the heterojunctions between the cells,[21] as well as a lower overall material cost. The band structure of the semiconductor must facilitate absorption of a large energy range of photons, at the same time as the materials used must be available and preferably low-cost. Many suggestions have been

made, one of the most promising solutions is the intermediate band solar cell.[1]

2.3 Intermediate Band Solar Cells

2.3.1 History and current status

When intermediate band solar cells (IBSC) were first suggested in the 1960's, the idea was rejected as it was believed that the efficiency of such a device would be strongly limited by non-radiative recombination.[12] The concept was re-introduced in the late 1990's by Luque and Marti,[24] with a detailed efficiency model suggesting that the efficiencies limits could indeed exceed the Schockley-Queisser limit of 41 %, and reach up to 63 % utilization of the sunlight [†]. The group suggested a design of such a cell in 2001,[25] and in the following decade several groups worked on finding and making suitable materials.

Calculations have been made to determine the ideal electronic structure of an intermediate band material. Several III-V semiconductors showed potential for IB use.[26] Experimental approaches have also been made. The first proof of concept IBSC was synthesized in 2008,[27] giving an intermediate band solar cell consisting of vanadium subsidized indium sulphide. The cell absorbed across the full solar spectrum and is still one of the most promising approaches in the field,[12] despite having efficiencies well under 1 %.

Later, several other materials have been used to make intermediate band solar cells, but the development of suitable materials has proven to be far from trivial.[10] The efficiencies still remain inadequate for commercial use, with a record efficiency of around 1 %.[28] When comparing this to the best silicon based solar cells on the marked with around 17 % efficiency, and laboratory records in the mid-20 % range, it is important to remember that the silicon industry has had a good 60 years to develop.[12]

The decade spent researching the concept has increased our knowledge in the field substantially, and a continued development of suitable materials may lead to intermediate band solar cells with efficiencies much higher than the currently commercially available silicon solar cells.[10]

2.3.2 Working principle and design

The intermediate band concept is based on an alteration of the electronic structure of a semiconductor, by introducing a partially filled intermediate band to

[†]These efficiencies are based on isotropic black body, full-sun illumination (46050 suns concentration), supressed non-radiative recombination, infinite carrier mobilities (no ohmic losses), a solar temperature of 6000 K, and a cell temperautre of 300 K.[10,24]

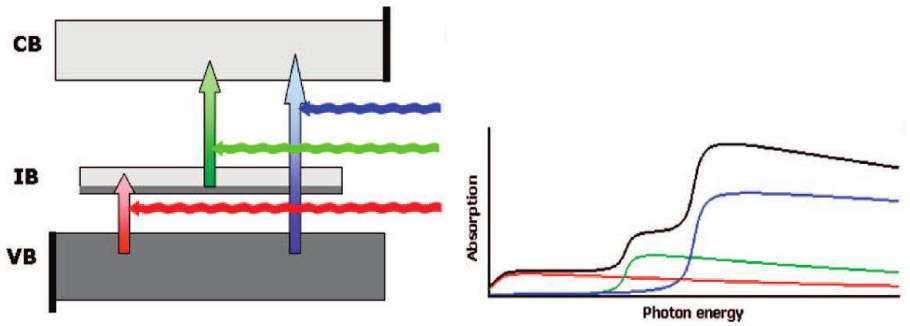

(a) (b)

Figure 2.6: 2.6(a): The working principle of an intermediate band semiconductor, photons excite electrons from the valence band (VB) to the conduction band (CB) and to the intermediate band (IB), as well as from IB to CB. 2.6(b): Illustration of the absorbance spectrum of an intermediate band solar cell.[27]

the band gap[24,25,29] presented in figure 2.6(a). This divides the band gap into smaller energy units, sub-band gaps. The intermediate band acts as a "stepping stone"[30] for low-energy photons. The semi-filled intermediate band will function as an electron receiver as well as an electron supplier.[31] The absorption spectrum of an intermediate band solar cell will therefore ideally include one absorption of energy equal to the band gap, in addition to two sub-band gap absorptions, illustrated in figure 2.6(b).[31]

The electronic structure of an IBSC will in other words allow absorption of three photon at the same time. A larger range of the solar spectrum will thus be utilized compared to conventional solar cells, as illustrated in figure 2.7. The multi-absorption creates more free electron and hole pairs available for increasing the electric current without lowering the voltage of the cell.[27,30] As a result the efficiency of the cell increases due to the augmented energy output per unit of incoming radiation.

The energy density state in the band gap introduced by the intermediate band is large enough to alter the Fermi state of the host semiconductor. This creates several quasi-Fermi levels when illuminated,[25,33] shown in figure 2.8. The figure also shows that the design of an intermediate band solar cell is similar to a conventional cell, with the IB material sandwiched between an n-and a p-type material.[12,25]

The intermediate band is considered to be truly delocalized from the valence

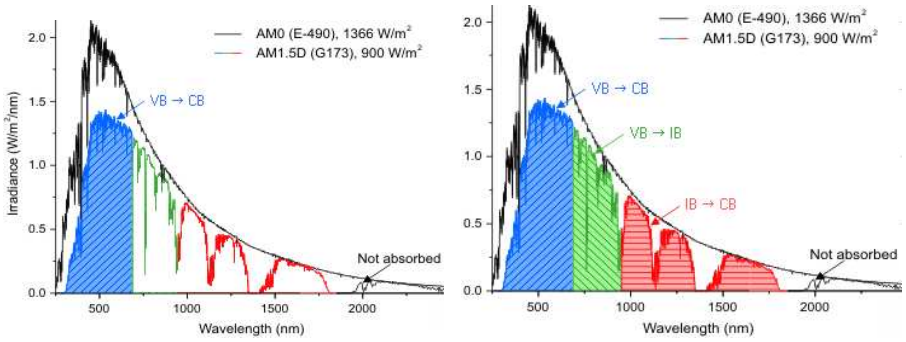

(a) (b)

Figure 2.7: 2.7(a): Spectral match of the solar spectrum and the absorption of a broad band gap semiconductor. 2.7(b): Spectral match of the solar spectrum and the absorption of a broad band gap and two sub- bandgap, due to an intermediate band (IB). Both figures are from SUBLAB laboratory,[32] modified by Sortland.[4]

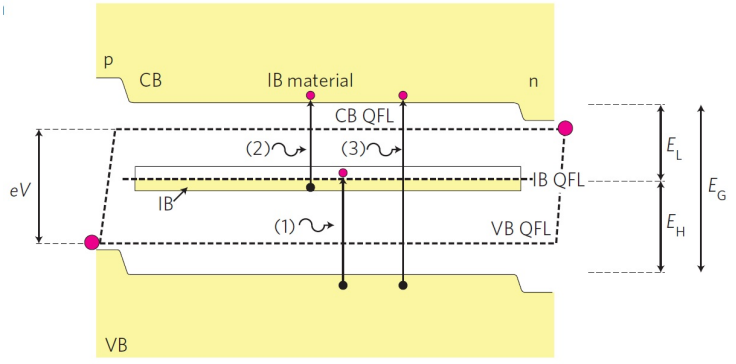

Figure 2.8: The electronic structure and design of an intermediate band solar cell. Quasi fermi levels, excitation of three photoelectrons and the design of the cell is shown.[12]

and conduction band due to the splitting of the Fermi levels.[27] This means that the three electronic transitions can mathematically be considered as separate excitations across a band gap.[34] An intermediate band must not be confused with a donor or acceptor band, as these are narrow density states that are not considered as truly delocalized. The IB is located almost equidistant to the CB and VB, while donor and acceptor bands are located very close to the VB or CB respectively.

The delocalized nature of the intermediate band is important for the performance of the solar cell. As previously described, electronic transitions between delocalized and localized states in the lattice induces non-radiative recombination, lowering the overall efficiency of the cell. Transitions between delocalized states, however, will not. Here lies the key in avoiding non-radiative recombination efficiency losses; having an intermediate band with a delocalized wavefunction.[24,27,31]

There have been two main approaches to making a material with this delocalized intermediate band electronic structure. The first is to introduce quantum dots to a semiconductor host lattice,[10] presented in figure 2.9. The quantum dots represent confined energy states in the lattice with different electronic structure than the host. For a sufficient amount of the right sized dots in the lattice, the overall electronic structure of the system can be altered to an intermediate band structure.[35] The quantum dot approach is the most well-known method for making IB materials, but the technique has major disadvantages such as major thermal losses.[36] The loss mechanisms are linked to the build-up of a quantum dot solar cell. The quantum dots represent recombination centres for electrons and holes in the lattice,[10,12] since they are incorporated in layers of the host structure.

The thermal losses can be avoided by lowering the temperature of the cell, but this will be impractical as solar cells should work at ambient temperatures. Another challenge is the mismatch between the dots and the host lattice, causing major strain issues as the thickness of the films used increases. Another disadvantage of the layout is the expensive physical equipment necessary for making a layered host/ quantum dot structure.

The second and less investigated approach is often called "bulk intermediate band materials", using that a material is synthesized naturally containing the intermediate band electronic structure.[12,30] This has several advantages compared to the more studied quantum dot approach. As the electronic structure is constant for the bulk material, there is no need for microstructuring of the material and less expensive synthesis techniques may be used. Lattice strains from lattice parameter mismatch are also avoided.

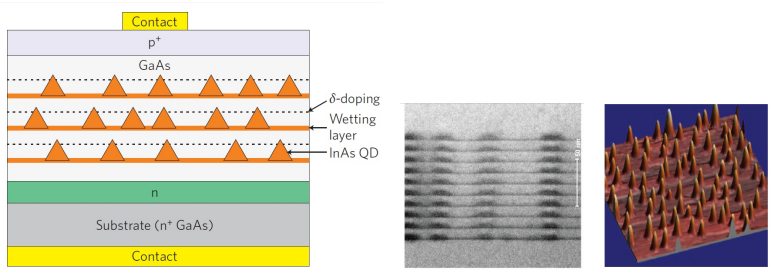

(a) (b) (c)

Figure 2.9: The design of a quantum dot solar cell. 2.9(a): Schematic overview of the design. 2.9(b): SEM image of a cross section of the cell. 2.9(c): AFM image of the InAs quantum dots.[12]

The bulk intermediate band materials are made by introducing impurities of transition metal ions to a broad band gap semiconductor. The impurity level needed is governed by the amount needed to delocalize the density of states of the intermediate band. According to Luque et al.[37] this usually lies in the range of a few percent impurity, or an impurity concentration around $10^{21}/cm^3$.

Substituting such a high amount of the lattice ions with transition metal ions is the key in avoiding impurity recombination centres in the lattice. At high substitution levels, the wave function of the impurity states is delocalized and thermal losses can consequently be avoided to a greater extent.[10]

Several attempts have been made at making bulk intermediate band cells, but so far all cells have had very low efficiencies.[30] These first attempts have been unoptimized systems, made for investigating if the IB concept is possible to synthesize.[27] The main challenge ahead lie in finding suitable materials with high theoretical efficiencies and optimizing the synthesis routes of these to approach this limit.

2.3.3 Ideal band structure

Finding a combination of host semiconductor and impurity transition metal with a suitable electronic structure is important for the intermediate band concept. The type of impurity will determine the position of the impurity contribution to the host electronic structure. Only when the impurity states are located within the band gap, can an intermediate band be formed.

The intermediate band should be introduced to a broad band gap semicon-

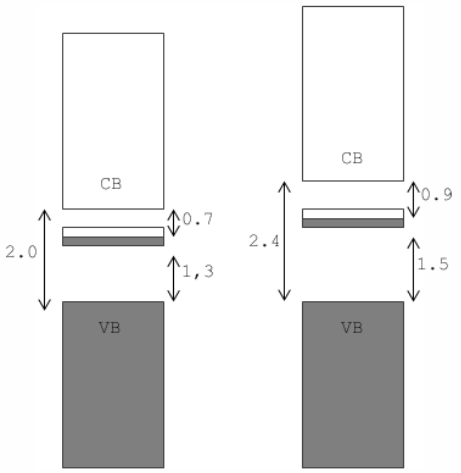

Figure 2.10: Ideal band structure of an intermediate band semiconductor, calculated for full sun irradiation (left) and 1 sun irradiation (right).

ductor. A wide band gap is necessary for the smaller sub-band gaps to still be able to absorb photons in the part of the solar spectrum most densly populated by photons. Ideally, the intermediate band is not located equidistant to the VB and CB, enabling absorption of two low-energy photons with different energies.

The calculated ideal band structure for an IBSC is a band gap of 2.4 eV, with an intermediate band located 0.92 eV from the host band edges [‡].[16] The ideal band structure is illustrated in figure 2.10. As can be seen from the figure, the intermediate band is located closest to the conduction band, which has been calculated to be the best configuration for avoiding undesireable band overlap.[31] The performance of the cell is also affected by the filling of the IB, the optimal is to have a partial filling of the band.[38]

The current-voltage plot for an intermediate band solar cell (IBSC) compared to a conventional solar cell is given in figure 2.11. It is seen that the cell current is higher for the IBSC, due to an increased number of charge carriers. This increases the fill factor of the IBSC, giving a higher ideal efficiency of the IBSC compared to the conventional single gap solar cell.

To sum up, there are many requirements that a material for intermediate

[‡]For 1 sun irradiation. The full sun (46050 suns) equivalent is 1.95 eV band gap, and IB located 0.71 eV from the band edge.[12]

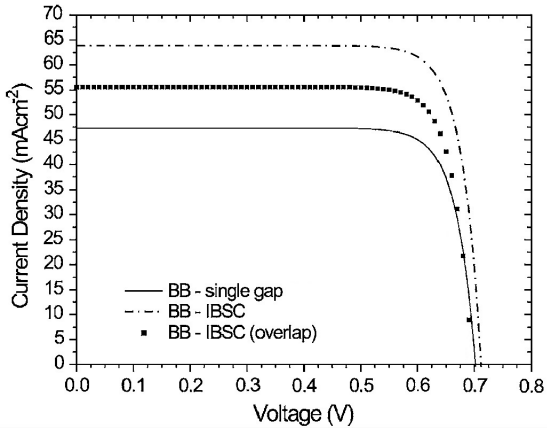

Figure 2.11: The current voltage plot for conventional silicon based solar cells (whole line) and intermediate band solar cells (IBSC) (dashed lines). The two lines for IB cells represent different degrees of absorption coefficient overlap in the calculations, the most realistic being the darkest with some overlap. The calculations are based on black body (BB) illumination. The figure is adapted with modifications from Marti et al.[16]

band solar cells must meet. The most important requirement is choosing suitable host material and impurity.

2.3.4 Chalcogenides as host semiconductors

Chalcogenides are a well-studied group of materials that possesses the important broad band gap electronic structure needed in intermediate band solar cells. Several types of chalcogenides are already implemented in the solar cell industry,[35,39] and have proved to be a cost-efficient alternative to the traditional silicon single crystalline solar cells.[7] Chalcogenides have been proposed as possible host materials for IB materials.[40]

A chalcogenide is composed of a chalcogen (S, Se, Te) and at least one positive ion tetrahedrally coordinated to the chalcogen.[41] The electronic structure of the chalcogenides includes a direct band gap of varying size depending on the composition. Tailoring electronic structure with composition may be beneficial for solar applications.[42]

The most well-known chalcogenide systems are the I-III-VI_2 ternary chalcogenides.[43] Of these, the efficiency record holding[15,20] $Cu(In_xGa_{1-x})(Se_yS_{1-y})$

with $0 \leq x, y \leq 1$ have been suggested as promising host materials for intermediate band semiconductors.[35,44]

When calculating efficiencies for IB materials the the impurity type is not considered, as these represent separate Fermi levels in the structure.[31] Figure 2.12 shows the theoretical efficiency calculations done to identify the ternary Cu-chalcogenide with the optimal band structure. It can be seen that the copper gallium disulfide ($CuGaS_2$) semiconductor comes closest to the efficiency limit, and has been suggested as the best host for intermediate band semiconductors.[33,40]

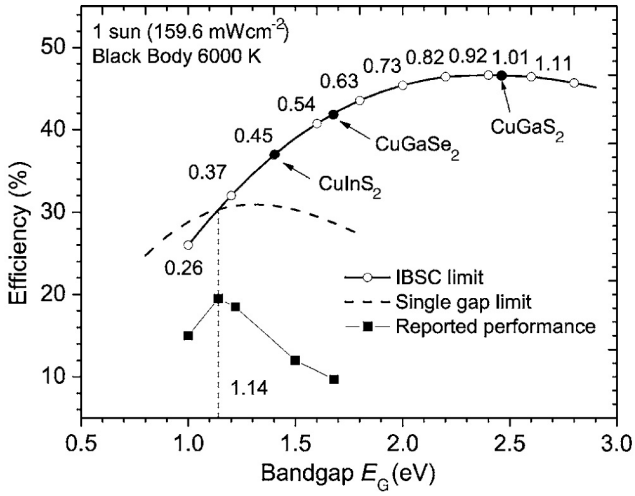

Figure 2.12: Calculations showing how different choices of host material will affect the efficiency of an intermediate band semiconductor. Selected ternary chalcogenides with different band gaps are compared.[16]

In addition to having the highest efficiency, $CuGaS_2$ has several other advantages. Gallium is less toxic and much more abundant in the earth's crust than Indium, by two orders of magnitude.[9] Sulfur is opposed to the toxic Selenium, non-toxic.[42]

$CuGaS_2$ is the first semiconductor to be suggested for combining the IB concept with thin film technology[44] which probably is because it has the lowest lattice mismatch of the chalcopyrites with the relatively cheap and common silicon (111) substrate.[39,42] For this reason, $CuGaS_2$ is compatible for epitaxial growth of thin films on silicon wafers.

It should be noted though that there are challenges connected to the use of chalcogenides, including $CuGaS_2$. One of the major challenges is that they naturally contain many defects,[35] which is unfavourable for electric currents in the cell. The same is the heterojunction between substrate and thin film, which represents a recombination centre.[45] In chalcopyrite cells light is mainly absorbed near the surface due to their high absorption coefficient,[46] making the cells highly sensitive to surface modifications. Production challenges include up-scaling, long term stability and reproducibility.[47]

2.3.5 $CuGaS_2$; structure and properties

$CuGaS_2$ is an intrinsic p-type semiconductor.[41,48] The unit cell of $CuGaS_2$ is tetragonal with a $I\bar{4}2d$ symmetry spacegroup,[49] or D_{2d} in Schoenflies notation.[41] The Cu^+ and Ga^{3+} cations are each coordinated to four sulfurs in tetrahedra, as displayed in figure 2.13. The lattice parameters of the unit cell varies in the litterature, and an overview is given in table 2.1. The overestimation of the calculated parameters is due to limitations in the calculation methods.[50]

Table 2.1: Lattice parameters for $CuGaS_2$.

a (Å)	c (Å)	Remark	Reference
5.328	10.462	Observed, orange colour	[51]
5.347	10.474	Observed, no colour info	[52]
5.349	10.47	Observed, brown colour	[41]
5.351	10.484	Observed, dark colour	[51]
5.356	10.435	Observed, no colour info	[53]
5.351	10.480	Observed, orange colour	[49]
5.51	10.74	Calculated	[50]

The covalency of the bonds is determined by the electronegativity difference which is 0.77 for the Ga-S bond and 0.68 for the Cu-S bond.[54] The bonds are thus partially ionic, partially covalent, as opposed to the corresponding oxides which are mainly ionic. The nature of the bonds will determine to what degree lattice substitution is affected by oxidation states. For an ionic bonding structure substitution will be highly affected by the oxidation states of the ions in question. This effect is much less prominent in the less ionic structure of $CuGaS_2$.

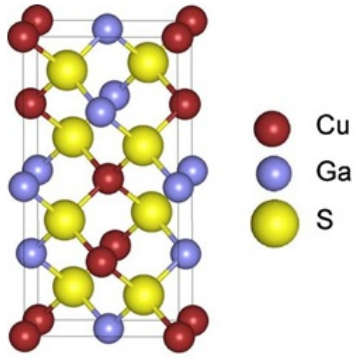

Figure 2.13: The tetragonal unit cell of $CuGaS_2$.[50]

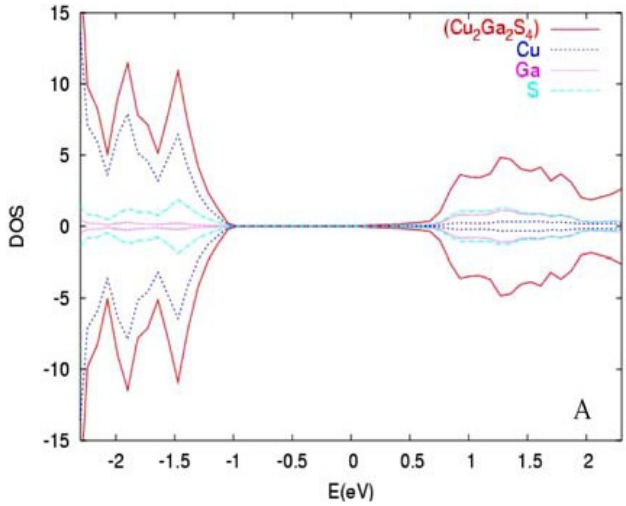

Figure 2.14: The band structure of $CuGaS_2$ calculated by DFT calculations.[55] *The valence bond is at the lowest, and conduction bond at the highest energies.*

As previously discussed, $CuGaS_2$ has been suggested as the best suited host for IB solar cells due to its direct broad band gap band structure.[10,40] The first reported estimation of the band gap size was 2.53 eV,[51] but has later been reduced to a band gap of around 2.4-2.5 eV.[40,56,577] at the Γ point in k-space.[50] The band structure of $CuGaS_2$ is complicated, since the electronic states close to the band edges have contributions from both the 3p states of sulfur and the 3d states of copper.[44,51] The band gap may be underestimated in calculations if this p-d hybridization is not accounted for.[44,58]A density functional theory (DFT) calculation of the band structure is presented in figure 2.14.

The size of the band gap decreases as the temperature of the semiconductor increases, as expected.[57] It is also expected that the band gap changes when making a thin film due to strains, but this is not the case for $CuGaS_2$. The system has been found to have the same band gap size for bulk single crystals as for polycrystalline thin films.[59] For application in thin film solar cells, this is an useful property.

The microstructure of $CuGaS_2$ seems to be dependant both on stoichiometry as well as synthesis parameters and method. There have been several reports on the morphology of $CuGaS_2$ thin films and powders. Thin films morphology vary from fine structured Ga-rich $CuGaS_2$ to granular Cu-rich $CuGaS_2$,[7] see figure 2.15(a). The morphology of $CuGaS_2$ powders vary a lot, from sphere-like particles in networks, as shown in figure 2.15(b), to spheres in the nanorange and snowflake-like structures in the microrange,[60] see figure 2.15(c). The microstructures found are differed by synthesis method and parameters. The microstructures are important for thin film growth for solar cell applications, as energy losses may be minimized by having uniform thin films with few grain boundaries and impurities.[61]

To understand why the stoichiometry of the $CuGaS_2$ structure can be allowed to vary from Ga-rich to Cu-rich, the phase diagram of the composition must be considered. The ternary diagram of Cu-Ga-S is given in figure 2.16(a). The $CuGaS_2$ phase is marked as "gal" for gallite. Several known binary phases are marked, as well as an unknown ternary phase X.[63] The dotted triangle in the diagram is enlarged in figure 2.16(b).

There is quite a wide composition range where $CuGaS_2$ can exist. This means that $CuGaS_2$ will often be slightly off-stoichiometric- with slight variations in the compositon.[64] The structure can accommodate a relatively large excess of Ga and S[48] and may co-exist with several other phases.[63] The varying stoichiometry and co-existence with secondary phases may be a challenge when targeting a phase pure product for solar cell applications.

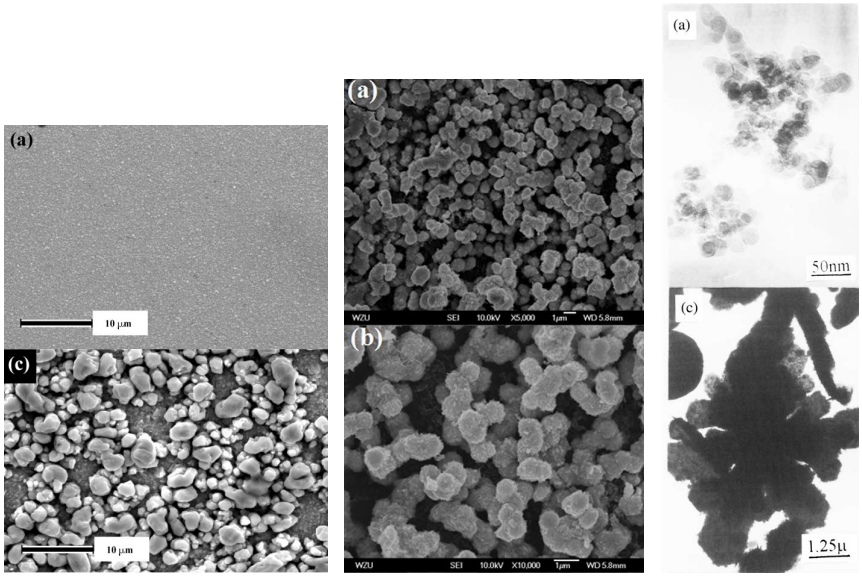

(a) (b) (c)

Figure 2.15: 2.15(a): Ga-rich (top) and Cu-rich thin films of $CuGaS_2$.[7] 2.15(b): Sphere-like particles of $CuGaS_2$ powder (top), with close-up image.[62] 2.15(c): Sphere-like nanoparticles (top) and snowflake-like microparticles of $CuGaS_2$.[60]

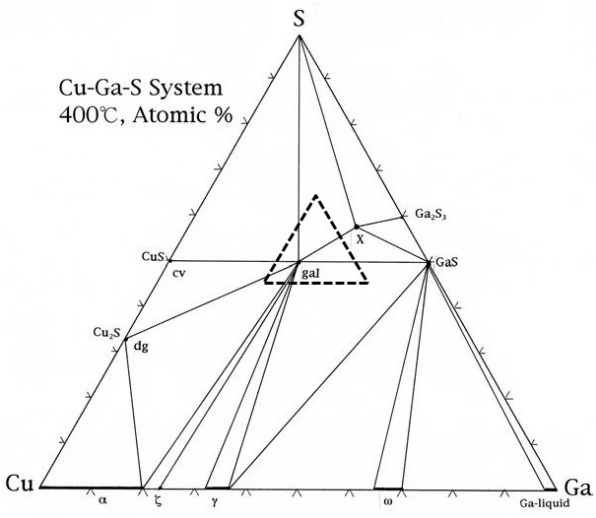

(a)

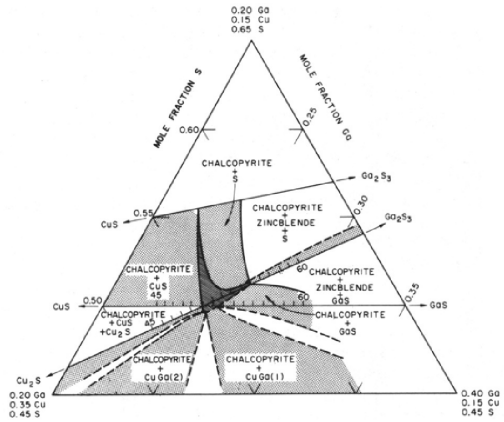

(b)

Figure 2.16: 2.16(a): Ternary phase diagram for copper, gallium and sulfur. Phases present are $CuGaS_2$ (gal), an unknown phase X, CuS covellite (cov), Cu_2S digenide (dig), Ga_2S_3, GaS, and five phases along the Cu-Ga line; $\alpha, \zeta, \gamma, \omega$ and liquid Ga.[63] 2.16(b): Close up of the dotted triangle section of the phase diagram that contain the $CuGaS_2$ phase, marked as dark grey.[48]

One effect of a changing stoichiometry is colour change of the structure. Different stoichiometric compositions will have slightly different band structures and absorb different wavelengths, making the colour of the semiconductor change. The p-d hybridization of sulfur and copper bands described above makes it difficult to accurately describe the optical transitions occurring in the structure.[44]

There have been many observations of the colours of $CuGaS_2$ with different stoichiometric compositions. There are few trends in these reports, possibly due to the lack of theoretical understanding of the electronic transitions occurring. The colour regions most often reported are yellow/orange,[48,64] green[48,64] and reddish brown/dark[62,65] colours.

In addition to composition differences, colour change in the structure may be attributed to other effects such as secondary phases present[48] and in the case of thin films, micro-crystals incorporated in the film.[64]

2.3.6 Iron substituted $CuGaS_2$

To introduce an intermediate band to the broad band gap of $CuGaS_2$ an impurity with suitable energy density states must be chosen. As described in section 2.3.3, the IB should be located around 0.9 eV from the valence band. In addition the impurity must be soluble in the $CuGaS_2$ lattice and a substitution must be thermodynamically favourable.[33,66]

Screenings have been made to identify the best suited transition metal for the formation of IB based on these criteria.[16,29,40,67] The position of the intermediate band formed by different first row transition metals can be viewed in figure 2.17. Based on the location in the band gap, both iron(II/III) and titanium(III/IV) have been suggested as promising choices of impurities[10,16]

The solid solubility of a compound into a ternary lattice gives information on the thermochemical stability of a substitution, as insoluble species will form binary secondary phases instead of being incorporated.[36] Choosing precursors where the metal is tetrahedrally coordinated will substantiate incorporation into tetrahedral positions in the $CuGaS_2$ lattice, while precursors with octahedral metal coordination will promote the formation of simpler binary secondary phases.[29]

Work done by Tablero and Fuertes[33] shows a thorough investigation of the solid solubility of different metals in the $CuGaS_2$ lattice. The results show that Mn, Sc and Ti were found to be insoluble and sources to undesired binary secondary phases. Fe, Co and Ni on the other hand, were found to be soluble. The band structure arisen from substitution of these metals to Cu-site and

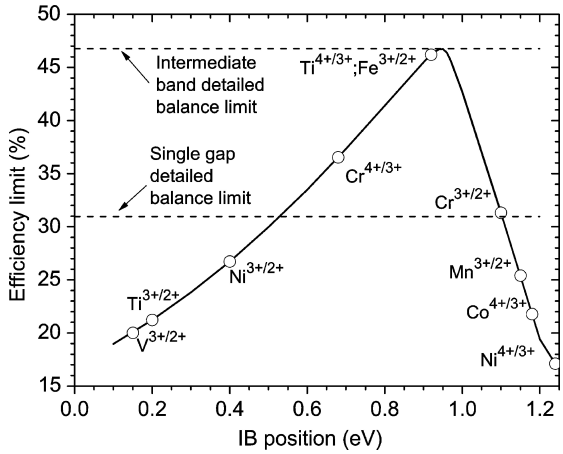

Figure 2.17: A comparison of the energetic position of an intermediate band formed by different first row transition metals. Efficiency limits based on 1 sun illuminations are also shown.[16]

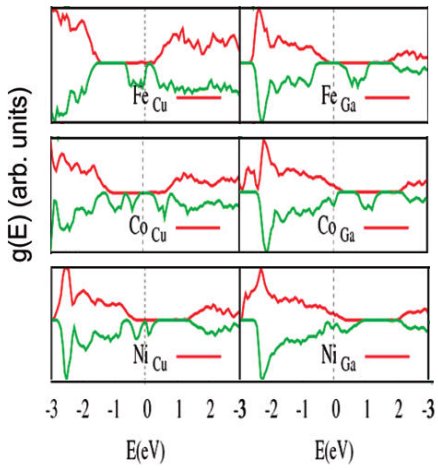

Figure 2.18: Calculated band structure of $CuGaS_2$ substituted with iron, cobalt and nikkel. Substitution to Cu-site (left) and to Ga- site (right).[33]

to Ga-site in the $CuGaS_2$ structure was investigated, see figure 2.18. Of these three, Fe forms a separated IB in the band gap, while the other have overlapping electronic states with the VB and CB of $CuGaS_2$.[33]

Based on these findings the quaternary system of iron substituted $CuGaS_2$ (CGFS) has been suggested as a promising structure for the use in intermediate band semiconductors.[10,68] In addition to having a promising calculated electronic structure and being soluble in the host lattice, iron is a relatively low-cost and environmentally friendly alternative to many other transition metals.

An intermediate band in the host band gap will enable a three-photon absorption process that is characteristic for the intermediate band system. In an absorption measurement, this will appear as two absorptions with energies lower than the band gap, in addition to an absorption edge at the band gap energy. This expected change in the optical measurements due to iron substitution was observed by a German group in the early 1970's.[49,69] The group reported a colour change and increased absorption in the near infra-red and visible range of the spectrum when introducing iron to the $CuGaS_2$ lattice. During the following years several groups reported similar optical measurements,[70,71] where the CGFS system had two sub-band gap absorptions in addition to the band gap edge. An example is given in figure 2.19. The studies were mainly aiming for application in light emitting devices. As the intermediate band concept was introduced decades later,[24] the optical change was not explained.

The first photovoltaic device made of CGFS with indications of an intermediate band electronic structure was recently made by Marsen et al.[28] The device consisted of a thin film of $CuGa_xFe_{1-x}S_2$ and had absorption intensities in the energy range expected for IB formation, see figure 2.20. The group assigned the absorption intensity of 1.9 eV to that of an iron related intermediate band in $CuGaS_2$. Despite the indication of an intermediate band, the charge carrier collection of the device was lower than an unsubstituted host. The cell had a lower open circuit voltage when substituted, giving an overall low efficiency, which may indicate increased thermal losses in the substituted cell compared to the pure $CuGaS_2$. The group suggests that the system should be seen as a model for further development rather than an optimized system.

The structure of iron substituted $CuGaS_2$ depends on the substitution site of iron. The $CuGaS_2$ structure has two unequivalent substitution sites, the monovalent Cu^+ and the trivalent Ga^{3+} site. Substitution is thermodynamically favoured by small lattice changes upon substitution. Figure 2.21 illustrates metal substitution to gallium-site in the $CuGaS_2$ structure.

Fe^{3+} is a good substituent for Ga^{3+} when it comes to ionic radii[49] and

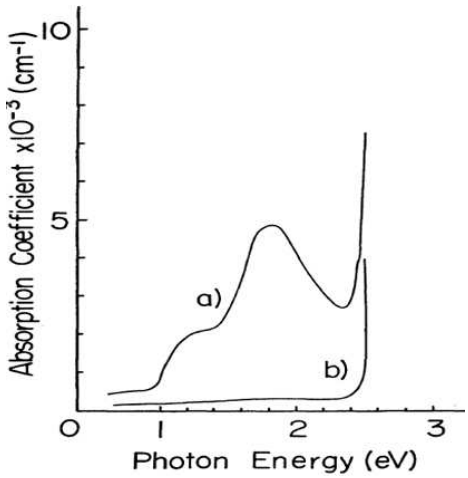

Figure 2.19: Absorption spectra of $CuGaS_2$ (b) and iron substituted $CuGaS_2$ (a) with sub-band gap absorptions.[71]

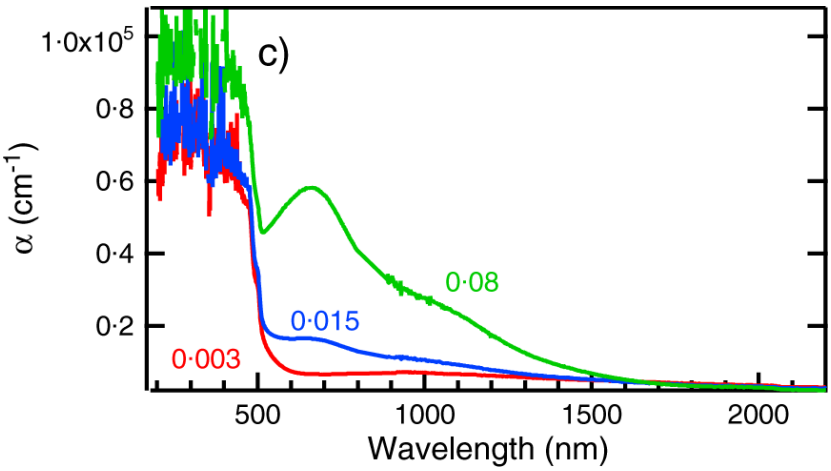

Figure 2.20: Absorption coefficient spectra for $CuGa_xFe_{1-x}S_2$ with different iron contents (x= 0.003, 0.015 and 0.08). The absorption edge at 500 nm (2.48 eV) is assigned to the band gap of $CuGaS_2$. In addition there are two sub- band gap absorptions at 650 nm (1.9 eV) and 1000 nm (1.2 eV).[28]

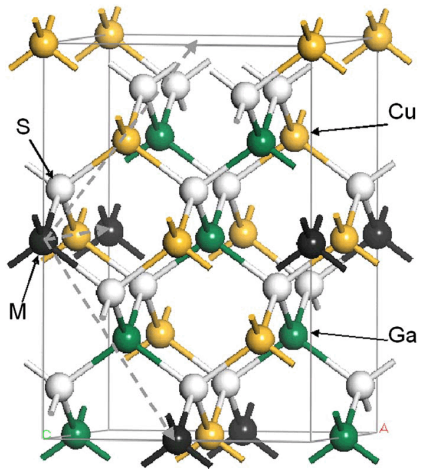

Figure 2.21: Metal substitution to Ga- site in the $CuGaS_2$ structure. The primitive cell axes are shown by dashed lines.[67]

Table 2.2: Overview of atomic and ionic radii of copper, iron and gallium. The coordination number of all ions is 4, as they are in tetrahedral site.[54]

Element	Atomic radii	Ionic radii (ox.state)
Copper	126 pm	60 pm (Cu^{+})
Iron	128 pm	49 pm (Fe^{3+})
Gallium	140 pm	47 pm (Ga^{3+})

oxidation states. The ionic radii of gallium and iron is much more similar than that of iron and copper, making a substitution into gallium site more energetically favourable. As previously discussed in section 2.3.5, the bonds in the structure are also partially covalent. When considering the covalent radii of the elements, iron is more similar to copper than to gallium, see table 2.2. The oxidation states of the elements need not be considered to a great extent for covalent bonds. The exact nature of the substitution site is complicated, due to the nature of the bonds, but the most commonly described substitution site is the Ga-site, giving the $CuGa_xFe_{1-x}S_2$ quaternary structure.

The phase diagram of the system, when substituting iron to Ga-site is presented in figure 2.22. For the substitution levels needed for the formation of an IB ($0 < x < 0.1$), it is seen that the melting point is around 1200 °C.[72]

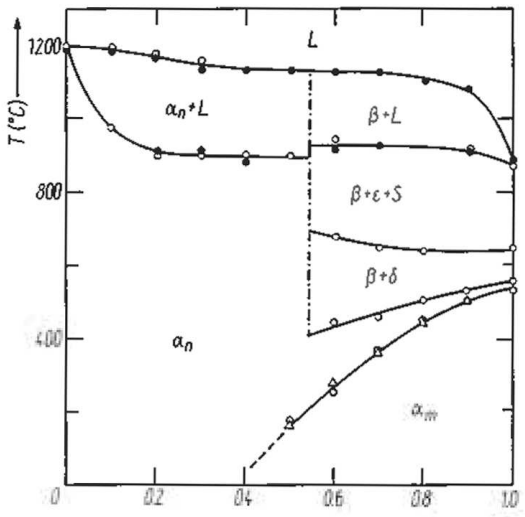

Figure 2.22: The pseudo binary phase diagram of the joint between $CuGaS_2$ (x= 0) and $CuFeS_2$ (x= 1). The phases present are a chalcogenide phase α, a face centered cubic phase β, pyrite δ (FeS_2), pyrrhotite ε ($Fe_{1-\gamma}S$), sulfur S, and liquid phase L.[72]

$CuGaS_2$ is isostructural to $CuFeS_2$,[73] and at low temperatures there is a single phase solid solution of the chalcogenide structure (α) for the whole composition range.[72]

The lattice parameters for the composition range have been investigated using least-squares analysis of x-ray diffractogram data,[73] see figure 2.23. The findings have been confirmed later another group.[72] It is seen from the figure that as the iron content in the lattice increases, the a parameter decreases, while c increases to a certain point before it decreases. For very low concentrations of iron in the lattice (under 1 %), the lattice parameter changes have been found to be neglishible.[49,65]

Low concentrations of iron affect the colour of the structure. Bardeleben et al.[70] describe the colour change as a function of iron content; pure $CuGaS_2$ is yellow or orange, low iron contents gives green colour and increasing the iron content further gives a black colour. The exact substitution amount is not described. This confirms the findings of Schneider et al.,[49] where iron containing $CuGaS_2$ was found to be green and black.

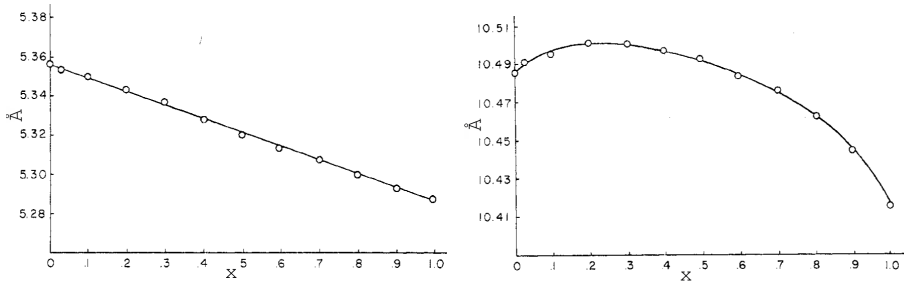

(a) Lattice parameter a (b) Lattice parameter c

Figure 2.23: Lattice parameters for the composition range between $CuGaS_2$ and $CuFeS_2$, x being the iron content.[73]

The colour change and the changes in optical measurements (seen in figures 2.19 and 2.20) indicates that iron substitution affects the optical properties of the system. Assigning absorption peaks in a spectra to different transitions in a band structure is challenging. According to Marsen et al.[28] the exact nature of the transitions taking place in the structure is not well-understood, due to the lack of calculations on transition mechanisms in the CGFS system. However, the group indicates that sub-band absorptions most likely are caused by the "stepping stone" effect created by an intermediate band in the band gap.

The time passing from the introduction of the IB concept to making the first device based on $CuGa_xFe_{1-x}S_2$ indicates that there are challenges in the field. The main challenge lies in combining thin film technology required to make a solar cell panel with the complex quarternary composition needed to get intermediate band structure. Competing binary and ternary impurity phases can precipitate, making the film inhomogenous. Synthesis parameters such as high temperatures may alter the films by growth phenomena. The iron impurities introduced may be unevenly spread in the lattice or in inadequate amounts, making the states in the band gap localized instead of a delocalized IB. This will cause major thermal losses due to non-radiative recombination.[36] The heterointerface between film and substrate may also cause recombinations.[28]

2.4 Wet chemical hydrothermal synthesis

The synthesis method chosen in this thesis is hydrothermal synthesis, based on the the many advantages of the method and the current status of iron substi-

(a) (b)

Figure 2.24: 2.24(a): Autoclaves of varying designs, volumes and pressure limitations. The picture is taken from the Parr Instrument Company website.[76] 2.24(b): The cross section of an autoclave with liner, filled with reagents and water.[75]

tuted $CuGaS_2$ (CGFS) synthesis, described further in section 2.5.

Hydrothermal synthesis is a wet-chemical method where precursors are dissolved in water. The method is similar to solvothermal synthesis, which is a more commonly used method using organic solvents. Hydrothermal synthesis is less harmful to the environment and often less expensive, as the solvent used is pure water.[74]

In the case of low-pressure syntheses, water may not suffice as a solvent due to the low solubility of many inorganic compounds in water. In hydrothermal synthesis the system is subjected to high pressure conditions. In some cases, the pressures obtained come close to or above the critical point of water.[75] Under such conditions the solubility increases drastically, making species normally considered insoluble, soluble in water.[74]

The high pressures are obtained using sealed reaction vessels called autoclaves, shown in figure 2.24. A teflon cup (called a liner) is filled with the precursors and water, is put into the autoclave which is sealed and heated to temperatures normally in the range of 100-250 °C.[75] When heated, the solution in the vessel expands and in some cases gases are evolved.

The main factors determining the pressure in the vessel are the temperature and the percentage fill of the liner called fill factor (not to be confused with the fill factor used in efficiency calculations). Figure 2.25 is based on the pressure contribution from the water in the vessel and shows how pressure can be controlled by fill factor and temperature choice. In addition, pressure contribution from gases evolved during the reaction must be included when calculating the

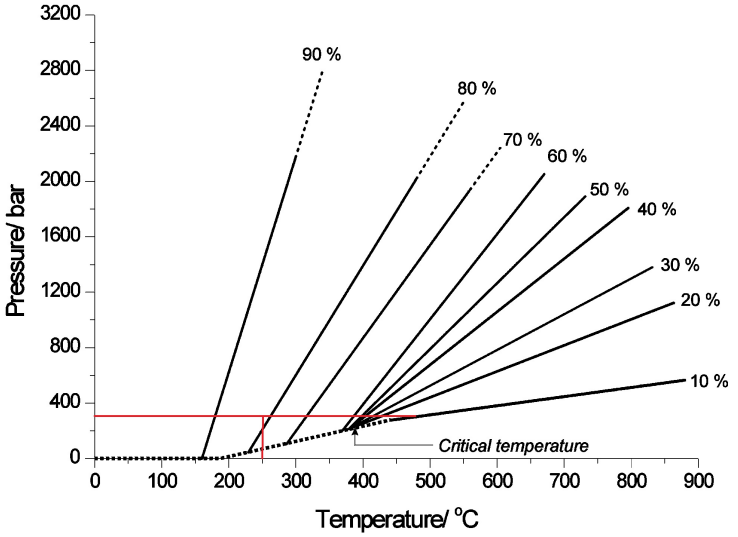

Figure 2.25: The fill factor and temperature of the autoclave determine the pressure inside the vessel, first shown by Walton et al.[75] An example is drawn into the figure, where a fill factor of 81% and heating to 250° C will give a pressure of 350 bar.

total pressure in the autoclave.

The elevated temperature and high pressure in the autoclave first makes insoluble species dissolve, giving higher solute concentrations (C). The mobility of the species is increased under hydrothermal conditions, and the reaction mixture is much more homogenous than its solid state counterpart.[74,75]

The reaction conditions helps the species overcome the energy barrier ($\Delta\ G_{nuc}$) needed for crystallization from the solution, given by equation (3).[74] The critical radii of a nuclei (R^*) is the radii where a stable nuclei is formed. Nuclei with radii smaller than this will dissolve. σ represents the surface tension. S_{sat} is the degree of supersaturation, given by C/ C_{eq}, which is the concentration at saturation and equilibrium. It is seen from the equation that increased temperature and concentration in the solution will decrease the nucleation barrier.

$$\Delta G_{nuc} = \frac{4\pi\sigma_{SL}R^{*2}}{3} \propto \frac{1}{T^2 S_{sat}} \tag{3}$$

The crystallization that takes place follows a nucleation and growth mechanism, where nuclei are formed when the supersaturation of the species in the solution is high enough. When the solution is no longer supersaturated, the nuclei starts to grow. Obtaining a product with a narrow particle size distribution requires a short nucleation time to avoid particle growth occurring simultaneously as nucleation.

The main advantages of hydrothermal synthesis is that the method facilitates homogenous nucleation and growth conditions for a broad range of inorganic compounds and that the method uses an environmentally friendly solvent, water. The equipment start-up costs combined with relatively low running temperatures makes this a cost efficient alternative to many expensive physical methods.

Another advantage is that the method gives crystalline products (solids with long-range ordering) directly without any further heat treatment. Other low-temperature methods such as the sol-gel method gives amorphous products that require a post-annealing step to obtain crystallinity.[74] In addition, the method allows control of stoichiometry, particle size and distribution.[60] It is possible to make nanosized crystals, but these have a tendency to form agglomerations due to their high surface energy.[77] The method has also been widely used for synthesizing nanostructured mesoporous (pores of 2-50 nm) materials.[74,78]

There are several disadvantages to the method though. The high pressures may cause a health hazard if not handled properly, especially when scaling up to industrial scale vessels. There may be concentration gradients in the vessel, as some inorganic species are not dissolved until the vessel is heated. Concentration gradients will enhance non-uniform products and should be avoided. For systems where this is a problem reaction vessels with stirring may be considered.

The main disadvantage of the method is that it is a batch method where the reaction takes place in a closed vessel, making real time (*insitu*) monitoring nearly impossible. As a result predicting the outcome of the reactions become difficult as reaction mechanisms remain unknown.[75] To get information on reaction mechanisms, the reaction in a vessel must be quenched after a series of reaction times and analysed after cooling to room temperature. Such an analysis implies that one has to assume that there is no change in the material from reaction conditions to room temperature and ambient pressures, an assumption that may in many cases involve great errors.[75]

To date there have not been done any extensive reaction mechanism studies on the $CuGaS_2$ system. Without detailed studies the exact reaction mechanism can not be known. In addition the reactions taking place are not necessarily in

equilibrium, making predictions of the reaction outcome even more difficult.

Despite a lack of systematic quenching experiments to determine the exact reaction mechanisms, suggested reaction mechanisms have been made. Hu et al.[60] suggest the reaction mechanism in equation (4); $[Cu(Tu)_x]^+$ complexes are formed from CuCl and thiourea ($SC(NH_2)_2$). The complexes release thiourea and dissolved Cu^+ to the solution. Thiourea is known to react with water and form S^{2-} ions. The dissolved ions of Cu^+, Ga^{3+} and S^{2-} can then precipitate as $CuGaS_2$.

$$Cu^+(aq) + Ga^{3+}(aq) + S^{2-}(aq) \rightleftharpoons CuGaS_2(s) \tag{4}$$

Competing reactions to this have also been suggested. Ga^{3+} can precipitate as GaO(OH) in low pH (1.8-1.9) solutions,[79] given in equation (5). The S^{2-} ions formed from the dissolution of thiourea may form H_2S gas,[80] see equaiton (6). In addition, any fully or partially oxidized copper in the solution may form competing binary copper sulfides (with $1 < \delta < 2$) shown in equation (7).

$$Ga^{3+}(aq) + H_2O(l) \rightleftharpoons GaO(OH)(s) \tag{5}$$

$$H^+(aq)^+S^{2-}(aq) \rightleftharpoons H_2S(g) \tag{6}$$

$$Cu^{+/2+}(aq) + S^{2-}(aq) \rightleftharpoons Cu_\delta S(s) \tag{7}$$

Reaction mechanism suggestions for the $CuGaS_2$ system including growth directing agents, such as the organic molecule L-cystine ($C_6H_{12}N_2O_4S_2$)[62] have been made. These mechanisms can not be directly translated to the water-based synthesis of $CuGaS_2$ as water is a non-structure directing solvent. The reaction mechanisms of similar systems with other compositions have also been investigated, for instance $CuInS_2$,[81] but these systems will not be directly transferable to this thesis' synthesis, as the compounds used are not the same.

2.5 Previous work

Iron substituted $CuGaS_2$ with intermediate band electronic structure has previously been made using physical methods.[28,65,70,71] These methods enables stoichiometric control, but require expensive equipment and have high running costs since high temperatures are needed.[75] $CuGaS_2$ has been made using hydro/solvothermal synthesis.[4,60,62] Hydrothermal synthesis has been used to make a non-chalcogenide based intermediate band material.[27] This thesis aims for a

combination of these; making iron substituted $CuGaS_2$ (CGFS) with IB structure using hydrothermal synthesis, a procedure not done to date. If successful, the method may be used to make CGFS for IB solar cell applications using the low-cost and environmental friendly approach of water-based wet chemical synthesis. This section will give an overview of the most important findings of selected previous works, to give a better understanding of the experimental procedures chosen in this thesis.

Sortland[4] used hydrothermal synthesis to make crystalline powders of $CuGaS_2$ with phase purities around 93 at%. Through a series of syntheses, a number of parameters were tested to see how the product was influenced. Phase quantification of $CuGaS_2$ compared to secondary phases such as covellite (CuS) and gallium hydroxide (GaO(OH)) was estimated using Rietveld analysis of the x-ray diffractograms. The best synthesis parameters were determined by comparison of the phase purity achieved.

Major findings were that high concentration of precursors gave higher ratio of the desired $CuGaS_2$ phase compared to secondary phases. Equal concentration of copper and gallium in the precursors was used, with four times excess of sulfur. It was suggested further that a high synthesis temperature of 250 °C and a reaction time of 30 hours would benefit the product purity. It was found that the best pH for the reaction was 1.

The complexing agent 1-pentanethiol stabilized the cations in the solution, reducing the yield of the reaction in equation (4) due to a shift in the equilibrium according to le Chateliers principle. As the complexing agent did not decrease the amount of secondary phases, it was found redundant to the reaction. A change in reactor volume by changing the autoclave size or adding substrate holders gave a reduced purity of the product. The morphology of the products was investigated using SEM. Many different morphologies were found. $CuGaS_2$ was mainly found to have a microstructure of irregular spheres in networks. The product powders had different colours; red, black and orange. Sortland suggests that the red was gallium rich, the black was copper rich and the yellow was partially stoichiometric. There was no clear trend in the microstrcutres of the different colours.

Sortland's work is based on work done by Hu et al,[60] where hydro- and solvothermal synthesis were used for the first time to make crystalline, yellow powders of single-phase $CuGaS_2$ without the need for post-annealing at high temperatures. The group suggests their synthesis route as suitable for making $CuGaS_2$ and other ternary compounds. The parameters used in the synthesis were a reaction temperature of 160 °C, 4 h reaction time, 95 % filling of the autoclave, pH= 1, equal concentration of copper and gallium, with an excess of

sulfur (no further detail is given). The microstructure of the obtained powders was strongly influenced by the solvent used. Uniform, spherical particles around 30 nm were found using water as a solvent, and snowflake-like microsized crystals using ethylenediamine as a solvent, see figure 2.15(c).

In a recent study done by Zhong et al.[62] solvothermal synthesis was used to make crystalline red powders of $CuGaS_2$ with few impurities. The morphology of the powders was irregular spheres, more or less entangled. The major findings of Zhong et al. relevant to this thesis is a confirmation of the synthesis route suggested by Hu et al. and that the group provides more detailed experimental parameters for reproduction and further development.

The precursors used were L-cystine ($C_6H_{12}N_2O_4S_2$) as a complexing molecule and sulfur source, copper chloride and gallium chloride. The solvent used was ethylenediamine. The group used equal concentration of copper and gallium, with four times excess of sulfur. The influence on reaction temperature and time on the morphology of the samples was investigated. It was found that increasing the reaction time from 6 to 15 hours gave more irregular nanoparticles. A wide temperature range was investigated and it was found that a reaction temperature under 160 °C gave secondary phases. A reaction temperature range from 180 °C to 220 °C was suggested as the best suited. The group found that further increasing the temperature above 230 °C did not affect the product. A reaction time and temperature of 10 hours, 200 °C was suggested as the parameters giving the most uniform particle size and morphology.

Work done by Lucena et al.[27] is important for this thesis as it is the first time a bulk semiconductor with a partially filled intermediate band absorbing across the whole solar spectrum has been synthesized.[40] The group made V substituted In_2S_3 by hydrothermal synthesis. This provides a proof-of-concept that bulk IB semiconductors can be made using wet-chemical synthesis, and encourages further work in the field. Another interesting fact from this synthesis is that a 10 % V substitution is used, which is an order of magnitude larger than the estimated amount needed for an IB formation.

Iron substituted $CuGaS_2$ has been made by several groups using physical methods; vacuum co-evaporation,[28] chemical vapor transport,[70,71] chemical transport reaction.[65] In all cases high reaction temperatures were used (400-900 °C). The importance of these works to this thesis is that the CGFS structure is found to be stable at room temperature, with promising optical measurements for IB applications, as previously described in section 2.3.6.

An overview of the selected previous works is given in table 2.3. A comparison of the synthesis parameters used in for hydro/solvothermal synthesis of $CuGaS_2$ is presented in figure 2.26.

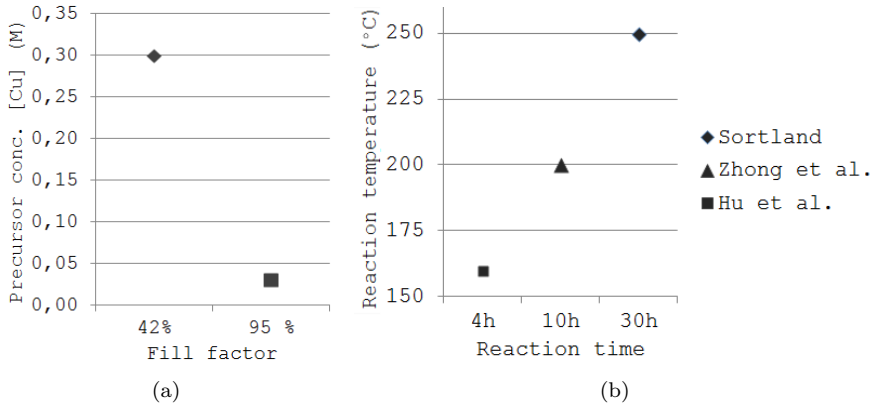

Figure 2.26: Overview of the synthesis parameters in the optimized hydro/solvothermal syntheses of $CuGaS_2$ by Sortland,[4] Hu et al.[60] and Zhong et al.[62]

Table 2.3: Previous work, an overview. Sortland reported a 93 at% phase purity of the product, the remaining powders are reported to be phase pure.

Structure	Synthesis method	Remark	Reference
$CuGaS_2$	Hydrothermal	Parameter study, iii	Sortland[4]
$CuGaS_2$	Hydro/ solvo-thermal	First wet- chemical synthesis of $CuGaS_2$, ii	Hu et al.[60]
$CuGaS_2$	Solvothermal	Parameter study, ii	Zhong et al.[62]
V:In_2S_3	Hydrothermal	First bulk IB material, ii	Lucena et al.[27]
CGFS	Physical meth.	i, ii	Marsen et al.[28]
CGFS	Physical meth.	i, iv	Teranish et al.[65]
CGFS	Physical meth.	i, iv	Bardeleben et al.[70]
CGFS	Physical meth.	i, iv	Tanaka et al.[71]

i: Optical measurements showing sub-band gap absorptions.
ii: Phase pure product reported.
iii: 93 at% phase purity reported.
iv: Phase purity not reported.

2.6 Characterization techniques

In this section, a short theoretical background for the characterization techniques used in this thesis will be given. The most relevant aspects of the methods will be discussed.

2.6.1 X-ray powder diffraction

X-ray powder diffraction (XRD) is a fingerprint technique for crystalline powders. A sample is irradiated by X-rays (usually from a copper source), and the scattered X-rays will have constructive interference (nλ) at the angles (θ) determined by Braggs law, given in equation (8).[82] The lattice spacing in Braggs law (d) is inversely proportional to the Miller indices hkl of the lattice planes in the sample. This gives a fingerprint set of diffraction lines for each crystalline phase present in the sample.

$$2dsin\theta = n\lambda \tag{8}$$

In powder XRD, the diffractogram of a given structure will consist of a set of peaks with varying breadth and intensity, giving rise to a wide range of structural information.[83] The first, and perhaps most important information from the diffractogram is the phase identification, where the unknown structure is compared to a reference (usually a Joint Committee on Powder Diffraction Standards (JCPDS)) database file. The reference is based on the 2θ positions of the peaks, giving a set of unique lines for each phase. Many phases may be identified in the same diffractogram. The phase identification can be done for phases present down to around 1-5 weight percent of the sample.[83]

The shape of the peaks may give information on the crystallinity and size of the crystallites. The peaks have a certain embedded breadth from the radiation from the Cu-source.[83] Large crystallites will have sharp peaks, small particle sizes will have broadened peaks. An amorphous or partially amorphous will have a very broad peak shape, see figure 2.27. Crystallites that are smaller than the detection limit of the XRD (2-10 nm) will appear as wide peaks,[83] which are similar to the peak shape of amorphous phases. If there is a large size distribution of the particles, or if the sample is partially amorphous, the peak shape will be a combination of these shapes. The peak broadening increases with the Bragg angle 2θ.[83]

The shape and position of the diffraction peaks may in some cases be used to distinguish between co-existence of two phases, and lattice changes occurring in a crystal. In a study by Marsen et al.,[68] the peak position and shape is used

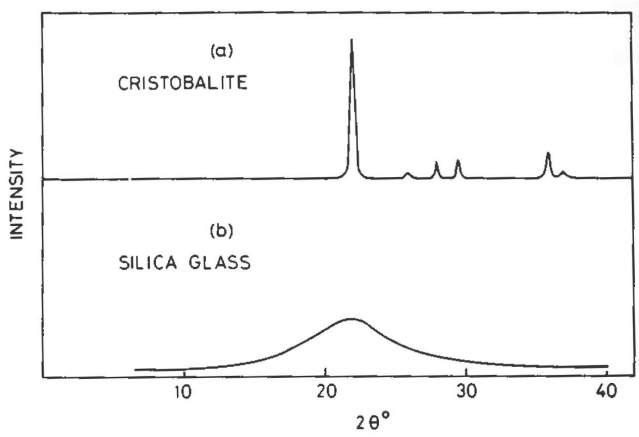

Figure 2.27: Typical powder x-ray diffractograms of crystalline (top) and amorphous (bottom) powders.[82]

as an indication of whether iron is substituted into the $CuGaS_2$ lattice, or is forming a secondary $CuFeS_2$ phase. The first gives a shift in the diffraction peak, while the latter gives a split of the diffraction peak, see figure 2.28.

Detailed structural and compositional information may be extracted from the diffraction data, using different calculation methods. The Rietveld method is an analysis method that combines peak intensities with peak positions, for quite accurate quantifications of the diffractograms, given that the powder analyzed is of high phase purity. The method uses least squares methods to make a theoretical fit to the collected diffractogram data.[54] The input data needed is detailed structural information on all phases present. Since the method uses both the intensities and the positions of the peaks, relative amounts of the different phases present may be quantified. For powders of lower phase purity, the Pawley method may be used for calculating the unit cell parameters and crystallite sizes.[84,85] The method is peak intensity independent, refinements are made based on peak position. Changes in the peak positions compared to the starting point gives information on changes in the lattice parameters of the crystal. A shift toward lower 2θ angles values means that the d spacing has increased, giving an increase in the lattice parameter(s) for that hkl plane. Higher 2θ angle of a peak means a contraction of the hkl plane.

A change in the lattice parameters may give information on composition

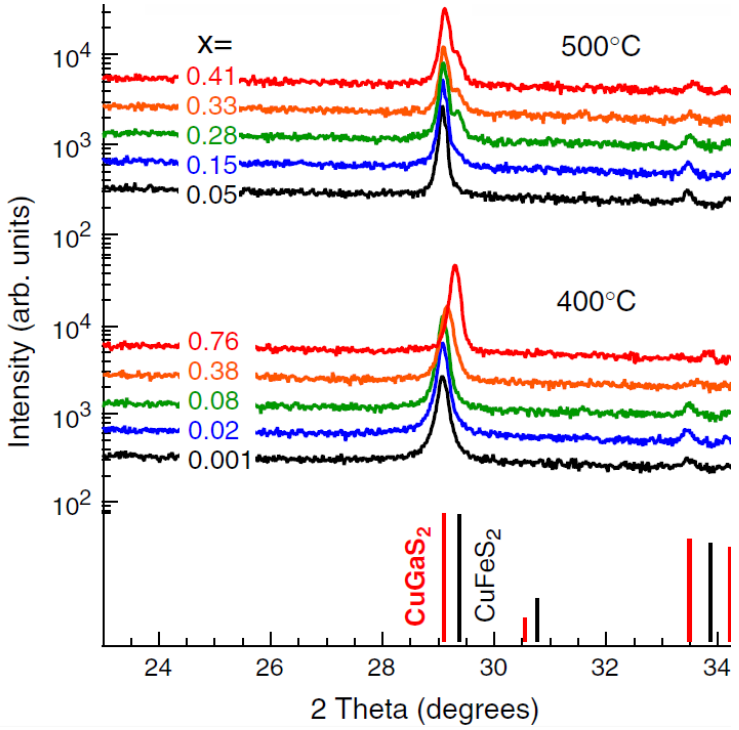

Figure 2.28: X-ray diffraction patterns showing a peak-split when both $CuGaS_2$ and $CuFeS_2$ are present in a powder (top), and a peak-shift for iron substitution into the $CuGaS_2$ lattice (bottom).[68]

variations. This is due to the small, but detectable changes in lattice parameters along a solid solution line.[83] As can be viewed in figure 2.23, such variations can indeed be detected for the iron substituted $CuGaS_2$ system. For increased iron content the a parameter decreases linearly, while the c parameter follows an parabolic increase followed by decrease.

There are a few limitations of the XRD method. First of all the sample must be crystalline. Any impurity phase that is not crystalline will not be detected using XRD. The lower detection limit of 1-5 wt% means that impurities present in very low weight percents will not be detected. For solar cell applications this is unfortunate as even low impurity concentrations may cause thermal losses. The copper irradiation is not necessarily monochromatic, as it is most common to have irradiation of both $K_{\alpha 1}$ and $K_{\alpha 2}$ irradiation. The combination of the two is known to cause some peak shoulder issues, espescially at high Bragg angles. The problem may be avoided by using only $K_{\alpha 1}$ irradiation.

The Rietveld and Pawley methods have several pitfalls that should be avoided. The amount of refinement parameters should not be too many. This is especially important for samples that are not phase-pure, as phase peaks may overlap. The quantitative data from the calculations are not absolute, but a mere relative quantification based on the same refining parameters. This means that a comparison of parameters such as phase purity or lattice parameters should only be done when the refinement parameters are the same.

2.6.2 Scanning electron microscopy and energy dispersive x-ray spectroscopy

Scanning electron microscopy (SEM) is a microscopy technique where a sample is bombarded with high energy electrons to give an image of the surface of the sample (normally in the microrange 0.1-100 μm).[82]

When the primary electrons hit the sample surface, some are backscattered and some penetrate the sample.[86] The accelerating voltage of the incoming electrons will determine the penetration depth of the electron beam, and therefore also the surface sensitivity of the method. The element analysed will also affect the penetration depth. For instance will electrons of 1 keV penetrate 50 nm into carbon and a 10 nm into gold.[86] Higher energies will give a lower surface sensitivity, but more information on the bulk of the sample. The penetrated electrons interact with the atoms in the sample, giving emission of secondary electrons and X-ray irradiation.

Some of the secondary electrons remain in the sample, and some are released to the continuum where they are detected and imaged by a detector. This gives

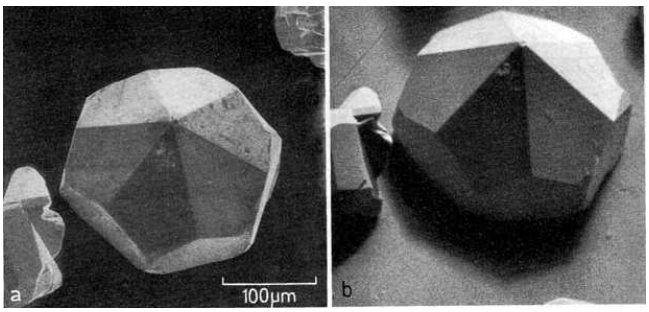

Figure 2.29: SEM images showing topography of a small crystal, for detector mounted perpendicularly (a) to the surface and to the side (b) of the surface.[86]

an image with topographical information of the sample surface. The location of the detector compared to the surface will influence the degree of topographical info obtained, as shown in figure 2.29. The images can be used to investigate the microstructure of the powder, as particle size, shape and texture are quite easily identified.[86]

The generated X-rays may be used to chemically characterize the sample, a technique called energy dispersive spectroscopy (EDS). The emitted X-rays have element characteristic energies, and the elements present in the sample may be identified and quantified.[82] The composition of different microstructures may thus be analysed.

Some of the advantages of the method is that sample preparation is easy, since the thickness of the sample does not have to be considered. Operating the instrument is relatively easy and quick.[54,82] The main drawbacks of the method is that the sample has to be conducting, the resolution is limited to the micro-range[82] and chemical analysis can only be done for the surface of the sample, not bulk.[54] EDS can only analyse heavy elements, hydrogen will for example not be included in the analysis. EDS mapping of particles will include some matrix effects, meaning that the surrounding and underlying particles will affect the elemental composition that is measured. The effect of underlying particles will be higher for higher mapping energies, as these have larger penetration depths than low mapping energies.[86]

2.6.3 UV-vis reflectance spectroscopy

For solid powder samples, reflectance spectroscopy may be used to get information on the optical properties of the sample, a technique called Ultraviolet-visible (UV-vis) reflectance spectroscopy or Solid state reflectance spectroscopy. The absorption properties of the sample is measured indirectly, by measuring the light reflected from the sample.[87] This may give information of the band structure of a semiconductor, as absorption energies are closely linked to electron structure features such as the band gap.

The sample is illuminated with light in the ultraviolet, visible and sometimes the near infra-red region, and a spectrum of the absorption of light is recorded. For a single band gap semiconductor, all light with energy higher than the band gap will be absorbed by the sample, giving a band edge feature to the spectrogram. Examples of a spectra are given in figures 2.19 and 2.20.

An integrating sphere is used to detect the reflected light from a dark background (D), an ideal non absorbing white reference (S_{ref}) and the sample itself (S). The reflectance of the sample (R) is calculated from equation (9).

$$R = \frac{S - D}{S_{ref} - D} \tag{9}$$

From this reflectance, the absorbance of the sample may be calculated using Kubelka-Munk theory.[88] The theory describes the optical properties of a sample which both absorbs and scatters parts of the incoming light. It is assumed that the particles in the powder is much smaller than the thickness of the sample investigated. For such a powder, the volume averaged absorption coefficient (A) is a function of the reflectance (R) as given by equation (10).[87] The scattering factor (S) is constant for all wavelengths. The true absorption coefficients of a compound, α, is proportional to A.[87,89]

$$\frac{A}{S} = \frac{(1 - R)^2}{2R} \tag{10}$$

For non-transparent powders, the major challenge with this method is the high absorbance of the powder. A high absorbance means that very little light is scattered of reflected from the sample. This is unfortunate for the method, as it is based on detecting reflected light from the sample. For high-absorbance samples, the signal ratio of the spectra may be very high. In some cases the noise may exceed the signal, giving no information from the spectrum.

3 Experimental

3.1 Materials

Gallium chloride ($GaCl_3$), copper chloride (CuCl) and thiourea ($SC(NH)_2$) were purchased from Sigma Aldrich and used as received. The hydrophilic $GaCl_3$ and CuCl were stored in a glove box with argon atmosphere. Iron-hexahydrate ($FeCl_3 \cdot 6\,H_2O$) was purchased from Sigma Aldrich and an iron chloride ($FeCl_3$) solution was standardized as described in section 3.2. All compounds used were of analytical grade.

3.2 Standardizing $FeCl_3$

A standardized $FeCl_3$ solution was made by weighing out 13.5154 g $FeCl_3 \cdot 6\,H_2O$ using a Mettler Toledo Sartorious TE2145 analytical balance and dissolving it in water. A 100 mL flask was used, giving a calculated concentration of 0.5 M. Since the given stoichiometry of the compound ($FeCl_3 \cdot 6\,H_2O$) is not exact, the concentration is not precise, and standardization is needed. The mass of the solution was noted.

Three porcelain crucibles were dried in a Carbolite Chamber Furnace ELF 11/6 at 800 °C for 2 hours, cooled to 400 °C and placed in a desiccator until it reached room temperature. Three parallels of ca. 0.5 mL were pipetted out and added to porcelain crucibles. The crucibles were weighed before and after added solution, giving the mass of the $FeCl_3$ in the crucibles. The crucibles were heated to 100 °C, held there for 3 hours, then heated to 800 °C, held there for 6 hours, and cooled down to 400 °C. The crucibles were taken out at 400 °C and placed in an desiccator, until it reached room temperature. The obtained Fe_2O_3 oxide was weighed at room temperature.

The number of moles of iron in the oxide was used to calculate the number of moles of iron in the $FeCl_3 \cdot 6\,H_2O$ solution. The $FeCl_3$ was standardized to 0.4982 M $\pm$ 0.001.

3.3 Synthesis method

Appropriate amounts of thiourea, $GaCl_3$ and CuCl were weighed out to get the required concentration using a Mettler Toledo Sartorious TE2145 analytical balance. $GaCl_3$ and CuCl were stored and weighed out in a glove box with argon atmosphere. A 50 mL flask was filled with 10 mL ion exchanged water and the precursors were added in the respective order stated above. For the

(a) (b)

Figure 3.1: 3.1(a): Flasks of 0.03M, 0.15M and 0.30M precursor concentrations. 3.1(b): 4746 High Strength Acid Digestion Vessel (autoclave) with all parts, including corrosion and rupture discs.

iron substitution syntheses, the standardized $FeCl_3$ solution was then added using a micropipette. The flask was filled further up with ion exchanged water, till almost full. To dissolve the precursors, the flasks were placed in a WVR Ultrasonic Cleaner bath with heating. The time and temperature needed to dissolve the precursors varied with concentration, normally the solution was heated to 30-40 °C for 30-50 minutes.

The pH was adjusted to pH= 1 ± 0.1 using concentrated hydrocloric acid (HCl, 37 %, puriss, Sigma Aldrich), the pH was measured using an inoLab pH-750 pH-meter. This pH value was chosen based on previous work by Sortland.[4] After adjusting the pH, the flask was filled further with ion exchanged water, until the solution was 50 mL. The standarized solutions were kept in a refrigerator of 4 °C. Solutions used for iron substitution experiments are displayed as an example in figure 3.1(a).

A micro-pipette was used to measure the desired volume of the solution for the syntheses, the solution was added to a Polymer Tetrafluoroethylene (PTFE) teflon liner (no 314, Parr Instrument Company). An autoclave of the type 4746 High Strength Acid Digestion Vessel from Parr Instrument Company was used in the syntheses, see figure 3.1(b) The autoclave had a maximum pressure limit of 350 bar, and maximum temperature limit of 275 °C. The vessel was assembled, the lid was screwed on tight and the vessel was placed in a pre-warmed Termaks TS8000 drying oven. After the given reaction time, the oven door was opened and the vessels remained in the oven until cooled room temperature.

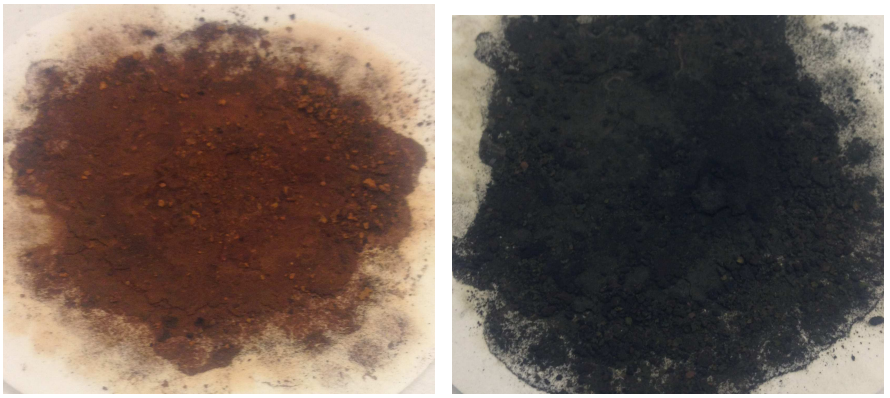

(a) (b)

Figure 3.2: Typical as-obtained powders of unsubstituted (a) and iron substituted (b) experiments.

The cooled vessels were opened and the PTFE liner was lifted out. The contents of the liner was transmitted to a Whatman White Ribbon, Ashless Filter Paper 589/2, Ø 70 mm. The precipitate was washed to remove water soluble impurities, five times with distilled water followed by five times with 70% ethanol and finishing with water once more.

The product was dried at 60 °C for 4 hours, with a 10 mbar air pressure, using a Binder vacuum drying cabinet. The washing and drying procedures were based on previous work.[4,60,62] The obtained dry powder was weighed and transferred to sample vials, typical products are given in figure 3.2.

Calcination of selected samples in air was done using a Carbolite CWF1300 oven and in 5.0 N_2 flushing in a ENTECH ETF30-50/17-S horizontal tube furnace. The crucibles were heated to 250 °C for 1 hour to remove water. The sample was added to the crucible, and heated by 200 °C/h to 800 °C. This temperature was held for 24 hours, after that a cooling rate of 200 °C/h to 400 °C was used. The crucibles were taken out at 400 °C and placed in a desiccator until cooled too room temperature.

A detailed overview of the syntheses performed, with all reaction parameters are given in tables 3.1-3.6. The sample names are given, indicating the composition of the precursors as well as the parameters changed in the experiment.

Table 3.1: Preliminary experiments: Synthesis 1 is a reproduction of 7a- the best synthesis from Sortland,[4] 2 is a reproduction in a smaller volume autoclave and 3 has an increased pressure. Pressure limits of the large autoclave disabled an increase of fill factor.

Autoclave volume	42% fill factor	75% fill factor
125 mL	1 (7a[4])	Not possible
23 mL	2	3

*Parameters kept constant: [Cu]:[Ga]:[S]= 0.30M: 0.30M: 1.20M, 250 °C, 30h, pH=1.

Table 3.2: Unsubstituted $CuGaS_2$: Fill factor and concentration experiments. The name of each synthesis indicate the concentration of copper/gallium, as well as the fill factor.

Concentration (M) [Cu] : [Ga] : [S]	42% fill factor	60% fill factor	73/80 % fill factor
0.03: 0.03: 0.12	CGS42-0.03	CGS60-0.03	CGS80-0.03
0.15: 0.15: 0.60	CGS42-0.15	CGS60-0.15	CGS73-0.15
0.30: 0.30: 1.20	CGS42-0.30	CGS60-0.30$^{\alpha}$	Not possible

*Parameters kept constant: 250 °C, 30h, pH=1,autoclave volume= 23 mL, stoichiometric relation Cu:Ga:S= 1:1:4.

α: Absorption properties measured.

Table 3.3: Unsubstituted $CuGaS_2$: Effect of sulfur excess. The name of each synthesis indicate the fill factor and sulfur excess.

Concentration (M) [Cu] : [Ga] : [S]	42% fill factor	60% fill factor
0.15: 0.15: 0.60	CGS42(4x)$^{\gamma}$	CGS60(4x)$^{\gamma}$
0.15: 0.15: 0.75	CGS42(5x)	CGS60(5x)

*Parameters kept constant: 250 °C, 30h, pH=1, autoclave colume= 23 mL.

γ: CGS42-0.15 and CGS42-0.15 from table 3.2, reused

Table 3.4: CGFS: Ga- substitution site. The name of each synthesis indicate the stoichiometric relation between Cu:Ga:Fe as well as the fill factor and the concentration [Cu] or [Ga+Fe].

Concentration (M) [Cu]: [Ga]: [Fe]: [S]	42% fill factor	60% fill factor
0.03: 0.027: 0.003: 0.12	$CG_{0.9}F_{0.1}S42\text{-}0.03$	$CG_{0.9}F_{0.1}S60\text{-}0.03^{\alpha,\rho}$
0.15: 0.135: 0.015: 0.60	$CG_{0.9}F_{0.1}S42\text{-}0.15$	$CG_{0.9}F_{0.1}S60\text{-}0.15^{\alpha,\rho}$
0.30: 0.270: 0.030: 1.20	$CG_{0.9}F_{0.1}S42\text{-}0.30$	$CG_{0.9}F_{0.1}S60\text{-}0.30^{\alpha,\rho}$

*Parameters kept constant: 250 °C, 30h, pH=1, autoclave colume= 23 mL.

α: Absorption properties measured.

ρ: Reproduced.

Table 3.5: CGFS: Cu- substitution site. The name of each synthesis indicate the stoichiometric relation between Cu:Ga:Fe as well as the fill factor and the concentration [Ga] or [Cu+Fe].

Concentration (M) [Cu]: [Ga]: [Fe]: [S]	42% fill factor	60% fill factor
0.027: 0.03: 0.003: 0.12	$C_{0.9}GF_{0.1}S42\text{-}0.03$	$C_{0.9}GF_{0.1}S60\text{-}0.03^{\alpha,\rho}$
0.135: 0.15: 0.015: 0.60	$C_{0.9}GF_{0.1}S42\text{-}0.15$	$C_{0.9}GF_{0.1}S60\text{-}0.15^{\alpha}$
0.270: 0.30: 0.030: 1.20	$C_{0.9}GF_{0.1}S42\text{-}0.30$	$C_{0.9}GF_{0.1}S60\text{-}0.30^{\alpha,\varepsilon}$

*Parameters kept constant: 250 °C, 30h, pH=1, autoclave colume= 23 mL.

ε: Calcination experiment made.

α: Absorption properties measured.

ρ: Reproduced.

Table 3.6: CGFS: Temperature and time. Iron is substituted to Cu- site. The name of each synthesis indicate that the reaction temperature and time.

Rx.time \ Temp.	160 °C	200 °C	250 °C
1 h	CGFS160-1	CGFS200-1	CGFS250-1
4 h	CGFS160-4	CGFS200-4	CGFS250-4
30 h	CGFS160-30	CGFS200-30	$CGFS250\text{-}30^{\beta}$

*Parameters kept constant: [Cu]:[Ga]:[Fe]:[S]= 0.135M: 0.15M: 0.015M: 0.60M, 60 % fill factor, pH= 1, autoclave volume= 23 mL.

β: C0.9GF0.1S60-0.15 from table 3.5, reused.

3.4 Characterization

X-ray diffraction (XRD) analysis was performed using a D8 Focus XRD apparatus, with copper ($K_{\alpha 1}$= 1.54051 Å and $K_{\alpha 2}$=1.54433 Å) irradiation and a Position Sensitive Detector. A single-crystalline silicon sample mount was used. A thin, uniform layer of the product was spread out on the substrate using a glass plate and ethanol. For the unsubstituted products the measuring parameters used were 2.5 seconds per step, 0.05° step length. The 2θ range analysed was 15- 70° using a slit size of 0.2 mm and sample holder rotation. For the iron substituted products the parameters used were 1.6 seconds per step, 0.03° step length. The 2θ area analyzed was 15- 70° using a slit size of 0.6 mm and sample holder rotation. The change in step length was made in order to get higher resolution.

In one case, a Simens D5005 XRD was used, with monocromatic copper $K_{\alpha 1}$ irradiation and a Braun Position Sensitive Detector detector. The measuring parameters used were 1.6 seconds per step, 0.03° step length. The 2θ area analyzed was 15- 70° using a slit size of 1 mm and sample holder rotation.

Phase identification of the RAW data was made using EVA software version 2.1. The elements present in the reaction mixture was inserted, and phases were identified using the PDF-4+2012, software version 4.12.0.4, database version 4.1203. When comparing different diffractograms, the peak intensity of the main peaks of the samples were aligned by y-scaling, to enable comparison of the relative intensities of the peaks. Y-offset was used to shift the diffractograms on the y-axis.

TOPAS software version 4.2 was used for Rietveld and Pawley analysis of the diffraction patterns. An overview of all refinement parameters used and structural information of the different phases inserted is given in appendix A. In the Rietveld analysis, the relative amount of the phases present in each sample was evaluated. Here, the $CuGaS_2$ phase was inserted using the "Add structure" option, and full structural information based on the PDF database was inserted. Pawley analysis was used to find the unit cell parameters and crystallite sizes. Here, the $CuGaS_2$ phase was inserted using the "Add hkl phase" option, and only the space group and lattice parameters from the PDF database were inserted. The mismatch of the refinement and the data is indicated in TOPAS with a R-weighted pattern (Rwp) value, which is the fraction of the calculated data compared to the actual data, 1 being no mismatch.[85]

To enable a correct refining, the phases can not be superpositioned. This means that if there are two possible structures for the chalcopyrite, each refinement must only include one of them. For instance a refinement on both $CuGaS_2$

and $CuFeS_2$ can not be made simultaneously. Each phase has to be refined separately , and the fit of the refinement (Rwp value) must be compared, as well as a manual inspection of the fit.

Scanning electron microscopy (SEM) analysis was performed to look at the morphology of the sample, using a TM3000 Hitachi table top SEM. The sample preparation was made by placing a few particles of the sample in an Eppendorf tube, adding 70 % ethanol and placing it into a ultrasonic bath for 10 minutes. A droplet of the solution was taken out and placed onto a carbon tape on an sample holder. The sample holder was inserted into the tabletop SEM, at a working distance of about 1 cm. The accelerating voltage used for SEM analysis was 15 kV. EDS connected to the SEM was used to study the composition of the different morphologies of the sample. The accelerating voltage was set to "Analyze" for these measurements, giving lower voltage and higher currents, more suited for element analysis. The elements chosen for analysis was Ga, Cu, S and O for the unsubstituted samples and Fe in addition to these for the substituted samples.

UV-vis reflectance measurements were made to selected samples to investigate the powder's optical properties. The set-up of the equipment was a source that emitted white light (Fiber light source from Hamamatsu), connected to an integrating sphere from Labsphere that focused the light onto the sample. From the sample, the reflected light was detected in a diode array detector. Since the sample is a non- transparent solid, light can not be transmitted through the sample. The light is reflected at grain boundaries on the surface and in the bulk sample, and is reflected back in many directions, called diffuse reflection. The absorbance of the sample can be calculated from the measured reflectance, based on the equations described in section 2.6.3.

4 Results

4.1 Preliminary experiments

Three experiments were made to give preliminary indications on the reproducibility of previous work, the effect of reduced reactor volume and increased pressure. An overview is given in figure 4.1 for the reader's convenicence, further details are given in table 3.1.

As this thesis is based on a master thesis by Sortland in 2011,[4] it was first attempted to reproduce the best powder of $CuGaS_2$ from this work. In synthesis 1, the same synthesis parameters and equipment was used as used by Sortland to produce their best product 7a. A fine powder with redbrown and orangebrown colour was obtained.

A comparison of the diffractograms of the original product made by Sortland (called 7a) and the product of the repdroduction syntheis 1 is presented in figure 4.2. The main phase identified in both products was the tetragonal $CuGaS_2$. A secondary phase of covellite (CuS) was identified in synthesis 1, indicated with triangles. The main secondary phase identified by Sortland in 7a is a digenite ($Cu_{2-\delta}S$) phase, indicated with circles.

The covellite and digenite secondary phases have similar unit cells, and therefore quite similar diffractogram patterns. A Rietveld analysis was done to synthesis 1 to determine which of the sulfide phases was present. CuS was found to have a better fit to the data than $Cu_{2-\delta}S$. This is mainly due to the distinct CuS peaks at 2θ= 31.9 and 32.9 angles, which were not present for the $Cu_{2-\delta}S$ phase.

The main peak located around 2θ= 29 has an interesting peak shape. The shape of the peak indicates that there is a large size distribution of the crystallites, the smallest being around the detection limit of XRD, giving a very wide peak, the largest giving a narrow, high peak shape. When a product contains a large size distribution, the peak shape may look somewhat like that shown here. Another aspect of the main peak is the shoulder located around 2θ= 27.5. This may be due to secondary phases present, or due to instrumental effects due to the non-monochromatic $K_{\alpha 1}$ and $K_{\alpha 2}$ irradiation as explained in section 2.6.1. A phase identification should therefore not be done solemnly based on this shoulder, but be based on other peaks as well.

As can be seen in figure 4.2, the CuS phase has two diffraction lines in the same region as the shoulder of the main peak, but it also has distinctive diffraction lines at the 2θ angles 31.9 and 32.9. A phase identification may therefore be done with a good accuracy based on the latter two peaks. The

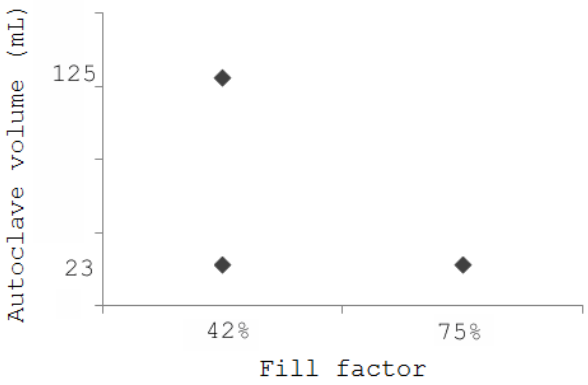

Figure 4.1: An overview of the parameter variations of the preliminary syntheses. Synthesis 1 and 7a by Sortland have 125mL x 42%, synthesis 2 have 23mL x 42%, synthesis 3 have 23mL x 75%.

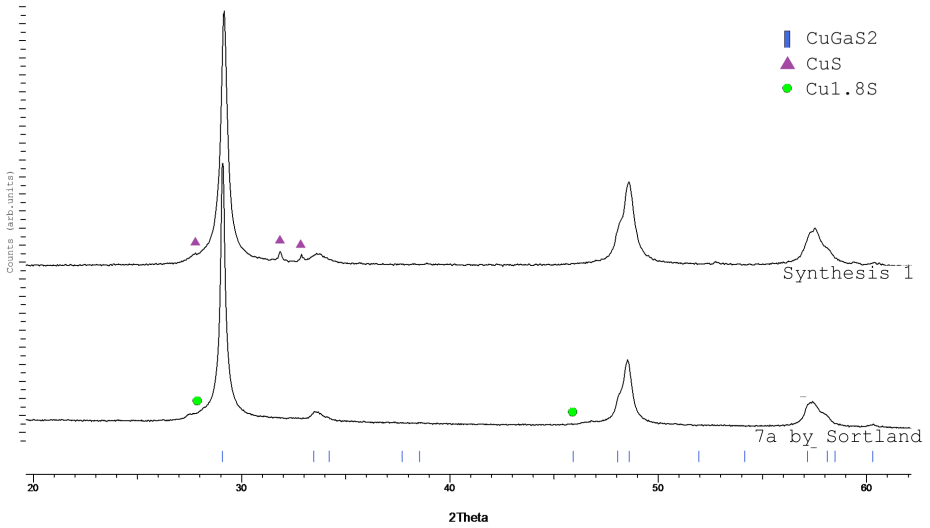

Figure 4.2: Diffractograms showing the best product from the work done by Sortland (7a).[4] Synthesis 1: a reproduction of 7a with the same synthesis parameters used. The diffraction lines of $CuGaS_2$ are displayed and the main peaks from the secondary phases are indexed.

$Cu_{2-\delta}S$ phase does not have distinctive peaks other than the 2θ= 27.5 peak, which makes phase identification of this phase difficult.

A Rietveld analysis was done with the aim of giving a quantitative analysis of the phase composition, giving a peak intensity problem for all the peaks corresponding to the $CuGaS_2$ phase. This can be seen from the mismatch curve at the bottom of figure 4.3, where it is seen that the Rietveld refinement has an overestimation of the 2θ= 34 peak and an underestimation of the 2θ= 49 and 57 peaks. Since this may be due to preferred orientation of some hkl directions, a refinement based on preferred orientation of the overestimated peaks was attempted. This did not result in an improvement on the mismatch curve. In addition, based on the microstructure of the sample (see figure 4.6) it is suggested that preferred orientation is not likely for this sample.

Figure 4.4 is the Pawley fit for the $CuGaS_2$ phase of the same product, giving a much lower peak intensity misfit. A phase composition quantification requires refinement on peak intensities though, so the phase purity of $CuGaS_2$ was calculated using Rietveld analysis. The refinement gave a composition quantification of 96 weight percent $CuGaS_2$ and 4 weight percent CuS. Converted to atomic percent (at %) the phase purity was found to be 94 at% $CuGaS_2$, with 6 at% CuS for synthesis 1.

The quantification using Rietveld may only be seen as relative to other quantifications using the exact same refinement procedures. It is therefore not possible to directly compare the purity with that of Sortland's synthesis 7a (93 at%). The diffractograms will give a better indication on the reproducibility than the Rietveld calculations in this case.

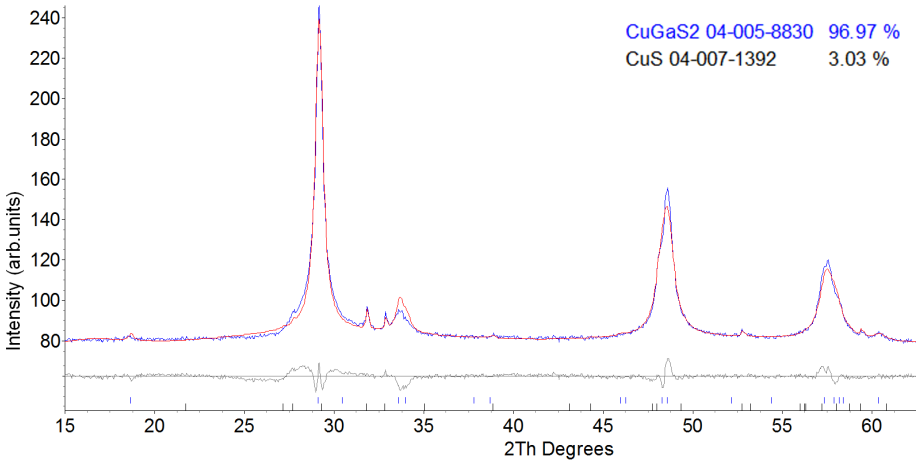

Figure 4.3: Synthesis 1: Rietveld refinement of the product, giving an under- and overestimation of the peaks corresponding to the $CuGaS_2$ phase, seen in the mismatch curve at the bottom.

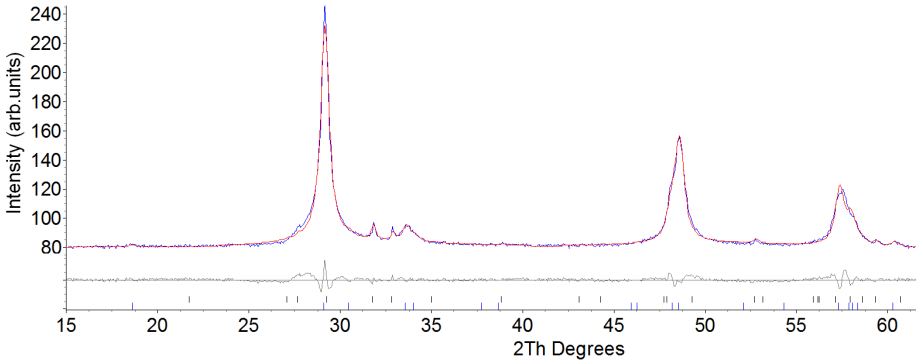

Figure 4.4: Synthesis 1: Pawley refinement on the $CuGaS_2$ phase, giving a low mismatch of refinement fit and data.

Synthesis 2 was done to make a preliminary investigation of the effect of reducing the reaction volume. It was indicated by Sortland[4] that a reduction in reaction volume also would reduce the product purity. This is contrary to what is expected, as a reduction in reactor volume should give less concentration gradients in the solution, and enhance the formation of a homogenous one- phase product. The volume of the autoclave in use was reduced from 125 mL to 23 mL. The diffractogram of the product of synthesis 2 (reduced volume) compared to synthesis 1 is showed in figure 4.5.

The phases identified are in both cases $CuGaS_2$ and CuS, the latter indicated with triangles. There seems to be very little difference in the product formed when reducing the volume of the autoclave.

The Rietveld analysis of the product also indicates this, where a phase purity of 91 at % $CuGaS_2$ was found. It should be noted that the peak intensity misfit was quite high, Pawley refinement gave a better fit to the data. The most accurate comparison will be to manually compare the diffractograms.

Synthesis 3, which is the last of the introductory syntheses, aims to make a preliminary investigation of the effect of increasing the pressure during the reaction by increasing the fill factor of the liner. This is the main suggestion made by Sortland for further work, based on the fact that most of the previous work done by others in the field is based on very high pressures in the autoclave, with autoclaves filled up to 95 %[60] of their capacity. The fill factor was therefore increased in synthesis 3, from 42% to 75 % of the capasity of the 23 mL liner. The diffractogram comparing low pressure, low volume (synthesis 2) with high pressure, low volume (synthesis 3) is shown in figure 4.5.

The phase identification showed the main $CuGaS_2$ phase, and possibly traces of CuS. It may be that if there is CuS present, it is in amounts too low for XRD detection. The diffractograms show that the peaks assigned to CuS at $2\theta =$ 31.9 and 32.9 angles is no longer apparent, meaning that the amount of CuS present has decreased. The Rietveld analysis of the diffractogram gave a good peak intensity fit for the standard mode. The quantified phase composition has therefore a much lower error than product 1 and 2. Nevertheless, the calculated composition of 97 at% $CuGaS_2$ and 3 at% CuS means that the absolute value of the secondary phase is within the detection limits of the method.

As can be seen from the diffracto indicates that an increase in pressure increases the phase purity of the sample. The Rietveld analysis of product 3 gave a good fit for the normal mode, meaning that the estimated phase purity of 97 at% has a low error margin.

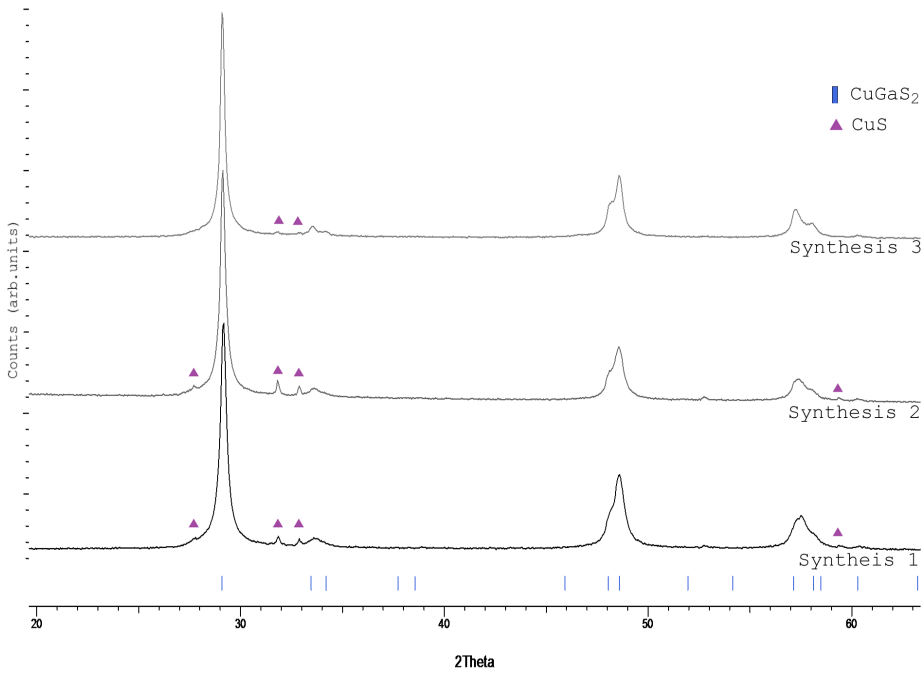

Figure 4.5: Diffractograms of Synthesis 1 (reproduction of 7a of Sortland,[4] Synthesis 2 (reduction of reactor volume) and Synthesis 3 (increased fill factor).

SEM analysis of the products show no clear trend in the morphology as a function of reactor volume, as products 1 and 2 have quite similar microstructures. It may look like the reactor pressure affects the morphology, as the mainly spherical structures in product 2 changes to a higher degree of fuzzy network structures in product 3. An overview image of the structures and an example of the most common structures in the powder is given in figure 4.6. The sphere-like particles present have many different surfaces, and it may look like there are two size distributions of the sphere- like particles. The average size of the sphere- like particles is decreased in synthesis 3, where the pressure is higher.

EDS measurements of the samples were made. A typical spectrum is shown in figure 4.7. The elements indicated in the spectra is Cu, Ga, S, Al and O. The latter two are most likely from the sample holder of aluminium with alumina layer on top, or from O_2 and H_2O attached to the product. Relative composition quantification based on the EDS data was not done, as the main target of the syntheses was to make introductory investigations on reproducibility, volume and pressure change on the overall phase composition.

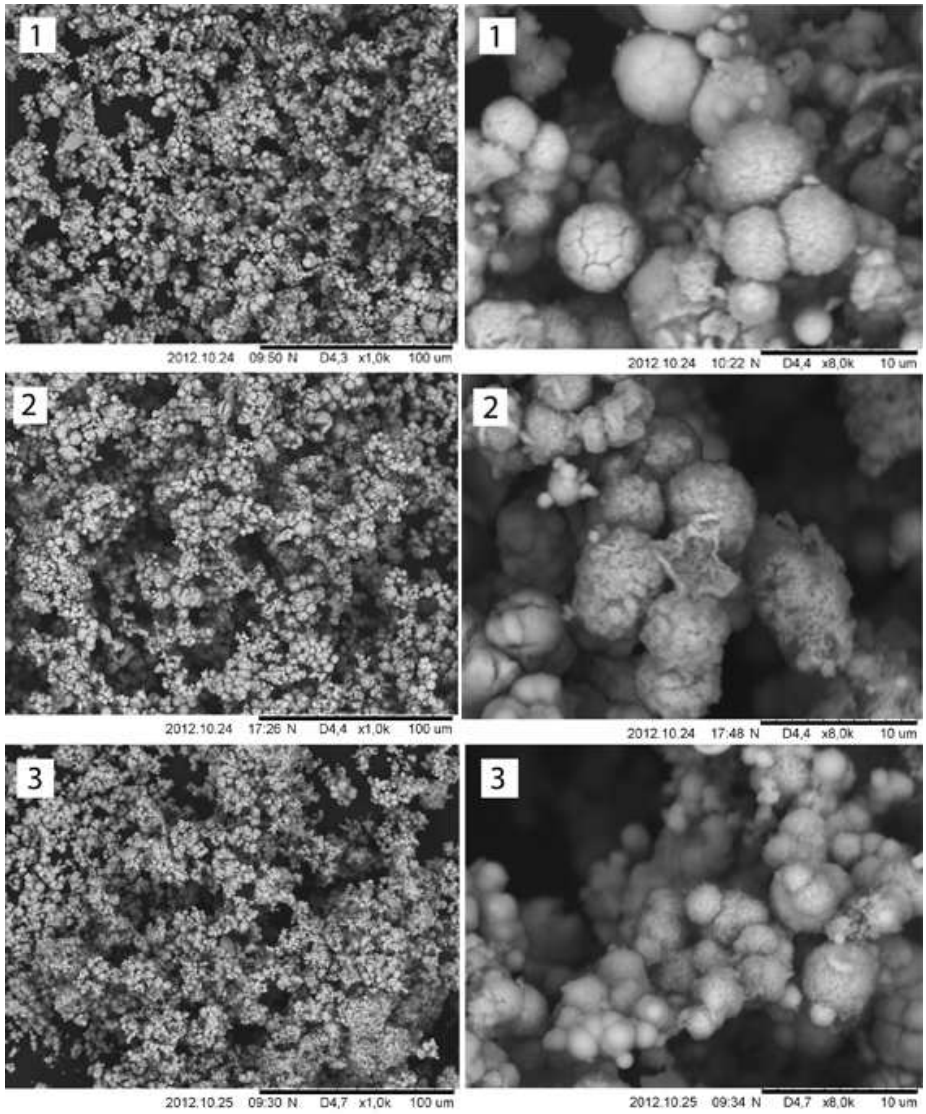

Figure 4.6: SEM images of synthesis 1, 2 and 3, with overview (100µm scale bar) and a closer view of the most common structures (10µm scale bar).

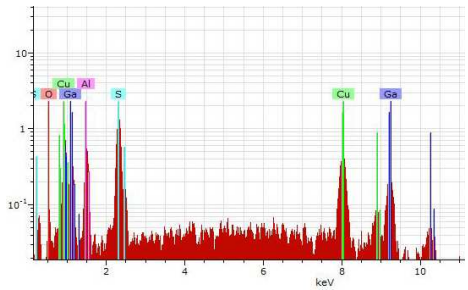

Figure 4.7: Typical EDS spectra for the close up views in figure 4.6.

4.2 Unsubstituted $CuGaS_2$

After these introductory syntheses, a parameter study of the unsubstituted $CuGaS_2$ was performed, to optimize this synthesis before a substitution was attempted. The goal was to make phase pure powder of $CuGaS_2$, since this would give the best starting point for substitution studies.

4.2.1 Fill factor and concentration

As indicated in the preliminary results section, the effect of changed fill factor can affect the purity of the product. Three fill factors were therefore chosen, as a means to investigate how the pressure change induced by using different fill factors affects the product. The lowest fill factor chosen was the one used by Sortland[4] in their best synthesis, which was 42 % filling of the autoclave. It was desirable to have the fill factor has high as possible, but the very high fill factors used by Hu et al.[60] were not possible to use, since this would exceed the pressure limitations of the autoclave used. A fill factor of 80 % was chosen as the highest limit, and as well as an intermediate fill factor of 60 %.

The work by Sortland[4] indicates that the precursor concentration seems to affect the product purity to a great extent, and the best concentration found by them was an order of magnitude larger than the litterature value of Hu et al.[60] It was decided to make a systematic study of the effect of concentration. Three precursor concentrations were chosen, the lowest based on the litterature value,[60] the highest based on the best product made by Sortland,[4] as well as an intermediate concentration. The stoichiometric relation between the elements was kept constant at Cu:Ga:S= 1:1:4.

An overview of the fill factor and concentration parameter study is given in

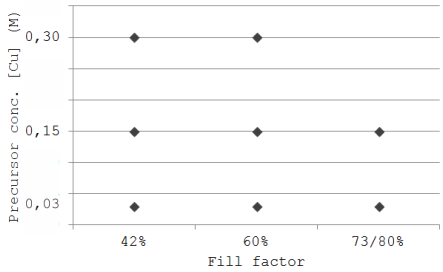

Figure 4.8: An overview over which parameters were varied for the eight unsubstituted samples.

figure 4.8, a detailed description is given in table 3.2.

The highest fill factors were not tested for all concentrations. The maximum fill factor for the temperature used (250 °C) was estimated to be around 80 %, based on the fill factor/ pressure/ temperature relation given by Walton et al.[75] shown in figure 2.25. This figure is based solemnly on the contribution from water in the vessel, evolution of gasses during the reaction is not accounted for.

During synthesis, it was found that it was indeed necessary to account for gases evolved. For the lowest concentration, the synthesis worked fine. For increased concentrations, the rupture disc of the vessel broke, due to too high pressures inside. The fill factor was decreased to 73 %, and the synthesis worked fine for the medium concentration. When the concentration was further increased, the rupture disc broke.

Due to safety concerns, no further studies were performed with the highest fill factor, meaning that the 3x3 synthesis matrix is reduced to a 2x3 matrix for the highest concentrations. This is unfortunate for the comparison of results, as a minimum three point comparison is the optimal.

The obtained products all had a distribution of fine and semi-fine powder texture, and a colour variation of orange-brown, red-brown, dark brown and black-brown. All products had a combination of these colour variations, with no apparent trend with regards to the synthesis parameters. Some flakes were obtained and these were very fragile and disintegrated to powder when transferred to a sample glass.

The diffractograms of the obtained products are presented in figure 4.9, sorted in groups of concentration and stacked by fill factor. The bottom three samples have low precursor concentration (0.03 M), the middle three medium

(0.15 M) and the top two have high precursor concentration (0.30 M).

The main phase of the products is the target phase $CuGaS_2$. The identified secondary phases are copper sulfide (CuS), gallium oxo-hydroxide (GaO(OH)) and the sulfate phases $CuSO_4 \cdot H_2O$ and $3\,Ga_2O_3 \cdot 4\,SO_3 \cdot 9\,H_2O$. The diffraction lines of the main $CuGaS_2$ phase are displayed, and the main peaks of the secondary phases are indexed.

The amount of the CuS phase present in the sample can be seen from a comparison of the height of the peaks at 2θ= 31.9 and 32.9 angles. The phase also has diffraction lines at 2θ= 47.8 and 58.0. For the samples with the highest CuS content, these peaks affect the $CuGaS_2$ peaks around 2θ= 48.5 and 57.5. The CuS peak at 2θ= 47.8 overlap with the $CuGaS_2$ peak at 2θ= 48.0 and "drags" the peak, giving an increased shoulder. The CuS peak at 2θ= 58.0 overlaps with the $CuGaS_2$ peak at 2θ= 58.1, giving a less visible shoulder.

For the lowest CuS contents, it is seen that the 2θ= 48 shoulder is low, and the 2θ= 57.5 peak is split. The peak shape is therefore most likely due to this secondary phase effect, and not a change in the $CuGaS_2$ unit cell.

The amount of the CuS phase also affect the shoulder of the main peak located at 2θ= 27.5. Higher CuS content gives a higher shoulder. The CuS content seems to be decreasing with increasing precursor concentration. Since this shoulder effect may be due to non-monochromatic irradiation from the instrument, a scan was done using monochromatic $K_{\alpha 1}$ irradiation. The result was a more or less identical diffractogram, leading to the conclusion that the shoulder is mainly an effect of secondary phases, not instrumental issues. The CuS is the only secondary phase present in all the samples. The fill factor does not seem to affect the CuS content at low concentration. For the medium and high concentration, it seems to be a slight decrease of CuS content with increasing fill factor.

The GaO(OH) secondary phase is only present in detectable amounts for the samples of low concentration. For this concentration, the amount of GaO(OH) is consistent for low and medium fill factors, and is highest for the highest fill factor. The sulfate phases $CuSO_4 \cdot H_2O$ and $3\,Ga_2O_3 \cdot 4\,SO_3 \cdot 9\,H_2O$ are only present in one sample, where the concentration and fill factor are lowest.

All in all, the purity of the product appears to be dependent on the precursor concentration, and not very dependent on fill factor. From the diffractograms it seems that 0.15- 0.30M precursor concentration, possibly combined with high fill factors gives the most phase pure product.

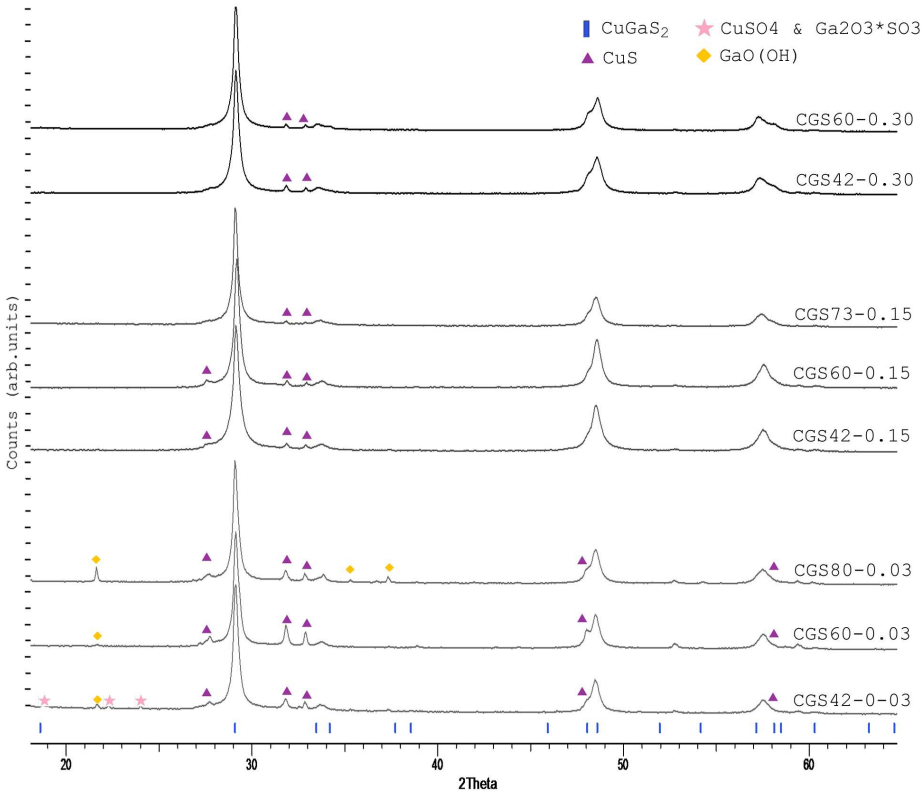

Figure 4.9: Diffractograms of unsubstituted $CuGaS_2$, grouped by precursor concentration and stacked by fill factor.

Rietveld refinement was used to quantify the phase composition of the samples, based on the peak position and intensities of the peaks. The calculated phase purity of $CuGaS_2$ for the different reaction parameters is compared to literature in figure 4.10. The calculated compositions correlates well with what was interpreted from the diffractograms, as it seems that 0.03M concentration gives a significantly lower phase purity than the rest. The effect of varying the fill factor is again not very prominent, as the uncertainties of the calculations are large. The literature comparison indicates that the samples of 0.30M are corresponding well to the results by Sortland,[4] but the 0.03M samples have a remarkably lower purity than that of Hu et al.[60]

The phase purity was calculated using Rietveld refinement with mismatch values (Rwp) were in the range 5.0-7.7. Pawley refinement on the $CuGaS_2$ phase was made, and this gave lower Rwp values in the range 3.3-5.0. Examples of typical Rietveld refinements and Pawley refinements are given in figure 4.11 and 4.12. Due to the lower mismatch value, all other refinements than the phase purity quantification was done using Pawley refinement.

In the diffractograms in figure 4.9 the position of the main $CuGaS_2$ appears to be shifting slightly towards higher Bragg angles and back for increasing fill factors. This may be an effect of changes in the unit cell, or a mechanical effect from sample preparation. Quantitative analysis of the structure was made by Rietveld refinements in the hkl mode. It is stressed that the calculation error is strongly affected by secondary phases, and especially the samples of 0.03M precursor concentrations should not be emphasized. The calculated unit cell volumes are in the range of 298.8-300.1 $Å^3$, see figure 4.13.

The peak shape of the main peak at $2\theta = 29$ indicates that there is a wide size distribution, possibly a bimodal size distribution of small crystallites (causing the wideness of the peak) and larger crystallites (causing the narrowness and height of the peak). The peak shapes of the remaining peaks are changing, but this is most likely an effect of overlapping diffraction lines with the CuS secondary phase, as discussed above.

The average Lauritzian crystallite size in the samples was calculated to be in the range of 20-30 nm. This size is an average of all crystallites and any bimodal size distribution would not be seen. This is not possible to quantify using Rietveld analysis within the given refinement structure.

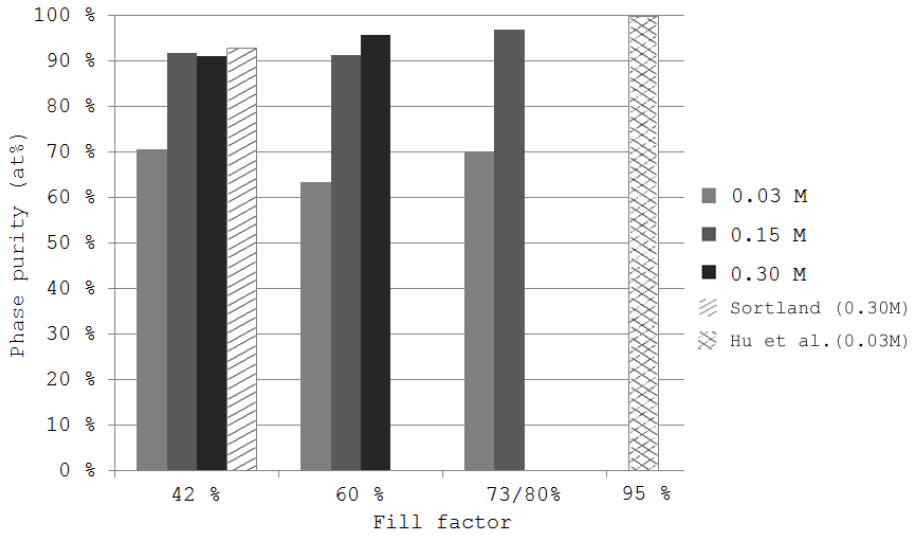

Figure 4.10: Phase purity of samples with varying precursor concentrations and fill factors. The Rwp values are in the range of 5.0-7.7, large errors in the calculated numbers must be expected. Litterature purities are also included from Sortland[4] and Hu et al.[60]

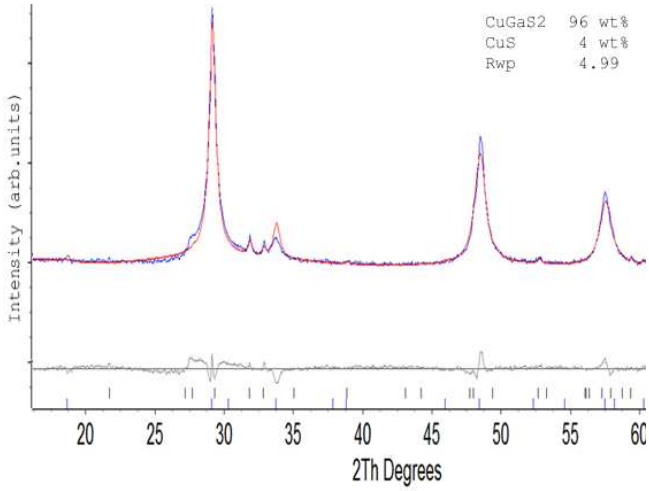

(a) Rietveld

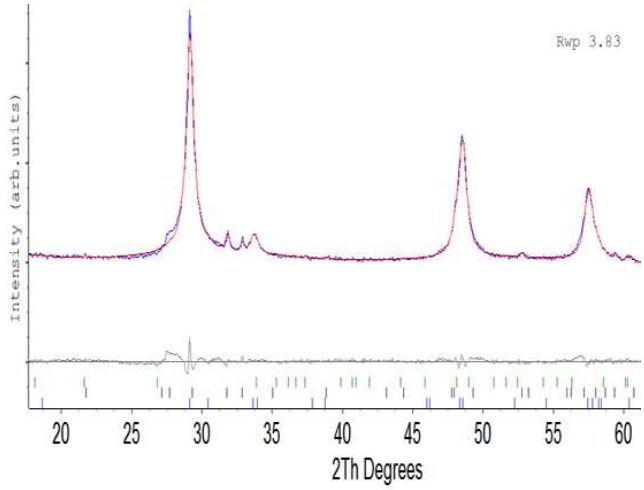

(b) Pawley

Figure 4.11: Rietveld and Pawley refining of $CuGaS_2$ in CGS42-0.15. The mismatch of calculated fit and data is shown in the mismatch curve at the bottom, and given by the Rwp value.

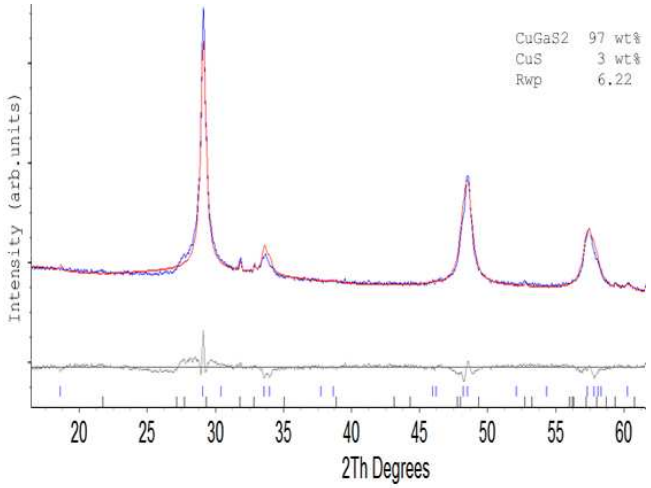

(a) Rietveld

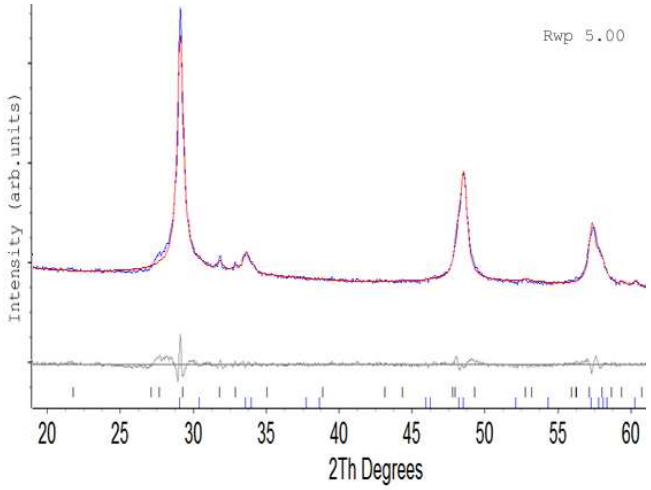

(b) Pawley

Figure 4.12: Rietveld and Pawley refining of $CuGaS_2$ in CGS73-0.15. The mismatch of calculated fit and data is shown in the mismatch curve at the bottom, and given by the Rwp value.

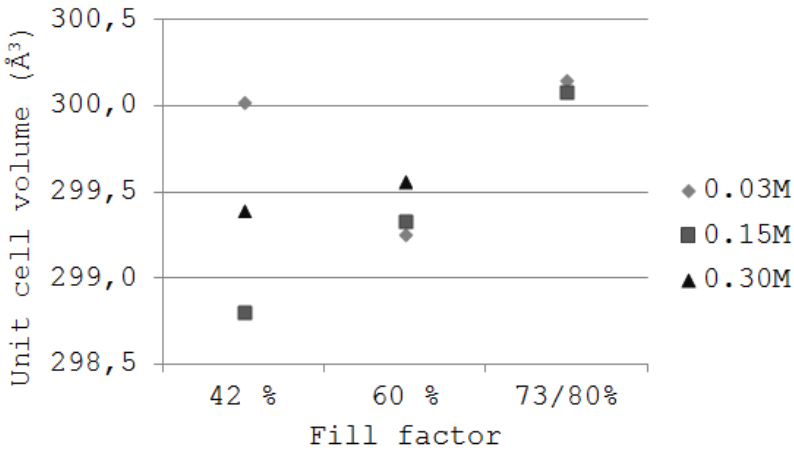

Figure 4.13: Unit cell volume for the samples of varying fill factor and precursor concentration. The 0.03M samples have poor calculation fits, and therefore large uncertainties are involved.

SEM images of the products are showed in figure 4.14. A large range of microstructures were found. A representative image of the most common structures is shown in figure 4.15.

The microstructure seems to be changing with concentration, especially when increasing from 0.03M to 0.15M concentration. The sphere- like structures go from being very irregular to more regular. The irregular spheres for 0.03M seems to have grown in preferred directions, making the structures plate-like, or even starfruit-like. The more regular spheres of 0.15M and 0.30M have varying surfaces; rough, fuzzy and smooth surfaces are represented. Some of the spheres seems to have cracked, displaying an inner sphere and outer layer surrounding it. The highest concentration has more uniform microstructures.

Increased fill factor seems to have little effect on the microstructure, although it is difficult to extract trends from such a complex microstructure.

A typical EDS spectra for the samples is shown in figure 4.16. The elements indicated in the spectra is Cu, Ga and S. The different microstructures shown in figure 4.15 were found to have equivalent EDS spectras.

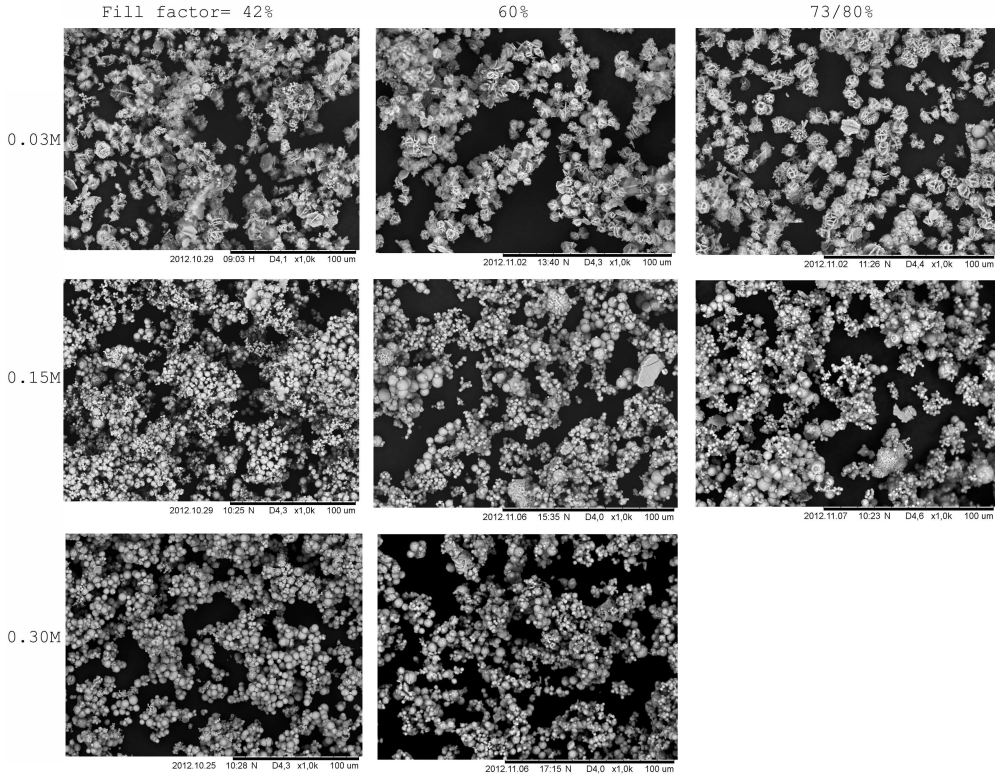

Figure 4.14: SEM images of the unsubstituted $CuGaS_2$, showing effect of fill factor and precursor concentration on the microstructure. The scale bar is 100 μm.

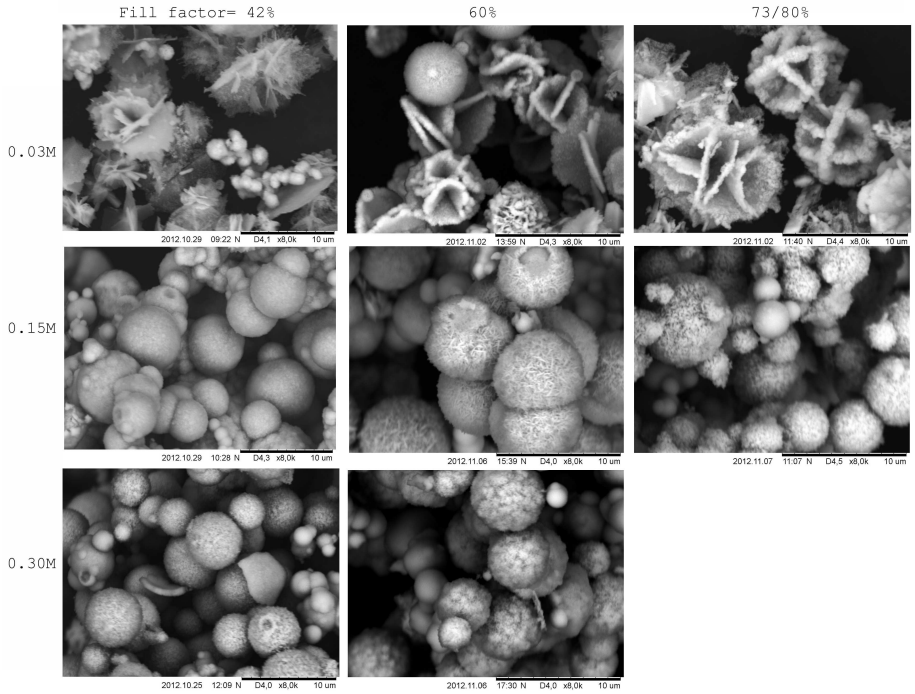

Figure 4.15: SEM images of the unsubstituted $CuGaS_2$. The scale bar is 10 μm.

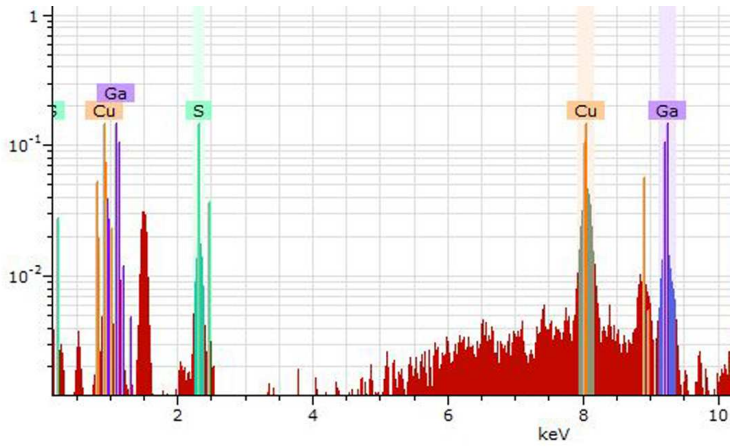

Figure 4.16: A typical EDS spectrum for the unsubstituted samples. Cu, Ga and S is labeled. The peak of Al (1.5 keV) and O (0.6 keV) is from the aluminium sample holder with oxide layer.

4.2.2 Effect of sulfur excess

The stoichiometric composition of the previous syntheses was based on a 1:1 relation of Cu:Ga and a four times excess of sulfur. The extent of the sulfur excess is not specified by Hu et al.,[60] which is the "model" synthesis for this work. Zhong et al.[62] and Sortland[4] uses a four times excess of sulfur. It was decided to test the effect of four versus five times sulfur excess in the precursor solution, giving the stoichiometric relation of Cu:Ga:S of 1:1:4 and 1:1:5.

For the study, medium concentration was chosen since this is an intermediate between the low concentration used by Hu et al.[60] and the high concentration used by Sortland.[4] The fill factors chosen were 42% and 60%, a detailed overview of reaction parameters is given in table 3.3, section 3.3.

The obtained powders all consisted of red-brown fine powder and dark black-brown semi-fine powder. The diffractograms of the powders are given in figure 4.17, grouped by fill factor and stacked by 4x and 5x sulfur excess.

The amount of the CuS secondary phase seems to be slightly higher for the products with 4x sulfur excess compared to 5x sulfur excess. This is based on a decrease in the intensities of the 2θ peaks at 31.9 and 32.9. The shoulder at $2\theta = 27.5$ does not indicate a decrease in the CuS content.

It was previously found that the peak shape of the $2\theta = 48$ and 57.5 peaks

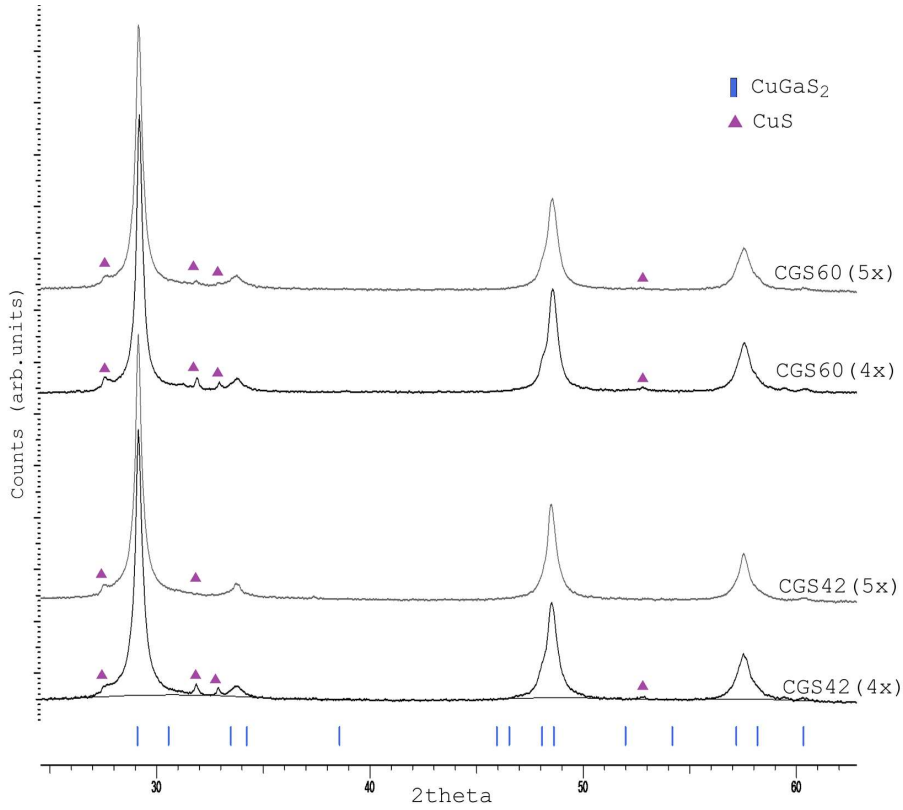

Figure 4.17: Diffractograms of products with 4 and 5 times sulfur excess, with 42 % and 60 % fill factors. The main peaks from the secondary phase, covellite (CuS) is indexed with triangles.

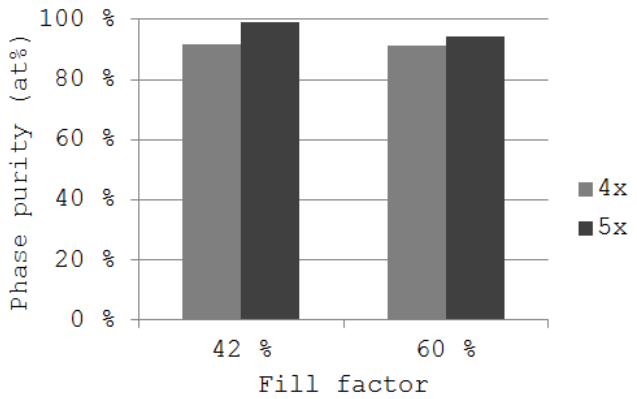

Figure 4.18: Phase purity of $CuGaS_2$, for 4x and 5x sulfur excess in precursors.

are affected by large changes in the CuS content. Since these peaks remain unchanged the relative change in the CuS content for 4x and 5x excess is not very large. The peak shape and position of the main peak at 2θ remains unchanged, indicating that the unit cell of the $CuGaS_2$ phase is unaffected by the sulfur content of the precursors.

Rietveld analysis in the standard mode was made giving phase composition quantification with Rwp values of 5.0-5.6. The phase purity of $CuGaS_2$ is presented in figure 4.18 and it is again stressed that the high Rwp values leads to uncertainties in these calculations.

SEM investigation of the products were made, see figure 4.19. The overall microstructure does not seem to be affected by the sulfur stoichiometric contribution. The main structures are spheres and sphere-like structures, most spheres are whole, some are broken displaying an inner sphere with an outer shell. The overall size of the structures does not seem to be affected by the sulfur content.

The EDS spectra collected for 4x and 5x sulfur are similar to that presented in figure 4.16, and showed no apparent difference when varying the sulfur content.

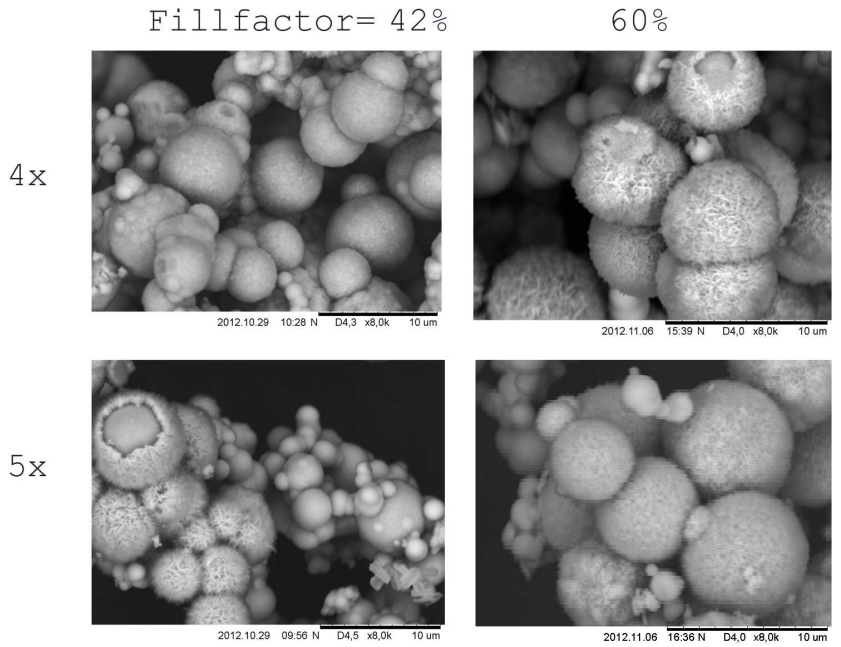

Figure 4.19: SEM images of samples with varying precursor sulfur content and fill factor.

4.3 CGFS: Substitution site

4.3.1 Substitution site

10 % iron substitution into the $CuGaS_2$ lattice was attempted, aiming for substitution to Ga-site (Fe_{Ga}) and Cu-site (Fe_{Cu}) by varying the stoichiometric composition of the precursors. For Fe_{Ga} substitution, the sum of n_{Fe+Ga} added up to n_{Cu}, and opposite for Fe_{Cu} substitution. Four times sulfur excess was used, the fill factor and precursor concentration were varied in the same manner as for the unsubstituted experiments, to enable comparisons.

12 samples were made, 6 of Fe_{Ga} and 6 of Fe_{Cu}, an overview is given in figure 4.20. A detailed description of all synthesis parameters and sample names are given in table 3.4 for Ga-substitution and table 3.5 for Cu- substitution, section 3.3.

The obtained products were light grey, dark grey and black, with no apparent difference in the colours of the Ga- and Cu-substituted samples. The texture was fine to semi-fine powder. There were some fragile flakes that disintegrated when transferred to a sample glass.

The diffractograms of the products are sorted by 42 % fill factor in figure 4.21 and 60 % fill factor in figure 4.22. The bottom three diffractorgrams are Ga- substituted samples, the top three are Cu- substituted, all stacked with increasing precursor concentration. Figure 4.21 and 4.22 are more or less identical and will therefore be evaluated together.

The phase identification gave several secondary phases. In addition to the phases already found in the unsubstituted samples, a cubic pyrite FeS_2 phase was identified. The phase has distinct diffraction lines at 2θ angles 33, 40.8 and 56.2.

For the Fe_{Cu} samples with concentration 0.03M, there is a peak at 2θ= 31, in addition to a high 2θ=27.5 shoulder. The origins of these peaks are unclear. A Ga_2S_3 phase was suggested in the EVA software for the peaks, but this did not give a good refinement for the 2θ=31 peak when a Rietveld refinement was tried with the phase. The shoulder is difficult to refine, due to the high overlap with the main peak of $CuGaS_2$. The Ga_2S_3 phase is suggested as a possible, but not certain explanation of the peak. The peak is not seen in any of the other samples.

The amount of all secondary phases are in the range of the lower limit of XRD detection. Nevertheless, trends may be extracted.

The CuS secondary phase is present in detectable amounts in the Fe_{Ga} substituted samples, the amount is decreasing with increasing concentration. The

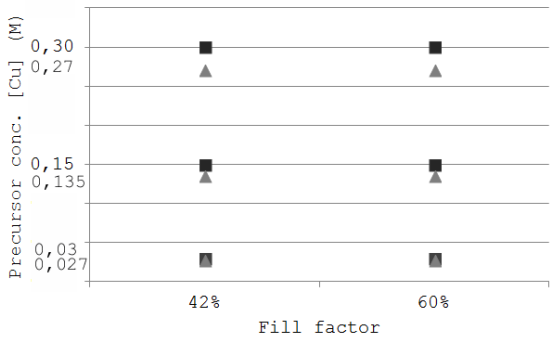

Figure 4.20: An overview of the parameter variations of the substituted syntheses. Fe_{Ga} substitution is indexed with squares, Fe_{Cu} with triangles.

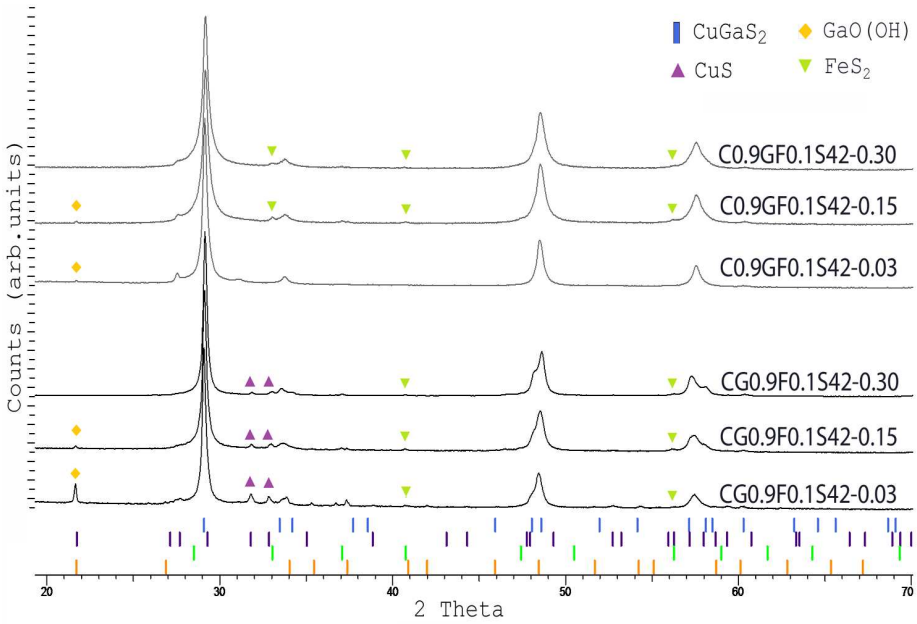

Figure 4.21: Diffractograms of substutited $CuGaS_2$ samples of 42 % fill factor. Bottom three: substitution to Ga-site. Top three: substitution to Cu-site. The main peaks from the secondary phases are indicated.

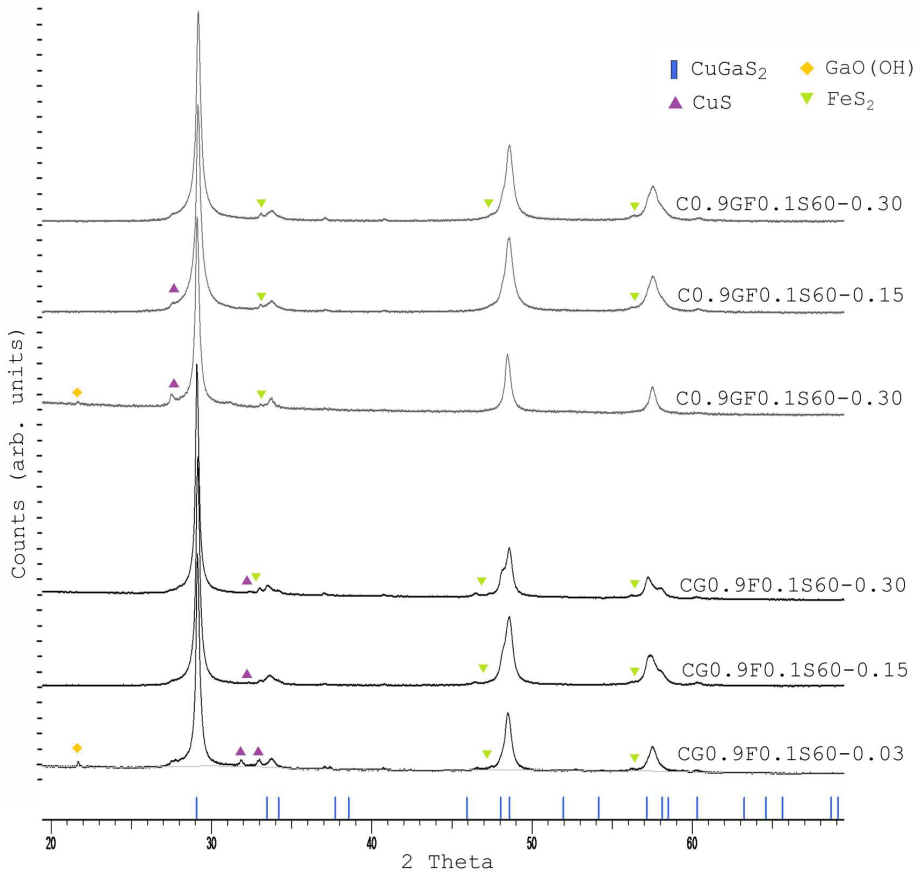

Figure 4.22: Diffractograms of substituted $CuGaS_2$ samples of 60 % fill factor. Bottom three: Fe_{Ga}, top three: Fe_{Cu}. Secondary phases are indexed.

GaO(OH) phase is present in the 0.03M and 0.15M samples for 42 % fill factor, and only in the 0.03M samples for 60 % fill factor, for both Fe_{Ga} and Fe_{Cu}. The overall amount of GaO(OH) is highest for the Fe_{Ga} samples. The iron rich secondary phase, FeS_2 is present in all samples except one ($C_{0.9}GF_{0.1}S42$-0.03), any trend of the quantity is difficult to extract due to the very low amounts.

The phase identification of the main phase gave several chalcogenides as alternatives, since the diffraction lines are similar for $CuGaS_2$ and $CuFeS_2$. For the iron rich $CuFeS_2$ to be the main phase, the composition of the precursors should contain equal amounts of copper and iron. Since the amount of iron in the precursors is very low compared to Cu and Ga, having $CuFeS_2$ as the main phase would give very large amounts of Cu-rich and Ga-rich secondary phases. It is seen from the diffractograms that this is not the case, and it was therefore concluded that the main phase most likely was $CuGaS_2$.

The peak shape and shifts differentiates the Fe_{Ga} from the Fe_{Cu} samples for both fill factors, especially for the 2θ= 29.1, 48.5 and 57.5 peaks, see figure 4.23. For the Fe_{Ga} samples, the peaks are splitting with increased concentation, while for Fe_{Cu} the peaks are remaining one peak and are shifted toward higher Bragg angles. The results indicate that Fe_{Ga} samples are following the same trend as the unsubstituted samples, where the CuS content affects the peak shape of these peaks, as discussed in section 4.2.1, while the Fe_{Cu} samples are distinguishable from the unsubstituted samples.

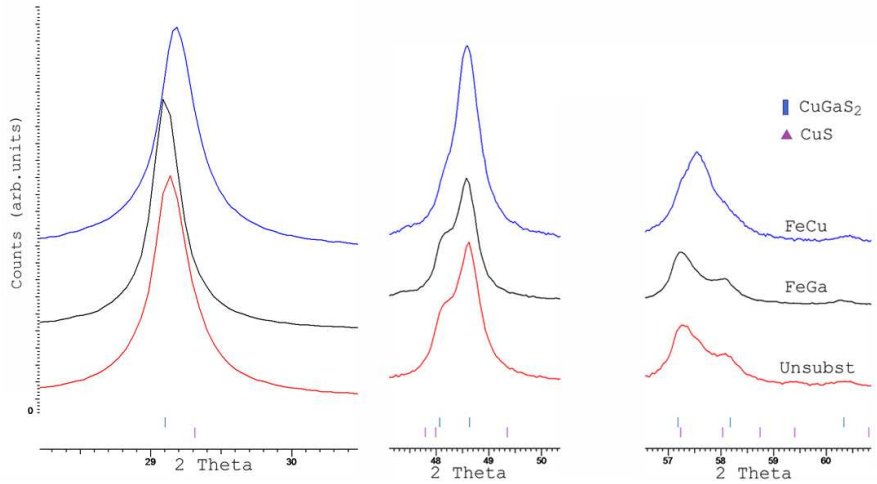

Figure 4.23: A comparison of the two substitution sites and an unsubstituted sample. All three have 60% fill factor and an overall precursor concentration of 0.30M.

A Rietveld analysis was done to confirm that the phase identification was correct. The assumption of $CuGaS_2$ as the main structure was confirmed, since that phase gave a lower mismatch than refinements based on the $CuFeS_2$ phase. The CuS, FeS_2 and GaO(OH) phases were all found to be present for the cases described above. Pawley refinements gave lower refinement mismatch, and was used to calculate lattice parameters and unit cell volumes. The a and c lattice parameters are presented in figures 4.24(a) and 4.24(b) respectively. For comparison, the Fe_{Ga}, Fe_{Cu} and unsubstituted $CuGaS_2$ are plotted together.

The a parameter is increasing with increasing precursor concentration, and the c parameter is decreasing, for both substitution sites and for the unsubstituted $CuGaS_2$. The a parameter is larger for Fe_{Ga} than Fe_{Cu}, for all concentrations. The c parameter is smaller for Fe_{Ga} than Fe_{Cu}, for all concentrations.

The unit cell volumes were calculated from the a and c parameters, see figure 4.25. The volume was on average larger for the substituted samples compared to the unsubstituted. It is difficult to extract any other trends.

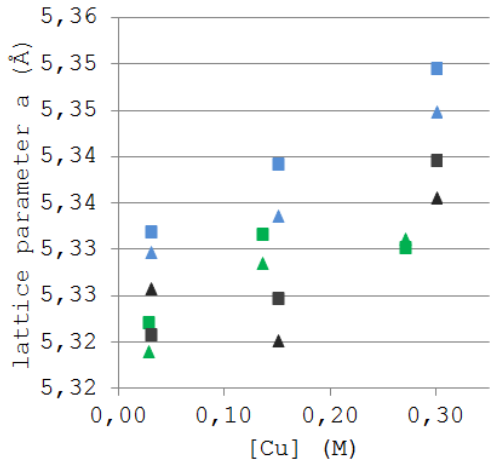

(a) Lattice parameter a

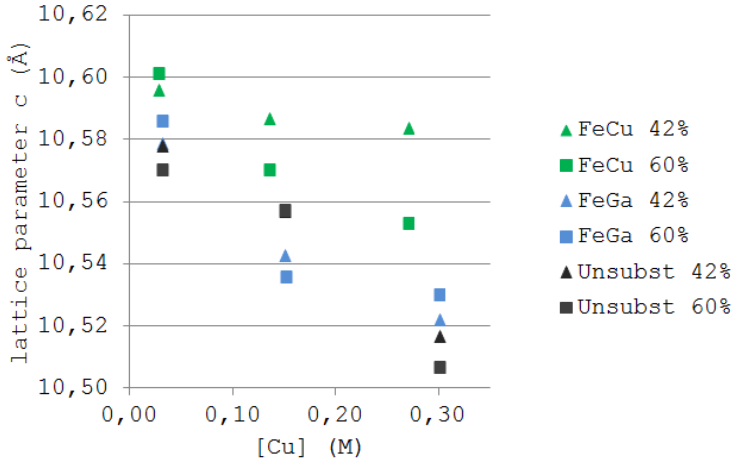

(b) Lattice parameter c

Figure 4.24: Lattice parameters for Fe_{Ga}, Fe_{Cu} and unsubstituted $CuGaS_2$. Fill factor (42 and 60%) and precursor concentration is indicated.

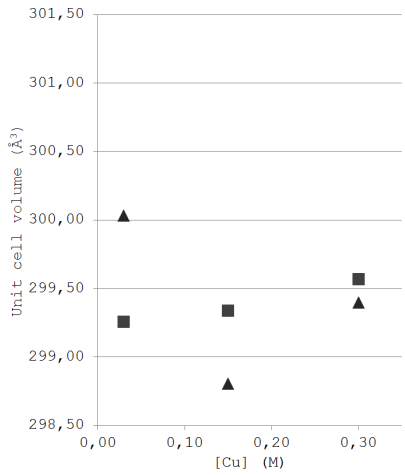

(a) Unsubst

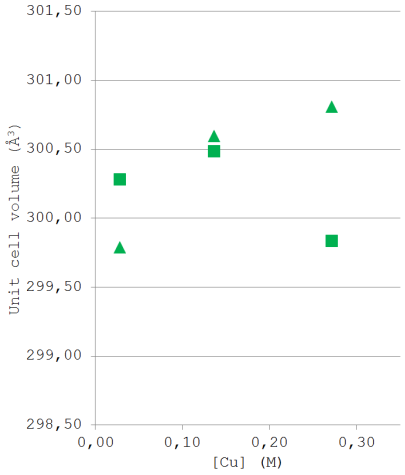

(b) Fe_{Cu}

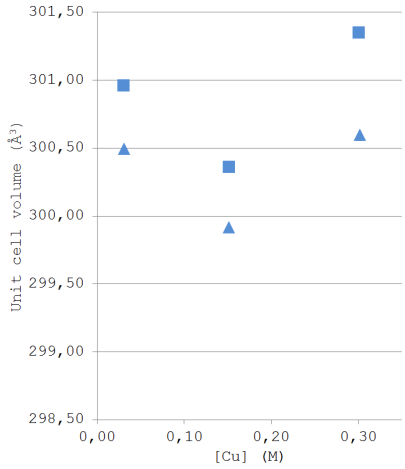

(c) Fe_{Ga}

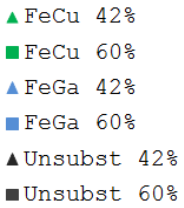

Figure 4.25: Unit cell volumes for unsubstituted, Fe_{Cu} (middle) and Fe_{Ga} (right) substituted $CuGaS_2$, calculated by Pawley refinement.

SEM investigations were made of the samples. As for the unsubstituted products, a large range of particles were found. The microstructures did not seem to be affected by the different substitution sites.

It was decided to do a detailed EDS mapping of the different microstructures of $CuGaS_2$ and identify the microstructures of the secondary phases in the samples. The interest in identifying the composition of the different microstructures lies in obtaining a general understanding of the system, as well as a possible future thin film application, where microstructures are important.

The EDS mappings are presented by a SEM image, combined with an elemental compositional EDS images of the same frame for Cu, Ga, S, Fe and O. A quantification of the elemental composition of the circled area of the SEM image is presented in a pie chart. The composition analysis was used to estimate which phase the different particles represent.

Several microstructures of $CuGaS_2$ were identified; regular spheres is given in figure 4.26, spheres with inner and outer shell, broken spheres and irregular sphere-like structures are presented in Appendix B. The relative amount of Cu:Ga:S indicates that all of these microstructures are $CuGaS_2$. As can be seen from the pie chart, there is a small amount of iron present in all structures. It should be noted that the EDS quantification has an uncertainty of a few atomic percent.

The microstructures of GaO(OH) was identified as 2-20 μm long rods, an example is given in figure 4.27. The phase was found in the samples where it was detected by XRD analysis.

An example of the FeS_2 microstructure is given in figure 4.28, crystallites of distinct growth directions and in some cases pyramidal shapes. It was found in all samples, including those where the amount was too low for XRD detection.

The microstructure of CuS was identified as irregular spheres an order of magnitude larger than those identified as $CuGaS_2$, see figure 4.29. The CuS phase was not identified in all samples where it was identified using XRD. This may be due to sample preparation, where an ultrasonic bath was used to make a dispersion of the particles, before they were dripped onto the sample holder. The large (17-30 μm) CuS particles may have sunk to the bottom of the Eppendorff tube and thus not been transferred to the sample holder for all samples. The image presented here is from the samples in section 4.4.

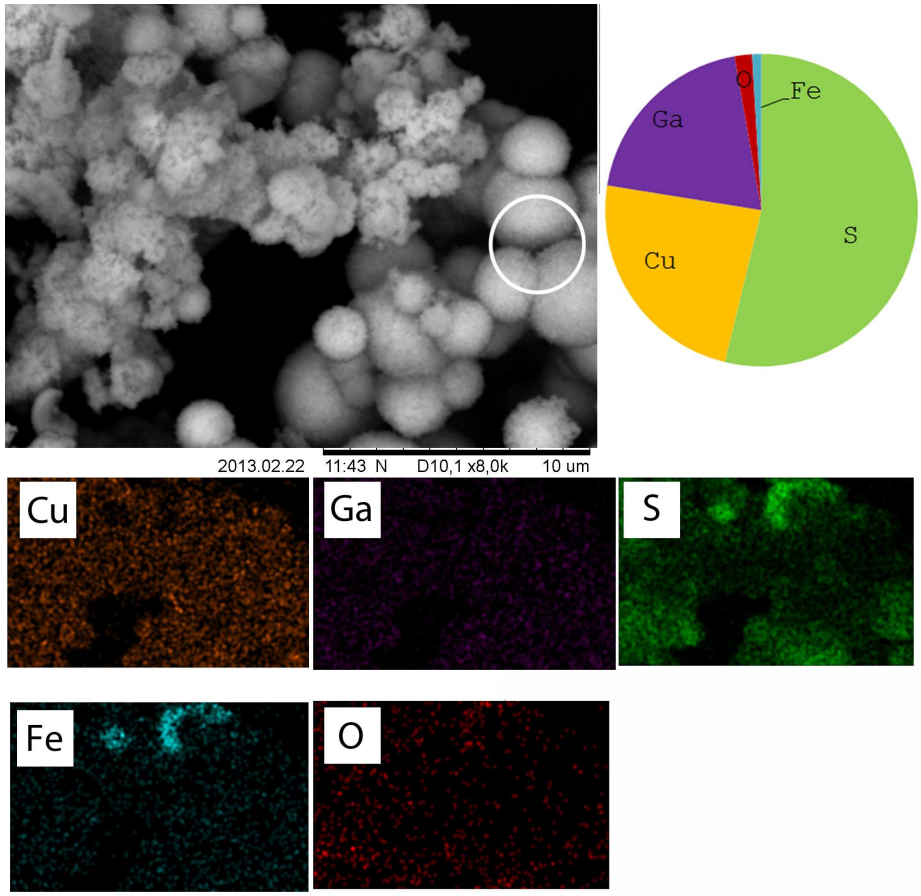

Figure 4.26: SEM images and EDS analysis of regular and irregular $CuGaS_2$ spheres, The image is taken from sample $CG_{0.9}F_{0.1}S42$-0.30.

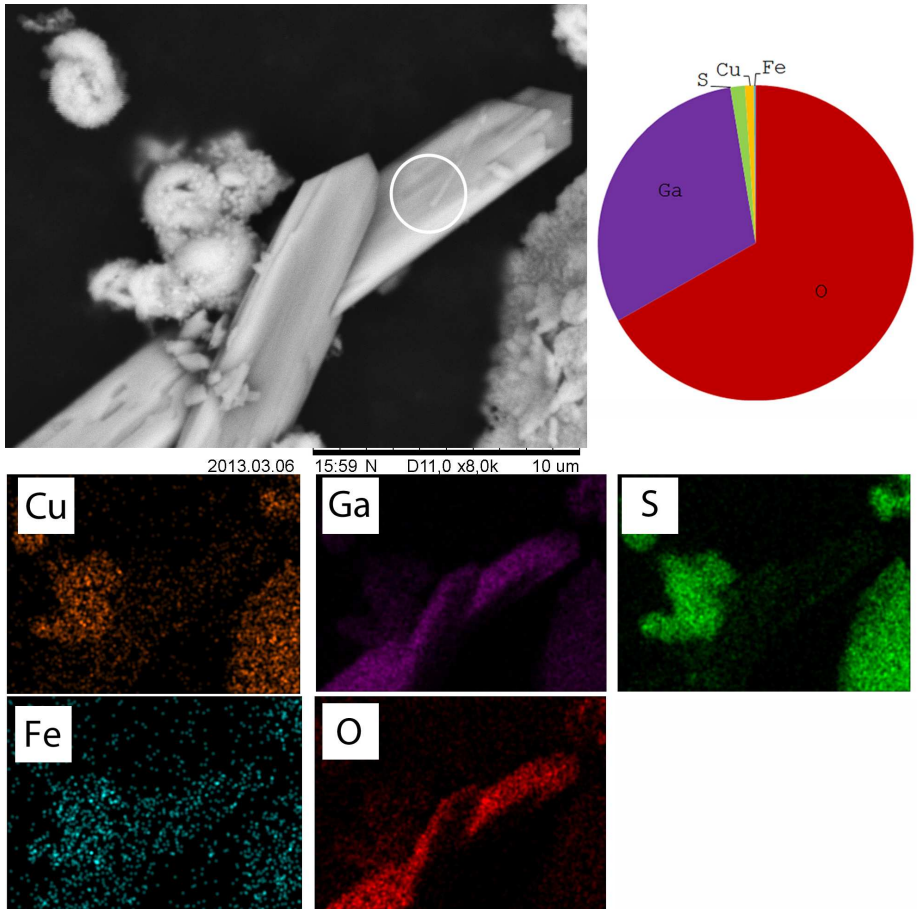

Figure 4.27: SEM images and EDS analysis of GaO(OH) microstructure, the rods are 3.5 x 35 µm. The image is taken from sample $CG_{0.9}F_{0.1}S42\text{-}0.03$.

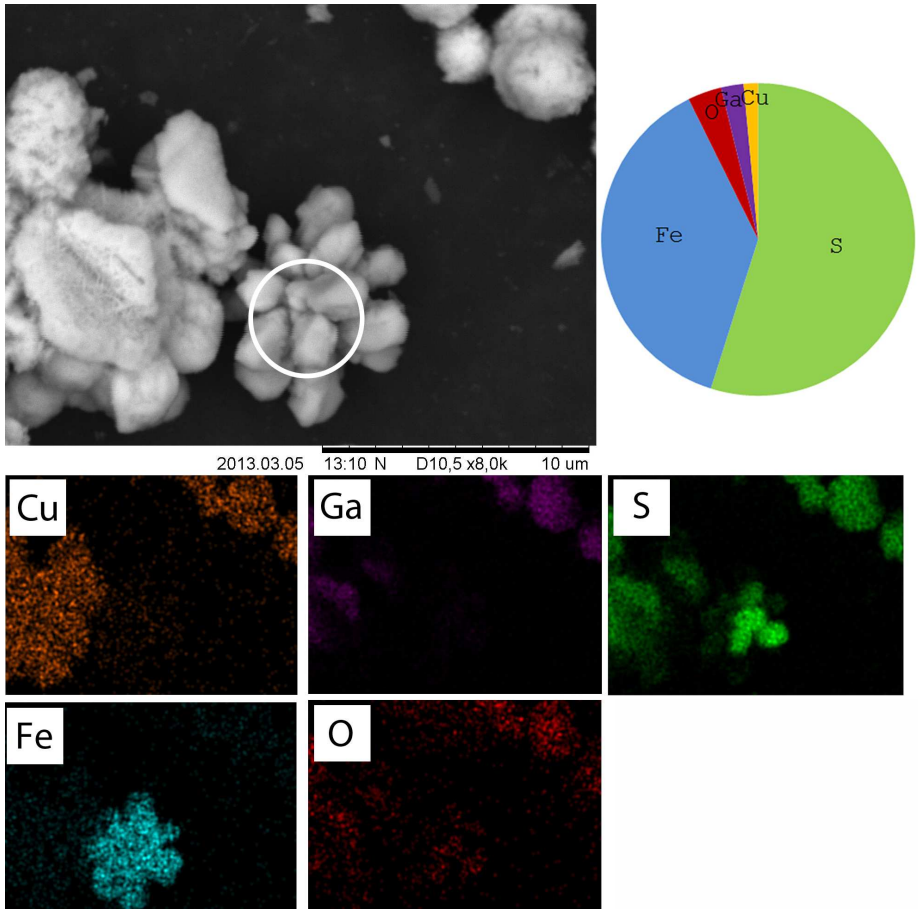

Figure 4.28: SEM image and EDS mapping of FeS_2 microstructure. The images are from sample $C_{0.9}GF_{0.1}S4$2-0.03.

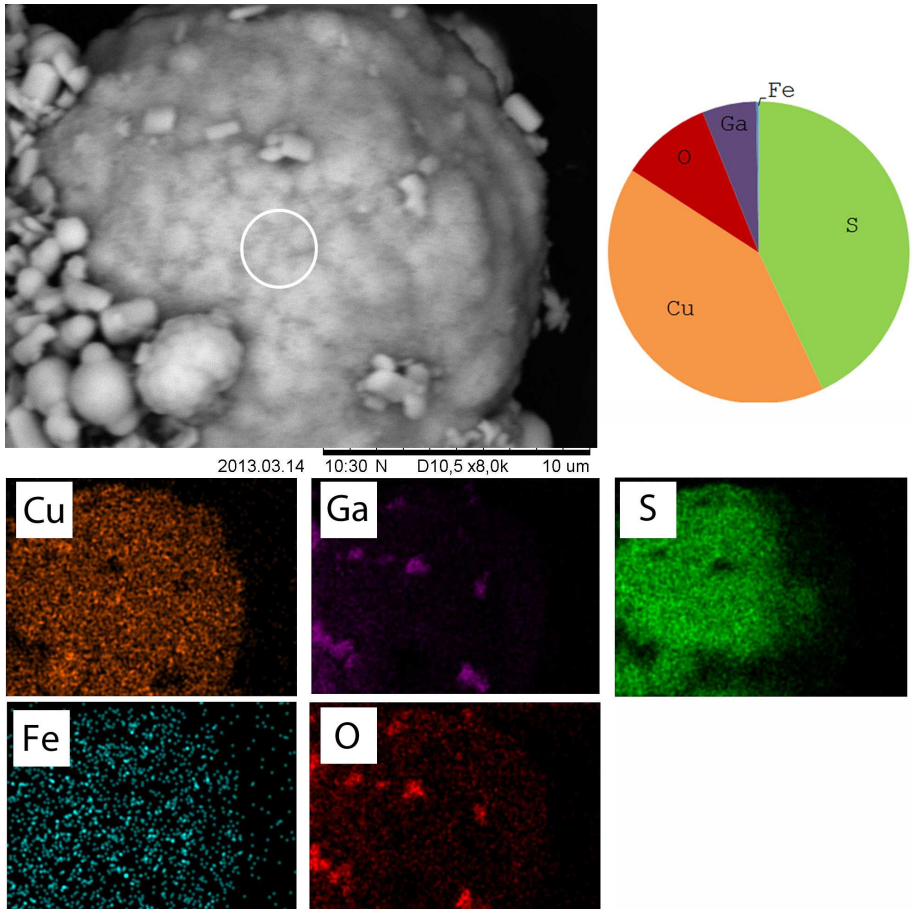

Figure 4.29: SEM image and EDS mapping of CuS microstructure. The images are from sample CGFS200-1, in section 4.4.

4.3.2 Reproducibility

A reproduction of selected samples was done to investigate the reproducibility of the synthesis, as the preliminary experiments indicated that reproduction in hydrothermal conditions might be challenging. The selected samples were a series of 0.03M, 0.15M and 0.30M Fe_{Ga} with 60 % fill factor, as well as one 0.03M Fe_{Cu} also with 60 % fill factor, indicated with ρ in tables 3.4 and 3.5.

Diffractograms of original and reproduced products are displayed in figure 4.30. Secondary phases are indicated with indexes. The results show a various degree of reproducibility, as the amount of secondary phases in the original and reproduced sample are not the same. The 0.30M Fe_{Ga} sample appears to have the best reproducibility, based on similar diffractograms. A Rietveld compositional quantification was made, see figure 4.31. The Rietveld analysis is consistent with the XRD analysis, as a higher phase purity is calculated where the XRD pattern shows a low amount of secondary phase, perhaps with the exception of 0.30M Fe_{Ga}, where the XRD patterns are quite similar.

4.3.3 Absorption properties

A diffuse reflectance UV-vis spectroscopy measurement was performed, the data was converted to absorption intensities, to give the absorption properties of selected samples. The samples used had the same fill factor, and varying precursor concentrations. Samples of the two substitution sites as well as an unsubstituted sample was measured. The results are presented in figure 4.32 where the bottom measurement is the unsubstituted, the next three are for Fe_{Ga}, the top three are for Fe_{Cu}. For reference, the band gap of $CuGaS_2$ is 2.4 eV, transitions related to an intermediate band in the band gap is expected at 1.9 eV (VB-IB) and at 0.7 eV (IB-CB).

Due to very high signal noise, there is little data to be extracted from the measurements. When comparing the unsubstituted with the substituted samples, there seems to be little difference.

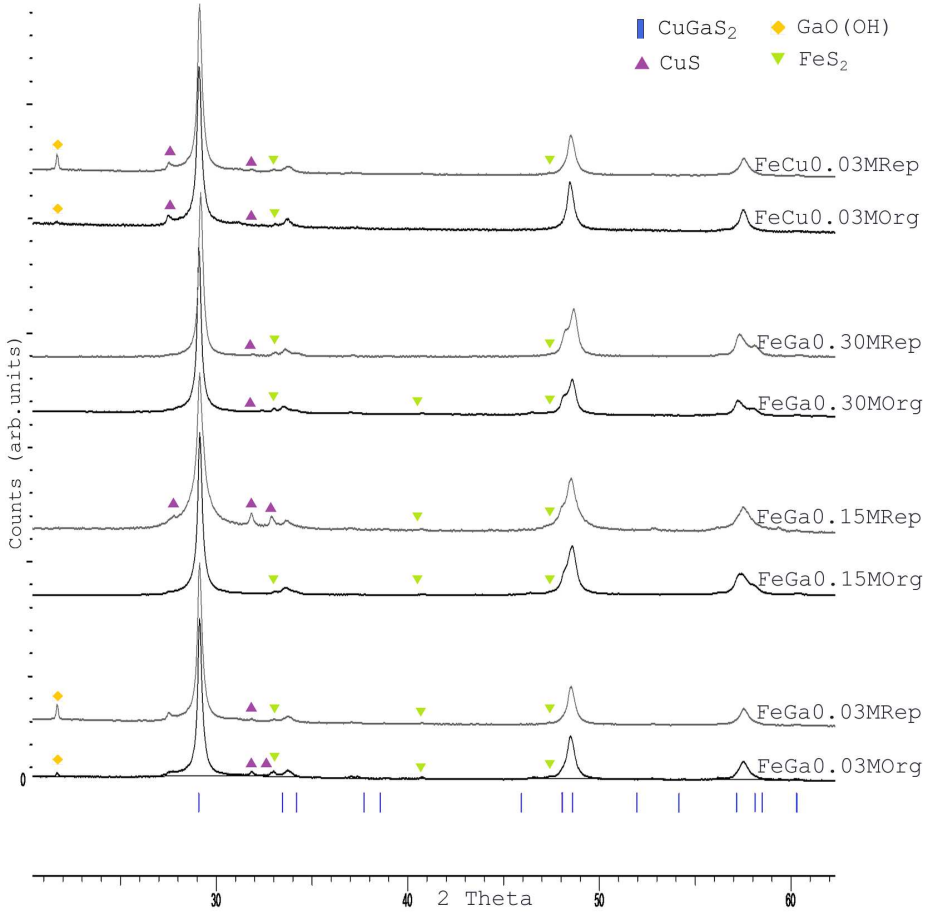

Figure 4.30: Diffractograms of original (black) and reproduced (dim gray) samples. Secondary phases are indexed.

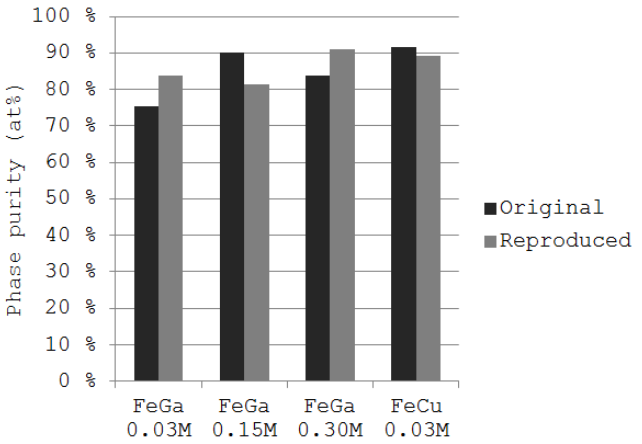

Figure 4.31: Rietveld calculations of phase purity of original (black) and reproduced (gray) samples.

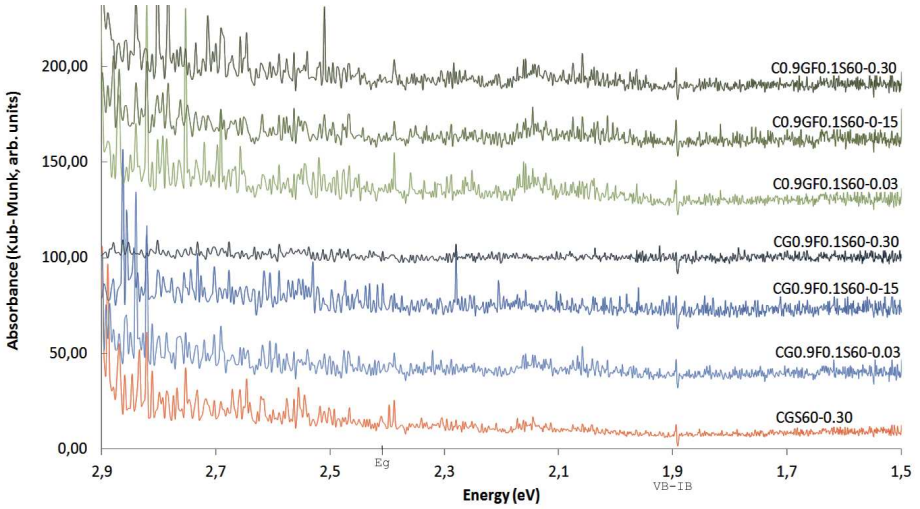

Figure 4.32: Kubelka-Munk transformed absorbance measurements of an unsubstituted sample (bottom), three Fe_{Ga} substituted and three Fe_{Cu} substituted samples (top three).

4.3.4 Calcination experiment

Calcination of the $C_{0.9}GF_{0.1}S60\text{-}0.30$ sample was carried out in air and in inert atmosphere with the aim of making a single-phase powder of iron substituted $CuGaS_2$. This sample was chosen since it was one of the most phase pure products obtained. The temperature of 800 °C was chosen based on the phase diagram in figure 2.22. The diffractograms in figure 4.33 shows the powder before calcination (bottom), calcined in air (middle) and calcined in inert atmosphere (N_2-flushing). For both calcination atmospheres the powder was oxidized, and a powder of $CuGa_2O_4$ and CuO was obtained.

Rietveld refinement on the products was made, giving a peak intensity problem for some of $CuGa_2O_4$ peaks in the standard mode (Rwp of 6.43). A quantification of the phase composition could have given an estimation of the composition before and after calcination, if the calculation had been more accurate. The quantifications are not included here, due to the large errors from the peak intensity misfit.

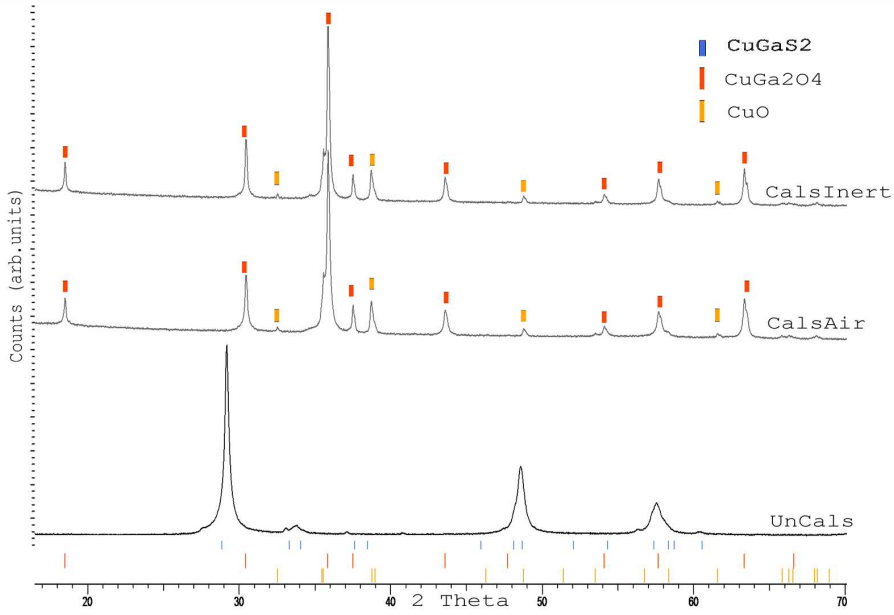

Figure 4.33: Diffractograms of the $C_{0.9}GF_{0.1}S60\text{-}0.30$ sample; not calcined (bottom), calcined in air (middle) and calcined in inert N_2 atmosphere (top).

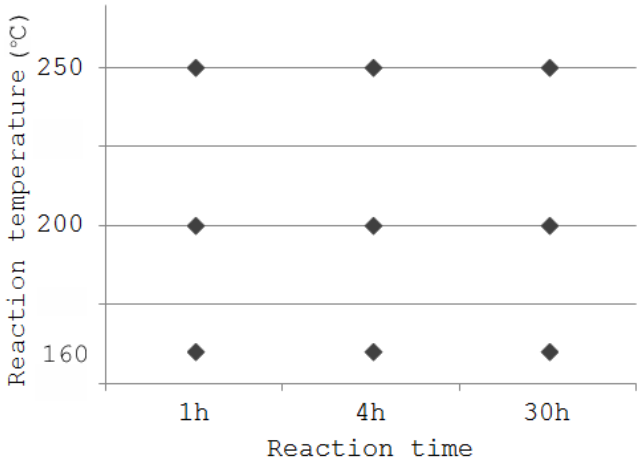

Figure 4.34: Overview of the samples made with various reaction temperature and times.

4.4 CGFS: Temperature and time

A further parameter study of the hydrothermal synthesis of iron substituted $CuGaS_2$ was done, to investigate the effect of changed reaction time and temperature, an overview is given in figure 4.34. Table 3.6, section 3.3 gives a detailed parameter description. The goal was to get more information on the nucleation and growth processes in the system.

The lowest temperature (160 °C) was based on that used by Hu et al.,[60] the highest (250 °C) based on the best product of Sortland.[4] It was chosen not to investigate lower temperatures than 160 °C, based on previous results by Zhong et al.[62] An additional temperature was therefore chosen as the intermediate 200 °C, to enable a three-point comparison. The reaction times chosen were also based on Hu et al. (4h), Sortland (30h), in addition a very short reaction time (1h) was chosen with the aim of makin preliminary investigations on reaction mechanisms. The concentration chosen was medium concentration (0.15M), with Fe_{Cu} substitution site and 60 % fill factor.

The masses of the obtained products were very varying, despite having the same precursor concentrations. The lowest mass obtained was for the CGFS160-1 sample, an increase in the obtained mass was achieved for increasing either reaction time and temperature.

The obtained powders were of different colours. The very low mass of the CGFS160-1 sample makes colour distinction difficult, but the product appeared to be a light grey fine powder. CGFS160-4 was partially red-brown, partially dark grey fine powder and fragile flakes. CGFS200-1 was consisted of light and dark grey fine powder and fragile flakes. The remaining products were all medium to dark grey and black, the texture was fine to semi-fine powder and fragile flakes.

The diffractograms of the obtained products are grouped by temperature and stacked by time in figure 4.35 and opposite in figure 4.36. The main peaks of the secondary phases CuS, GaO(OH) and FeS_2 are indicated. The bottom diffractogram has high noise to signal ratio, due to the very low mass of the sample.

For low temperatures (160 °C), the shortest reaction time gave 100% GaO(OH), and very little product mass. Increasing the reaction time gives a drastic decrease of the relative amount of GaO(OH) present, as several other phases have formed, including the target phase $CuGaS_2$. For a further increase in the reaction time, there is a decrease of the amount of all secondary phases in favour of the $CuGaS_2$ phase.

For medium temperatures (200 °C) , the most drastic effect of increasing the reaction time is for the increase from 1-4 hours, as the amount of secondary phases are lowered substantially relative to the $CuGaS_2$ phase. All secondary phases are still present, though. A further increase to 30 hours reaction time makes the amount of GaO(OH) and FeS_2 undetectable, and gives a decrease of the CuS secondary phase to a near undetectable amount.

For high temperatures (250 °C) , the short reaction time of 1 hour already gives a large amount of the target $CuGaS_2$ phase. An increase in reaction time to 4 hours gives a lowered amount of all secondary phases, the amount of GaO(OH) becomes undetectable. Increasing the reaction time to 30 hours decreases the amount of CuS further still.

The diffractograms grouped by reaction time have the same trends; an increase in temperature gives an overall decreased amount of secondary phases present. The exception is the increased temperature of 200-250 degrees for 30 hour reaction times, where there seems to be no change in phase purity. These two samples (CGFS200-30 and CGFS250-30) are the most phase pure of all.

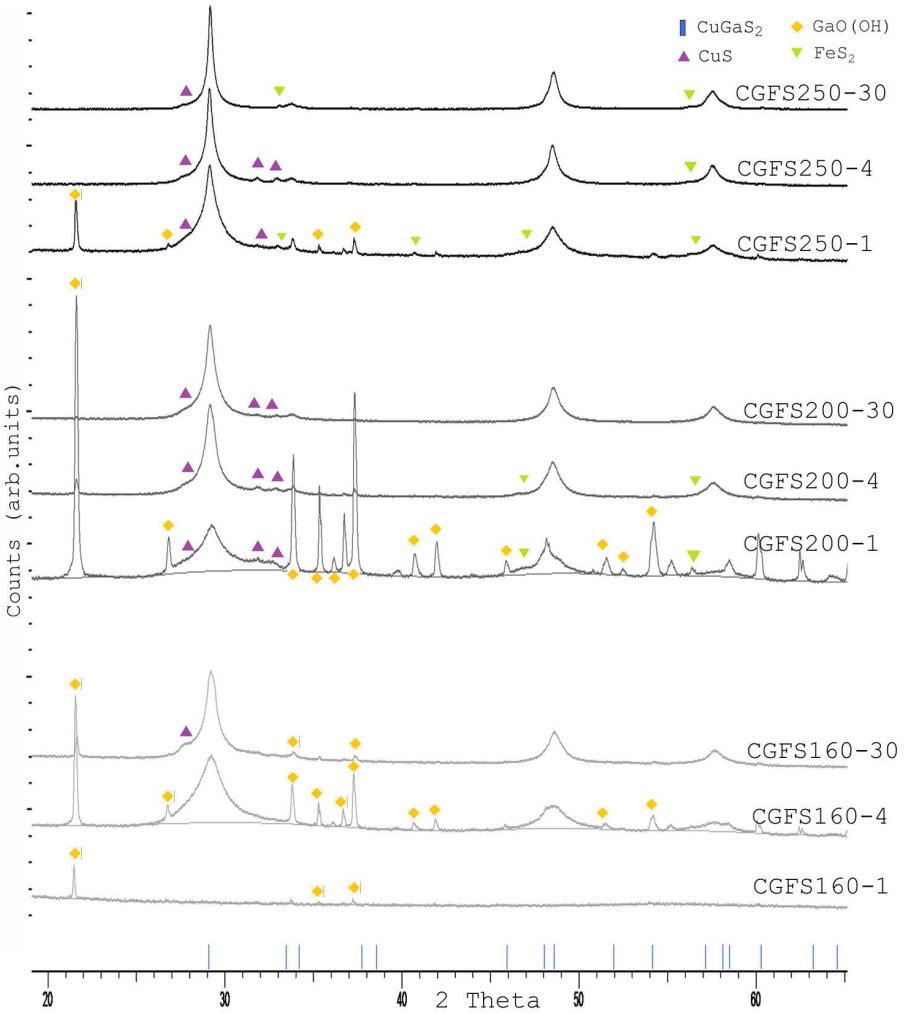

Figure 4.35: Diffractograms of samples of varying reaction temperature and time, grouped by temperature.

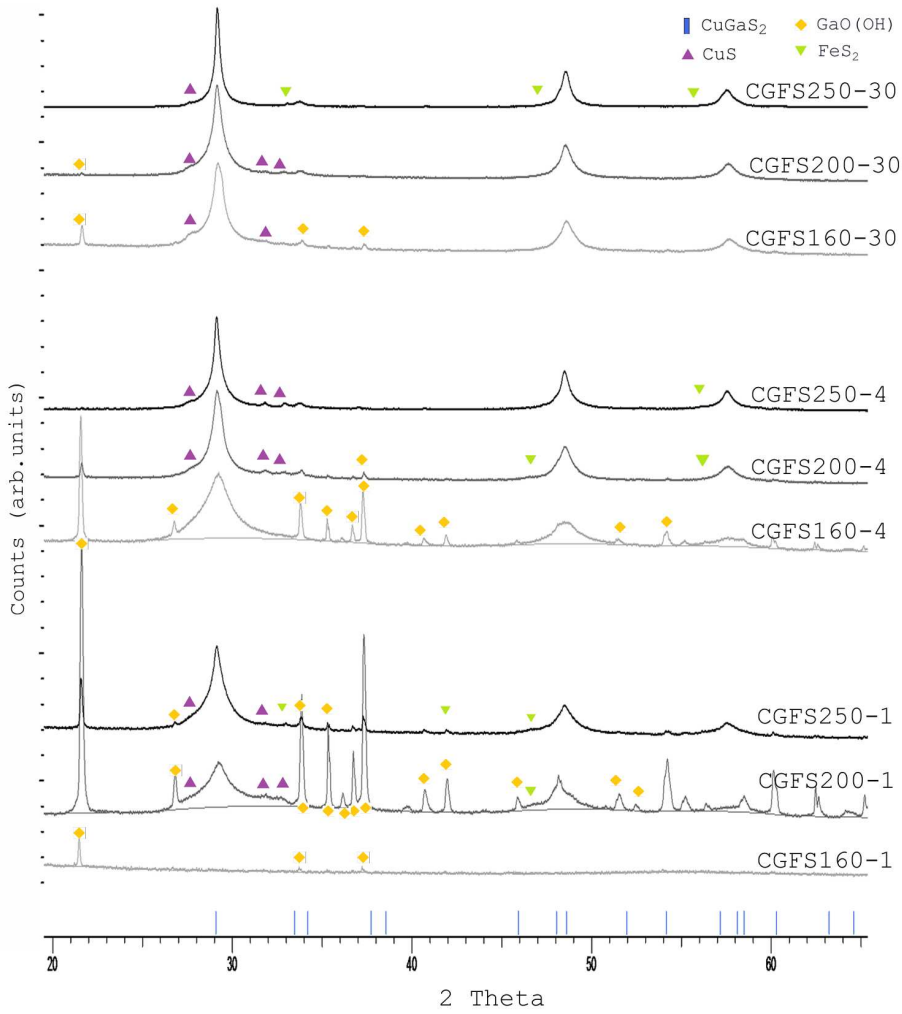

Figure 4.36: Diffractograms of samples of varying reaction temperature and time, grouped by reaction time.

A Rietveld analysis was made to quantify the composition of the products. High Rwp values were obtained , due to high amounts of secondary phases.

For the sake of understanding the formation of secondary phases as a function of the reaction parameters, a plot of the amount of secondary phases present is made, see figure 4.37. In the plot, the same trends as described above are seen; the GaO(OH) phase is abundant for low temperatures and reaction times; The amount of GaO(OH) is reduced with increasing either reaction time or temperature; The amount of CuS is increased, and then decreased again as the reaction time and temperature is increased. The FeS_2 secondary phase is not present in any detectable amounts for low reaction times or temperatures, but increases as the temperature and reaction time increases.

The phase purity of $CuGaS_2$ from Rietveld refinement is presented in figure 4.38. The trends found from the analysis of the diffractograms are in correlation with what is calculated here, an increase in reaction time and temperature gives a higher phase purity. The exception is again the samples of 30 hour reaction time, where there is not a distinguishable difference between the 200 °C and 250 °C.

The shape of the diffraction peaks related to the $CuGaS_2$ phase, show that an increase in temperature gives a narrowing of the peak, for all reaction times. This is especially visible for the main peak with Bragg angle $2\theta = 29$.

The crystallite size of the samples were calculated using Pawley analysis, see figure 4.39. The Pawley refinements had a better fit to the data than the Rietveld refinements, and these calculations were therefore used for the crystallite sizes. The 1h products are excluded from the analysis, as they contain very high amounts of secondary phases, causing a large uncertainty in the calculations. The calculated crystallite size increases with increased temperature, which is in correlation with the observed narrowing of the main $CuGaS_2$ peak at $2\theta = 29$ in the diffractograms.

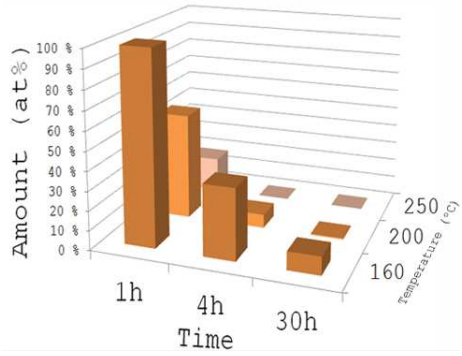

(a) GaO(OH)

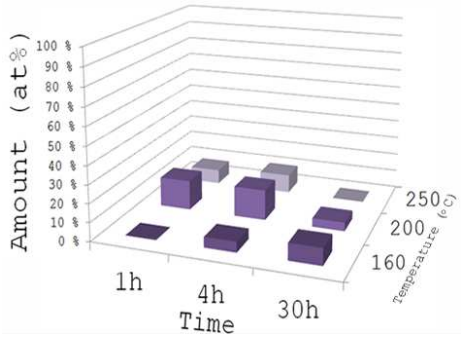

(b) CuS

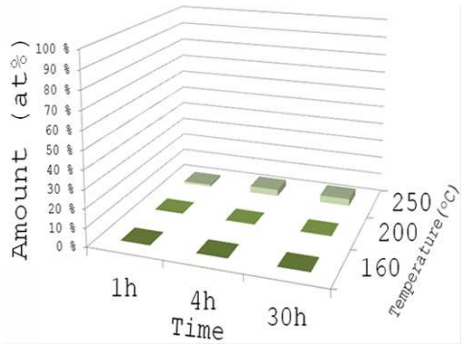

(c) FeS_2

Figure 4.37: Amount of the secondary phases GaO(OH), CuS and FeS_2 for different reaction times and temperatures, found using Rietveld calculations.

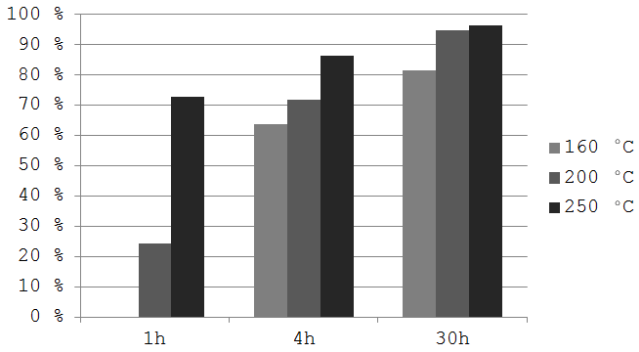

Figure 4.38: Rietveld calculations of phase purity of the $CuGaS_2$ phase of the products with varying reaction temperature and time.

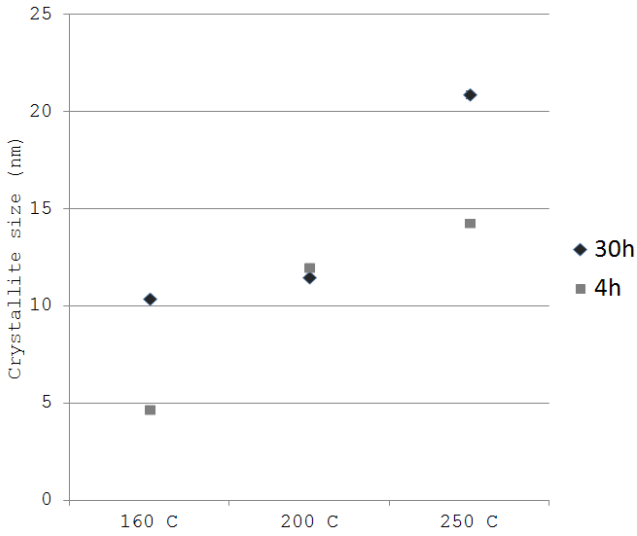

Figure 4.39: Calculated crystallite sizes for samples of 30h reaction time and varying temperatures.

SEM images were taken of all samples, except CGFS160-1 due to the very low amount of product obtained. An overview is given in figure 4.40, and a closer view of the most common particles is given in figure 4.41.

EDS was used to identify points of interest in the overviews, and these were investigated by mapping the elemental composition. Based on this, the microstructures of the different phases was identified. The findings corresponded well with what was found previously; the $CuGaS_2$ phase consisted of spheres and sphere-like structures in the size range of 2-6 μm, and in some cases large flakes or large fuzzy structures in the 20-40 μm size range; The CuS phase was identified as large sphere like structures; the GaO(OH) phase as rods and the FeS_2 phase as highly crystalline structures and in some cases pyramides. It should be noted that the observed microstructures are agglomerates of smaller crystallites, so the crystallite sizes found by Pawley calculations are not the same as the observed microstructures.

The relative amount of each phase seen in the SEM images correlates well with the phase composition analysis done by XRD. For low temperatures and reaction times, there are a lot of GaO(OH) rods. Increasing either temperature or reaction time gives less GaO(OH) rods.

The FeS_2 phase was not found for the CGFS160-4 sample. All remaining samples were found to contain FeS_2, also those with too low content for XRD detection. The FeS_2 phase was most common in the products with 250 degree reaction temperature.

The relative amount of $CuGaS_2$ microstructures increases with increasing reaction time for all temperatures. Increasing the reaction temperature from 1 to 4 hours gives the most significant increase of $CuGaS_2$. For 30 hours reaction time there is a decrease in the amount of GaO(OH) rods present when increasing from 160 to 200 degrees. There is no clear difference between 200 and 250 degrees for this reaction time. This correlates well with the phase composition in the diffractograms, and the Rietveld analysis of these.

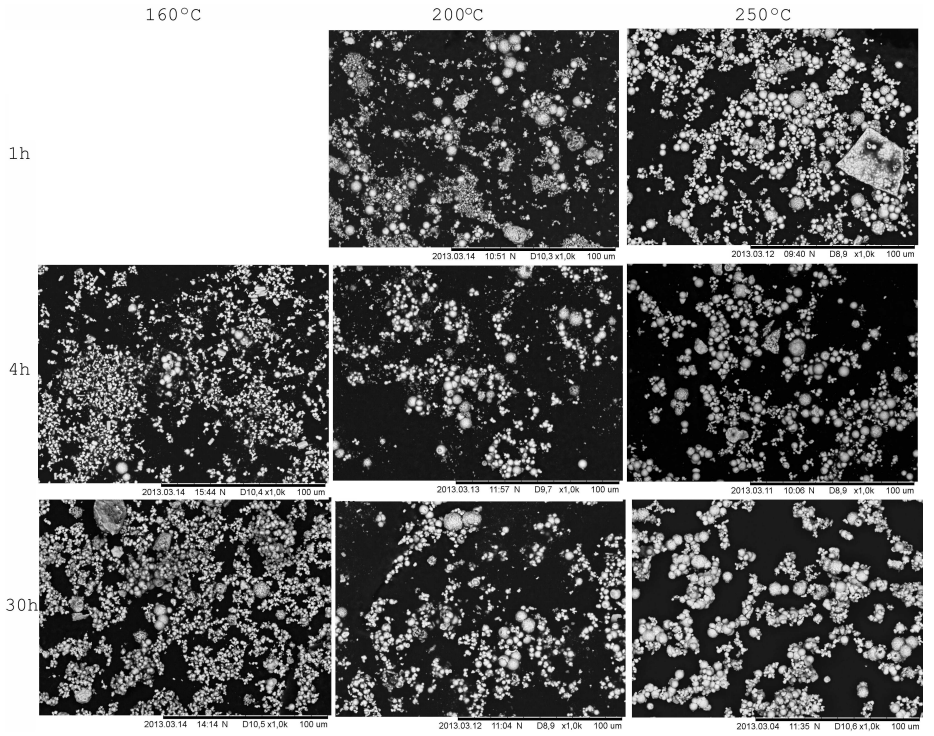

Figure 4.40: Overview of the microstructures found in products with varying reaction time and temperature. The scale bar is 100 µm.

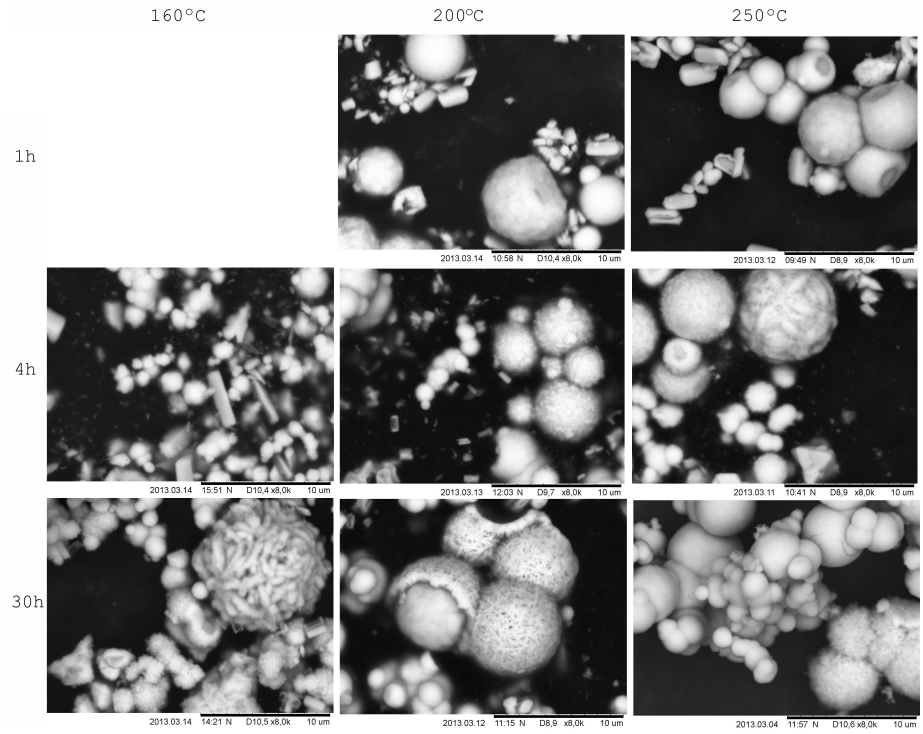

Figure 4.41: Close-up of the most common structures of products with varying reaction time and temperature. The scale bar is 10 μm.

5 Discussion

5.1 Preliminary experiments

The first experiments were conducted to make preliminary investigations to provide guidelines for further work.

Reproducing previous work gave the same phase purity, but different secondary phases were present. This indicates that the hydrothermal conditions were not entirely uniform in the original and reproduced sample. This may be due to small deviations in the reaction conditions or equipment, which may give differences in the composition of the products as different phases nucleate under different conditions. Based on these findings, it appears that a precise reproduction under hydrothermal conditions may be challenging.

Reducing the autoclave volume was found to have little effect on the phase purity of the product, as expected. As long as the content of the solution in the autoclave is unchanged, the thermodynamic and kinetic conditions remain unchanged, and there is no reason why a decrease in the overall volume would affect the product. If any, the product should be more homogenous, since there will be a smaller concentration gradient in the solution. The XRD results and the microstructures found do not indicate any significant changes in the products with changed reactor volume. It was concluded that a smaller reactor could be used without affecting the product. Being able to change the scale of the reactor without large changes in the product will be beneficial for future up-scaling for applications in the solar cell industry. It should be noted however, that an industrial scale-up should include stirring of the solution during reaction to avoid gradients in concentration, temperature, pH and other parameters in the solution.

Increased fill factor was found to increase the phase purity. This is in accordance with the phase pure product made by Hu et al.,[60] where a very high fill factor of 95 % was used. The fill factor is a measure of the amount of solute and solvent (water) in the autoclave. In hydrothermal synthesis the pressure in the vessel is due to water vapour and evolution of gases. The water vapour which will affect the pressure in the autoclave as given by figure 2.25, section 2.4. For the same precursor concentration high fill factors will give rise to higher amounts of H_2S gas evolution, due to higher amounts of thiourea in the solution. The preliminary results combined with previous work therefore indicate that a high pressure due to high fill factors will give a more phase pure product. The microstructures were found to be of more uniform morphology and size when increasing the pressure, also an indication of phase purity. A more

uniform microstructure will be beneficial for making uniform thin films for solar cell applications. It was therefore decided to do further investigations of the effect of changed fill factor.

5.2 Unsubstituted $CuGaS_2$

The main goal of the parameter study of the unsubstituted $CuGaS_2$ was to find the synthesis parameters that maximize the phase purity of the product. The ideal phase purity for solar cell applications is 100%. A phase pure product will also facilitate substitution experiments. A qualitative analysis of secondary phases present was done by analysing the XRD data; a subjective analysis of the change in peak intensities. For a more accurate quantification, Rietveld analysis can be used. Rietveld refinements are based on calculating the minimum Rwp value, that is the difference between refinement and data. The calculation terminates when a minimum is reached, which does not necessarily correspond to the global minimum of the calculations.[85]

As seen in the result, figures 4.11(a) and 4.12(a), the Rietveld refinement had peak intensity problems with several of the diffraction peaks of $CuGaS_2$. This will give errors in the phase composition quantified since this is related to the intensities of the peaks. If the peak intensity misfit had been the same for all samples, the relative composition would be correct. However, this was not the case as there were variations in the peak intensity misfit. Unfortunately, phase purity quantification can not be done intensity independent. An awareness of these challenges is important when analysing the relative phase purities presented in figure 4.10, as the numbers presented have uncertainties.

Nevertheless, the results show some clear trends in the phase purity. Increasing the precursor concentration above 0.03M gives higher phase purity. This is in correlation with findings by Sortland[4] where higher concentration gave a more phase pure product, but not in correlation with the phase pure product obtained by Hu et al.[60] for 0.03M precursor concentration. The only difference between the findings is the fill factor. For a change from 42% to 60% to 73/80% fill factor there was no clear trend in the phase purity, a further increase to 95% was not possible due to safety concerns. This indicates that the pressures created by these relatively low fill factors are not high enough to affect the reactions occurring in the vessel. For these fill factors it appears that the pressure in the autoclave is mainly governed by the concentration, and the increased evolution of H_2S gas with increased concentration. Still, even for high concentrations of 0.30M, the phase purity remained in the mid-90 percent range. For a further increase in the phase purity it is suggested to investigate extreme pressures above

those tested here. The mechanisms behind high pressures giving high phase purity is not understood.

The microstructures found also indicate that the largest change occurs when increasing the concentration above 0.03M, and that fill factor in the range that was tested does not have a large effect on the system. The microstructures found at higher concentrations are more spherical and uniform than the particles of directional growth of 0.03M. Similar variations in the microstructures were found by Zhong et al.,[62] for 0.03M and water as a solvent. Hu et al.[60] found nanosized spheres for similar reaction parameters, but higher pressures. For thin film growth, a more uniform microstructure will enhance the growth of a uniform thin film, which is beneficial for solar cell applications. A concentration above 0.03M is therefore suggested as beneficial for the microstructure.

The Pawley method was used to quantify all other structural information since this gave a much better fit, as shown in figures 4.11(b) and 4.12(b). For all plots of phase purity, unit cell volumes or lattice parameters based on Rietveld and Pawley calculations, error bars are included in the figures, but these are too small to be seen. The calculated errors are statistical and not actual errors. The actual errors will be larger, since the samples are not phase pure, and secondary phases will affect all calculations, due to peak overlap between $CuGaS_2$ and secondary phases.

The trend in the calculated unit cell volumes given in figure 4.13 can be correlated to the phase purity of the products. The 0.03M concentration does not have a linear phase purity increase with increasing fill factor, the non-linearity is also seen in the calculated unit cell volumes. The 0.15M concentration have a linear increase in the purity with increasing fill factor and a linear trend in the unit cell volumes is seen. The 0.30M samples have little difference both in the phase purity and in the unit cell volume. This indicates that the calculated change in the unit cell is in fact an effect of influence of the secondary phases on the calculations, more than an actual change in the unit cell. If the unit cell of $CuGaS_2$ was changed, it would give a shift of the $CuGaS_2$ peaks in the diffractograms, which is not seen for these samples. It should be noted that sample preparation affects the shifts in a diffractogram. Based on these findings, it is suggested that fine-tuned calculations on lattice parameters are very affected by the presence of secondary phases, and should be done on phase pure products.

The reactions suggested for the formation of $CuGaS_2$ under hydrothermal conditions in section 2.4, propses a 1:1 stoichiometric relation of the sulfur precursor thiourea and the evolution of H_2S gas. This would give a pressure contribution of H_2S gas one order of magnitude lower than that of the water vapour, which would make it close to neglishible for the overall pressure. It is

suggested that this simple reaction is insufficient as a description of the system. This is based on the experimental findings that the pressure in the autoclave was highly dependant on the precursor concentration, meaning that the gases evolved in the reactions were not of neglishible amounts. This indicates that there has either been an underestimation of the H_2S gas contribution, or that other gases are evolved during the reaction, or a combination of these.

To understand the reaction mechanisms in the system better, the gases produced in the synthesis could have been collected and analysed. Investigations of the possible reaction mechanisms of the unsubstituted systems is not a part of the goals of this thesis and no further studies on the gas evolution was made. It is however suggested that a more thorough understanding of hydrothermal synthesis of the unsubstituted $CuGaS_2$ system should be obtained, as there are many factors that may affect the synthesis. A thorough understanding of the unsubstituted system will also be beneficial for the understanding of the iron substituted system, which may be used for intermediate band applications.

5.3 CGFS: Substitution site

The main goal of this thesis is to make iron substituted $CuGaS_2$ via hydrothermal synthesis. The microstructure of the product should be uniform, to facilitate thin film growth for solar cell applications. The product should have an intermediate band in the band gap, making it an intermediate band semiconductor. To obtain this, a sufficient amount of iron should be substituted into the lattice, enabling the creation of a continous intermediate band. It was chosen to aim for a 10 % iron substitution into the lattice, based on the amount used by Lucena et al.[27] to obtain an intermediate band by V substitution in a In_2S_3 lattice. The systems are not similar, but the amount was used as a guideline for a test- of- concept. 10 % substitution is an order of magnitude larger than what is necessary for intermediate band formation, but will suffice as a guide for whether iron substitution is possible using hydrothermal synthesis.

Iron substitution to both cation sites was attempted, as it is not clear which site is more favourable, as discussed in section 2.3.6. Both substitution sites gave a colour change in the obtained product compared to the unsubstituted equivalent. The colour change was from red/brown to grey/black. This colour change has been observed in literature, and was assigned to iron substitution into the lattice.[49,70] If an intermediate band is formed in the band gap of $CuGaS_2$, it will induce additional absorption transition, as may be seen as colour change in the product. For the obtained product however, the colour change alone may not be directly attributed to iron substitution, as the product contained

an additional FeS_2 secondary phase that was not present in the unsubstituted samples.

For a more accurate description of the absorption properties reflectance spectroscopy was attempted. Any change in the band structure due to intermediate band formation should give a change in the absorption properties of the iron containing samples compared to the unsubstituted sample. As shown in figure 4.32, there was a very high signal noise and little information could be extracted from the absorption measurements. Any trends in the absorption seen from the spectra are the same for all samples, also those not containing iron. Other investigations are needed to determine whether iron is changing the band structure.

The phase composition of the products may be an indication of whether iron substitution was achieved or not. A high substitution of iron into the $CuGaS_2$ lattice would give a low iron content in the secondary phases, in addition to Ga-rich or Cu-rich secondary phases, for Fe_{Ga} or Fe_{Cu} respectively. A quantitative mass balance would be best to analyse this. This requires a Rietveld refinement of low peak intensity mismatch, giving precise phase quantifications. This was, unfortunately, not the case for these products.

The diffractograms were therefore used to give a qualitative estimation of the mass balance of the systems. It was found that the Fe_{Ga} samples contained both Ga-rich and Cu-rich secondary phases, in addition to low amounts of iron-rich secondary phase. The Fe_{Cu} samples contained mainly Fe-rich secondary phases, leaving less iron available for substitution than for the Fe_{Ga} samples. This indicates that if there has been any iron substitution, it has occurred in the Fe_{Ga} samples. This is in accordance with the literature proposing Ga-site as the best suited for iron substitution, based on similar ionic radii and oxidation states.

On the other hand, the shape of the peaks in the diffractograms (figures 4.21 and 4.22) indicates iron substitution to Cu-site. An iron substitution into the $CuGaS_2$ lattice would mean substituting a large cation with a smaller one, giving a decrease in the unit cell. This would give a diffraction peak shift to higher Bragg angles.[68] A substitution could also induce a relative shift in the a and c lattice parameter compared to the unsubstituted sample. A change in either a or c parameter could cause a peak split, if the peak is an overlap of different hkl planes. It is seen that there is a difference in position of the main peak at 2θ angle at 29.2 and the peak shape at 2θ angles 48.5 and 57.5, when comparing the Fe_{Ga} and Fe_{Cu}, see figure 4.23.

A peak split is seen for the Fe_{Ga} samples, but the peak is very similar to that of the unsubstituted samples. Both Fe_{Ga} and unsubstituted samples

contain CuS, which also has diffraction lines in the same area as the $CuGaS_2$ peak split. The peak split may be an effect of a change in the unit cell, but most likely it is just an effect of a lower CuS content, lowering the overlap with these diffraction lines, causing the peak to split with decreasing CuS content. The similarity to the unsubstituted peaks gives reason to believe that the peak split is not caused by iron substitution.

A peak shift to higher Bragg angles is seen for the Fe_{Cu} samples, indicating a decrease in the unit cell compared to the unsubstituted samples. These samples do not contain detectable amounts of CuS, which therefore will not interfere with the shape of the peaks. The difference of the peak shapes of the iron containing and the unsubstituted sample indicates that there is indeed a difference in the unit cell. Marsen et al.[68] has made iron subsituted to Ga-site, and found a peak shift for increasing amount of iron in the lattice. The size of the peak shift in figure 4.23 corresponds to that found by Marsen et al.[68] for 8% iron in the lattice, that is $CuGa_{1-x}Fe_xS_2$ with x=0.08, see figure 2.28. Marsen et al. later investigated the optical properties of the system[28] and found that for a substitution amount of x=0.015 and 0.08, there was a sub-band gap absorption, see figure 2.20. The group suggests that this absorption may be due to the formation of an intermediate band.

The literature comparison indicates that there may be iron substitution into the $CuGaS_2$ lattice, for the Fe_{Cu} samples of 0.30M precursor concentration. The size of the shift corresponded to an amount of iron that Marsen et al.[28] found sufficient to induce sub-band gap absorption. A sub-band gap absorption may be due to the formation of an intermediate band in the band gap. Optical measurements were attempted, but as described above, the results were inconclusive, due to high signal to noise ratio.

Pawley refinements were made to investigate whether or not iron substitution could be detected as a change in the lattice parameters. As described in section 2.3.6, figure 2.23 the lattice parameters were found to vary along the solid solution line between $CuGaS_2$ and $CuFeS_2$. Digiuseppe et al.[73] found that the a parameter decreased and the c parameter increased with increasing iron content. This is the opposite of what was found in the presented results, where the a parameter on average was larger, and the c parameter was in the same range as the unsubstituted. This does not necessarily contradict possible substitution, as it was found by Schneider et al.[49] and Teranish et al.[65] that the lattice parameters do not change considerably for low substitution levels. The question could be posed though, if such low substitution levels are sufficient for the formation of a continuous intermediate band.

The effect of iron substitution on the $CuGaS_2$ unit cell volume is unclear,

since the bonds in the structure are partially ionic and partially covalent. The unit cell volumes of the substituted samples were found to be on average larger than the unsubstituted. There was no clear difference found between the different substitution sites.

The microstructures found were similar to the unsubstituted samples. For low substitution amounts this is not unexpected, as the microstructures may remain unchanged for small unit cell changes, since the microstructures are agglomerates of smaller crystals. It was decided to make a closer investigation of the elemental composition of the microstructures using EDS mapping. The hope was to find a distinct difference in iron content of the different $CuGaS_2$ structures. The elemental composition analysis using EDS showed some iron content in most $CuGaS_2$ particles. A trend in the iron content for different morphologies of $CuGaS_2$ was not found. The amount of iron was in the range of a few atomic percent. This is the target substitution amount, but unfortunately also within the uncertainty limit of the EDS mapping due to matrix effects, described in section 2.6.2. Low energies were used for the mappings to minimize the influence of underlying and surrounding particles, but the elemental quantification will still entail a certain error.

The mapping of the secondary phases show particles of distinct growth directions, or large sizes. Both are unfortunate for the growth of uniform thin films. A phase pure CGFS should therefore be obtained before attempting to grow the structure into a thin film. This could be done by a further parameter study of the hydrothermal synthesis.

A phase pure product should also be obtained to enable structural refinements. A fine-tuned Rietveld analysis of the substitution sites could possibly be done if a phase pure product was obtained. As the phase diagram of the system in figure 2.22 shows, the system is thermodynamically stable as a one-phase system of iron substituted $CuGaS_2$. Smaili and Kanzari[90] annealed a $CuGaS_2$ thin film with impurities in inert atmosphere and obtained a phase pure $CuGaS_2$ film. Heat treatment of the product was therefore attempted with the aim of obtaining a single phase powder. The heat treatment led to oxidation of the powder, even with N_2 flushing and very low oxygen partial pressures. A phase pure product of $CuGaS_2$ was therefore not obtained, and a refinement on the lattice positions was not possible.

5.4 CGFS: Temperature and time

The many secondary phases found in the products imply that the systems are not in thermodynamic equilibrium. Gibbs phase law[91] dictates that for thermo-

dynamic equilibrium there may be a maximum of three phases present in this four component system (Cu, Ga, S and Fe). As several of the products contain the $CuGaS_2$ phase combined with up to three secondary phases, Gibbs phase law is broken and kinetic considerations should also be made. Some phases may be formed before a thermodynamic equilibrium is set, other phases may be formed due to gradients of concentration, temperature, pH etc. in the reaction mixture. The hydrothermal system is complex, and an investigation of the effect of varying reaction time and temperature was made with the aim of obtaining a better understanding of the reaction mechanisms.

All samples of this study had the same precursor concentrations, composition and fill factor, giving the same theoretical mass of all products. The fact that there was a large variation of the obtained product masses indicate that a reaction equilibrium has not been obtained, especially for the shortest reaction times.

As shown in figures 4.37 and 4.38, it was found that the GaO(OH) phase was the only phase formed for 1h reaction time and 160 °C reaction temperature, indicating a lower activation barrier for the formation of this phase compared to $CuGaS_2$, CuS and FeS_2. When increasing the temperature for the same short reaction time of 1 hour, other phases ($CuGaS_2$, CuS and FeS_2) were formed, indicating enhanced reaction kinetics with increased temperature, as expected.

From figure 4.37 it appears that the CuS phase is formed for intermediate reaction temperatures and times, and a further increase causes a decrease in the amount of the phase. This occurs simultaneously as a decrease in the GaO(OH) phase, see figure 4.37(a) , and an increase of the $CuGaS_2$ phase. This gives reason to believe that the $CuGaS_2$ phase is formed at the expense of the precipitated CuS and GaO(OH) phases, in a continuous precipitation reaction between the precipitated species and the solute. Increased reaction time will give the reaction sufficient time to approach equilibrium, while increased reaction temperature will enhance the reaction kinetics.

The FeS_2 phase is formed mainly at high temperatures, but the SEM/EDS analysis showed that it is formed at most reaction temperatures, but in amounts lower than that detectable by XRD. The high temperatures needed indicate that there is a large activation barrier for the formation of the phase. For lower temperatures, the iron may remain in the solution and be washed out, or it may be included in the $CuGaS_2$ lattice.

The reaction parameters that give the highest purity of $CuGaS_2$ is 30 hour reaction time and a temperature of 200- 250 °C. There was little difference in the purity when increasing the reaction temperature above 200 °C, which is in accordance with the results of the parameter study by Zhong et al.[62] The group

proposes no change in the $CuGaS_2$ compound for a temperature increase above 200 °C. Lattice parameters are not presented for the temperature range, so it is not known whether the group means that there was no change in the phase purity of the sample, or no change in the $CuGaS_2$ lattice parameters.

As the diffractograms in figures 4.35 and 4.36 show, there was a difference between 200- 250 °C in these samples, the difference being mainly in the $CuGaS_2$ crystalline size, not in the phase purity. The diffractograms show a narrowing of the main peak of $CuGaS_2$ for increased reaction temperature from 160 to 250 °C as well as for increased reaction time from 1 to 30 hours. A narrowing of the diffraction peaks indicates a larger average crystallite size. The Pawley crystallite sizes calculated (figure 4.39) indicate that the narrowing of the peak is indeed due to an increased crystallite size. The growth in crystallite size may either be due to consumption of precursors, or due to Ostwald ripening when an equilibrium between precipitate and precursors is obtained. Ostwald ripening is growth of large crystallites at the expense of smaller ones.

It is seen from the diffractograms that the crystallite size is affected by both reaction time and temperature. Higher reaction temperature gives a higher supersaturation of the solution, leading to a shorter nucleation time and separation of nucleation and growth period. A narrow size distribution of the particles is thus obtained with high temperatures. A low reaction temperature gives lower supersaturation levels and longer nucleation time. This will make the the nucleation and growth process occur simultaneously, making the size distribution large. This is seen as a broad diffraction peak in the diffractograms for low reaction temperatures. The peak narrowing with increasing temperature, indicates that despite having a narrower crystallite size distribution, the average crystallite size is larger for higher temperatures. For a given temperature, it is seen that an increase in reaction time gives larger crystallites in most cases. The reaction time will affect the crystallite size, as the reaction time is correlated to the growth time. It is difficult to determine exactly which growth process is occurring for the different reaction times, as the kinetics of the system is not well-known.

The crystallite size found by Hu et al.[60] was 25 nm, for reaction time 4 hours and temperature of 160 °C. Their products were phase pure and the Scherrer equation based on the width of the diffraction peaks was used to estimate the crystallite sizes. The calculation method differs from the Pawley refinements used here, where a 5 nm crystallite size was found. It should be noted that there are large uncertainties in this calculation, as a reaction time of 4 hours and temperature of 160 °C did not give a phase pure product, and the calculations are affected by secondary phases present. It is suggested that the crystallite

sizes found here are in the same range as that found in literature, but a further comparison is not possible due to the large differences in the samples.

6 Concluding remarks

The parameter study of hydrothermal synthesis of $CuGaS_2$ indicates that it is difficult to make a 100% phase pure product with this method. The highest purities (around 95 at%) were obtained with reaction temperatures of 200-250 °C, 30 hour reaction time and medium to high precursor concentration, that is [Cu]:[Ga]:[S]= 0.15M:0.15M:0.60M or higher. Increasing the sulfur excess to five times excess may give an increase in the phase purity. The fill factor of the autoclave was found to have little effect on the phase purity of the product, which indicates that the fill factors tested are too low to have a large effect on the overall pressures. Further studies on higher fill factors are needed.

Iron substitution into the $CuGaS_2$ lattice was attempted by varying the stoichiometric relation of the precursors. High amounts of secondary phases made fine-tuned refinements on lattice positions difficult. Lattice parameters and unit cell volumes were calculated, but due to the nature of the bonds in the lattice it was difficult to extract any conclusions from the unit cell volumes. The main conclusion drawn from the microstructure analysis is that there might be iron in the $CuGaS_2$ samples, but that the amounts are too low to quantify accurately by EDS analysis.

The position and shape of the diffraction peaks indicate that if iron is substituted into the lattice, it has been substituted to Cu-site. The size of the shift corresponds to the shift found by another group, where the CGFS had a substitution level high enough to create sub-band gap absorptions that were linked to the possible formation of an intermediate band. Although the diffraction data is promising, it is not possible based on these data to conclude whether it is possible to substitute iron into the $CuGaS_2$ lattice by hydrothermal synthesis or not.

Suggestions to the reaction kinetics related to the formation of secondary phases are made. It is suggested that a Ga-rich secondary phase is precipitated first, and for an increase in reaction time or temperature, a Cu-rich secondary phase is formed simultaneously with $CuGaS_2$. A further increase in reaction time or temperature gives a consumption of the secondary phases in favour of the precipitation of $CuGaS_2$. Based on how the reaction parameters affected the crystallite sizes of $CuGaS_2$, a nucleation and growth process is suggested. Further studies are needed to obtain a greater understanding of the reaction mechanisms occurring in the system.

The products made in this work were all powders. To enable integrating the compound into a solar cell device, thin film growth of $CuGaS_2$, both unsubstituted and iron substituted should be investigated. Grain sizes should be

considered when growing a thin film, as grain boundaries represent recombination centres. The large and uniform crystallites of 250 °C may be beneficial for thin film applications, compared to the smaller particles of larger size distribution made by 200 °C reaction temperature. Both temperatures are suggested above, based on equal phase purities as this will be the most important for the making of a thin film for solar cell applications.

References

(1) Luque, A.; Hegedus, S., *Handbook of photovoltaic science and engineering*; Wiley: Chichester, 2003.

(2) In, Arvizu, D.; Balaya, P.; Cabeza, L. F.; Hollands, K. G. T.; Jager-Waldau, A.; Kondo, M.; Konseibo, C.; Meleshko, V.; Stein, W.; Tamaura, Y.; Xu, H.; Zilles, R. *Direct Solar Energy: IPCC Special Report on Renewable Energy Sources and Climate Change Mitigation* Ed: Edenhofer, O., Cambridge University Press, Cambridge, United Kingdom and New York, NY, USA, 2011.

(3) 2013 Renewable Energy Progress Report, COM (13) 175, final.

(4) Sortland, Ø., *Wet chemical synthesis of materials for intermediate band solar cells*, Master Thesis, Department of materials chemistry, Norwegian University of Science and Technology, Trondheim, 2011.

(5) Green, M. A., *Power to the people : sunlight to electricity using solar cells*; University of New South Wales Press: Sydney, 2000.

(6) Ende, B. M. van der; Aarts, L.; Meijerink, A. *Advanced Materials* **2009**, *21*, 3073.

(7) Branch, M. S.; Berndt, P. R.; Botha, J. R.; Leitch, A. W. R.; Weber, J. *Thin Solid Films* **2003**, *431-432*, 94–98.

(8) Renewable Energy Corporation ASA; *REC ASA has decided to cease further funding of REC Wafer Norway AS*, Initial public offering (IPO), 14/8, 08:01; 2012.

(9) Chowdhury, S.; Ichimura, M. *Mater. Sci. Semicond. Process.* **2011**, *13*, 252–256.

(10) Luque, A.; Marti, A. *Advanced Materials* **2010**, *22*, 160–174.

(11) Hanna, M. C.; Nozik, A. J. *Journal of Applied Physics* **2006**, *100*, 074510–8.

(12) Luque, A.; Marti, A.; Stanley, C. *Nature Photonics* **2012**, *6*, 146–152.

(13) SUNLAB laboratory (2007) *High-efficiency multi-junction solar cells: Current status and future potential* (Yastrebova, N. V.) Centre for Research in Photonics, University of Ottawa.

(14) Boltzmann, L., *Lectures on gas theory*; University of California Press: Berkeley, 1964.

(15) Repins, I.; Contreras, M. A.; Egaas, B.; DeHart, C.; Scharf, J.; Perkins, C. L.; To, B.; Noufi, R. *Progress in Photovoltaics* **2008**, *16*, 235–239.

(16) Marti, A.; Marron, D. F.; Luque, A. *J. Appl. Phys.* **2008**, *103*, 073706/1–6.

(17) Fonash, S. J., *Solar cell device physics*, 2nd ed.; Elsevier: Amsterdam, 2010.

(18) Strandberg, R.; Reenaas, T. W. *Ieee Transactions on Electron Devices* **2011**, *58*, 2559–2565.

(19) Shockley, W.; Queisser, H. J. *Journal of Applied Physics* **1961**, *32*, 510–519.

(20) Jackson, P.; Hariskos, D.; Lotter, E.; Paetel, S.; Wuerz, R.; Menner, R.; Wischmann, W.; Powalla, M. *Progress in Photovoltaics* **2011**, *19*, 894–897.

(21) Green, M. A., *Third generation photovoltaics : advanced solar energy conversion*; Springer: Berlin, 2003.

(22) Semonin, O. E.; Luther, J. M.; Choi, S.; Chen, H.-Y.; Gao, J.; Nozik, A. J.; Beard, M. C. *Science* **2011**, *334*, 1530–1533.

(23) Moon, A.; James, L. W.; Vander Plas, H. A.; Yep, T. O.; Antypas, G. A.; Chai, Y. In *13 th IEEE Photovoltaic Specialists Conference*, pp 859–867.

(24) Luque, A.; Marti, A. *Physical Review Letters* **1997**, *78*, 5014–5017.

(25) Luque, A.; Marti, A. *Progress in Photovoltaics* **2001**, *9*, 73–86.

(26) Wahnón, P.; Tablero, C. *Physical Review B* **2002**, *65*, 165115.

(27) Lucena, R.; Aguilera, I.; Palacios, P.; Wahnon, P.; Conesa, J. C. *Chem. Mater.* **2008**, *20*, 5125–5127.

(28) Marsen, B.; Klemz, S.; Unold, T.; Schock, H. W. *Progress in Photovoltaics* **2012**, *20*, 625–629.

(29) Palacios, P.; Sanchez, K.; Conesa, J. C.; Fernandez, J. J.; Wahnon, P. *Thin Solid Films* **2007**, *515*, 6280–6284.

(30) Luque, A.; Marti, A. *Nature Photonics* **2011**, *5*, 137–138.

(31) Linares, P. G.; Marti, A.; Antolin, E.; Luque, A. *J. Appl. Phys.* **2011**, *109*, 014313/1–8.

(32) SUNLAB laboratory; http://sunlab.site.uottawa.ca/research.php, Retrieved April 24, 2013, 14:21.

(33) Tablero, C.; Fuertes, M. D. *J. Phys. Chem. C* **2010**, *114*, 2756–2763.

(34) Lin, C.-C.; Liu, W.-L.; Shih, C.-Y. *Optics Express* **2011**, *19*, 16927–16933.

(35) Fuertes, M. D.; Canovas, E.; Levy, M. Y.; Marti, A.; Luque, A.; Afshar, M.; Albert, J.; Lehmann, S.; Abou-Ras, D.; Sadewasser, S.; Barreau, N. *Sol. Energy Mater. Sol. Cells* **2010**, *94*, 1912–1918.

(36) Marron, D. F.; Marti, A.; Luque, A. *Physica Status Solidi a-Applications and Materials Science* **2009**, *206*, 1021–1025.

(37) Luque, A.; Marti, A.; Antolin, E.; Tablero, C. *Physica B-Condensed Matter* **2006**, *382*, 320–327.

(38) Luque, A.; Marti, A. *Ieee Transactions on Electron Devices* **2010**, *57*, 1201–1207.

(39) Metzner, H.; Hahn, T.; Cieslak, J.; Grossner, U.; Reislohner, U.; Witthuhn, W.; Goldhahn, R.; Eberhardt, J.; Gobsch, G.; Krausslich, J. *Applied Physics Letters* **2002**, *81*, 156–158.

(40) Aguilera, I.; Palacios, P.; Wahnon, P. *Solar Energy Materials and Solar Cells* **2010**, *94*, 1903–1906.

(41) Hahn, H.; Frank, G.; Klingler, W.; Meyer, A.-D.; Störger, G. *Zeitschrift für anorganische und allgemeine Chemie* **1953**, *271*, 153–170.

(42) Cieslak, J.; Hahn, T.; Metzner, H.; Eberhardt, J.; Witthuhn, W.; Krausslich, J.; Wunderlich, F. *Phys. Rev. B: Condens. Matter Mater. Phys.* **2007**, *75*, 245306/1–245306/9.

(43) Oishi, K.; Kobayashi, S.; Kaneko, F. *J. Cryst. Growth* **1995**, *153*, 158–63.

(44) Aguilera, I.; Vidal, J.; Wahnon, P.; Reining, L.; Botti, S. *Physical Review B* **2011**, *84*, Article no. 085145.

(45) Hahn, T.; Metzner, H.; Reislohner, U.; Cieslak, J.; Eberhardt, J.; Muller, M.; Witthuhn, W. *Thin Solid Films* **2005**, *480*, 332–335.

(46) Scheer, R. *Trends Vac. Sci. Technol.* **1997**, *2*, 77–112.

(47) Heske, C.; Richter, G.; Chen, Z.; Fink, R.; Umbach, E.; Riedl, W.; Karg, F. *J. Appl. Phys.* **1997**, *82*, 2411–2420.

(48) Kokta, M.; Carruthers, J. R.; Grasso, M.; Kasper, H. M.; Tell, B. *Journal of Electronic Materials* **1976**, *5*, 69–89.

(49) Schneider, J.; Räuber, A.; Brandt, G. *Journal of Physics and Chemistry of Solids* **1973**, *34*, 443–450.

(50) Bailey, C. L.; Liborio, L.; Mallia, G.; Tomic, S.; Harrison, N. M. *Physical Review B* **2010**, *81*.

(51) Tell, B.; Shay, J. L.; Kasper, H. M. *Physical Review B* **1971**, *4*, 2463.

(52) Abrahams, S. C.; Bernstei, J. L. *Journal of Chemical Physics* **1973**, *59*, 5415–5422.

(53) Spiess, H. W.; Haeberle, U.; Brandt, G.; Rauber, A.; Schneide, J. *Physica Status Solidi B-Basic Research* **1974**, *62*, 183–192.

(54) Atkins, P. W.; Shriver, D. F., *Shriver & Atkins' inorganic chemistry*, 5th ed.; Oxford University Press: Oxford, 2010.

(55) Palacios, P.; Sanchez, K.; Conesa, J. C.; Wahnon, P. *Phys. Status Solidi A* **2006**, *203*, 1395–1401.

(56) Shay, J. L.; Schiavon, L. M.; Tell, B.; Kasper, H. M. *Physical Review B* **1972**, *5*, 5003.

(57) Horinaka, H.; Yamamoto, N.; Miyauchi, T. *Japanese Journal of Applied Physics* **1978**, *17*, 521–526.

(58) Romero, A. H.; Cardona, M.; Kremer, R. K.; Lauck, R.; Siegle, G.; Hoch, C.; Munoz, A.; Schindler, A. *Physical Review B* **2011**, *83*, 195208/1–9.

(59) Metzner, H.; Eberhardt, J.; Cieslak, J.; Hahn, T.; Goldhahn, R.; Reislohner, U.; Witthuhn, W. *Thin Solid Films* **2004**, *451*, 241–244.

(60) Hu, J. Q.; Deng, B.; Wang, C. R.; Tang, K. B.; Qian, Y. T. *Solid State Communications* **2002**, *121*, 493–496.

(61) Hamakawa, Y., *Thin-film solar cells: next generation photovoltaics and its applications*; Springer: Berlin, 2004.

(62) Zhong, J. S.; Zhao, Y. S.; Yang, H. L.; Wang, J.; Liang, X. J.; Xiang, W. D. *Applied Surface Science* **2011**, *257*, 10188–10194.

(63) Ueno, T.; Nagasaki, K.; Horikawa, T.; Kawakami, M.; Kondo, K. *Canadian Mineralogist* **2005**, *43*, 1653–1661.

(64) Julien, C.; Barnier, S. *Materials Science and Engineering B-Solid State Materials for Advanced Technology* **2001**, *86*, 152–156.

(65) Teranish, T.; Sato, K.; Kondo, K. *Journal of the Physical Society of Japan* **1974**, *36*, 1618–1624.

(66) Marron, D. F.; Marti, A.; Luque, A. *Thin Solid Films* **2009**, *517*, 2452–2454.

(67) Palacios, P.; Sanchez, K.; Wahnon, P.; Conesa, J. C. *Journal of Solar Energy Engineering-Transactions of the Asme* **2007**, *129*, 314–318.

(68) Marsen, B.; Klemz, S.; Landi, G.; Steinkopf, L.; Scheer, R.; Schorr, S.; Schock, H. W. *Thin Solid Films* **2011**, *519*, 7284–7287.

(69) Brandt, G.; Rauber, A.; Schneide, J. *Solid State Communications* **1973**, *12*, 481–483.

(70) Bardeleben, H. J. von; Goltzene, A.; Meyer, B.; Schwab, C. *Phys. Status Solidi A* **1978**, *48*, K145.

(71) Tanaka, K.; Ishii, K.; Matsuda, S.; Hasegawa, Y.; Sato, K. *Japanese Journal of Applied Physics Part 1-Regular Papers Short Notes & Review Papers* **1989**, *28*, 12–15.

(72) Lamarche, A. M.; Woolley, J. C.; Quintero, M.; Ruiz, J. *Physica Status Solidi a-Applied Research* **1991**, *126*, K109–K113.

(73) Digiuseppe, M.; Steger, J.; Wold, A.; Kostiner, E. *Inorganic Chemistry* **1974**, *13*, 1828–1831.

(74) Cushing, B. L.; Kolesnichenko, V. L.; O'Connor, C. J. *Chemical Reviews* **2004**, *104*, 3893–3946.

(75) Walton, R. I. *Chemical Society Reviews* **2002**, *31*, 230–238.

(76) Parr Instrument Company, Non- stirred Pressure Vessels: www.parrinst.com, Retrieved april 23, 2013, 14:00.

(77) Li, B.; Xie, Y.; Huang, J. X.; Qian, Y. T. *Advanced Materials* **1999**, *11*, 1456–1459.

(78) Tompsett, G. A.; Conner, W. C.; Yngvesson, K. S. *Chemphyschem* **2006**, *7*, 296–319.

(79) Zhao, Y. Y.; Frost, R. L.; Yang, J.; Martens, W. N. *Journal of Physical Chemistry C* **2008**, *112*, 3568–3579.

(80) Feng, J. M.; Han, J. J.; Zhao, X. J. *Progress in Organic Coatings* **2009**, *64*, 268–273.

(81) Lu, Q. Y.; Hu, J. Q.; Tang, K. B.; Qian, Y. T.; Zhou, G. E.; Liu, X. M. *Inorganic Chemistry* **2000**, *39*, 1606–1607.

(82) West, A. R., *Basic solid state chemistry*, 2nd ed.; Wiley: Chichester, 1999.

(83) West, A. R., *Solid state chemistry and its applications*, 1st ed.; Wiley: Chichester, 1984.

(84) Pawley, G. S. *Journal of Applied Crystallography* **1981**, *14*, 357–361.

(85) Young, R. A., *The Rietveld method*; Oxford University Press CY: Chester, England, 1993.

(86) Egerton, R. F., *Physical Principles of Electron Microscopy: An Introduction to TEM, SEM, and AEM*; Springer Science Business Media, Inc.: Boston, MA, 2005.

(87) Hapke, B., *Theory of Reflectance and Emittance Spectroscopy*, 2nd ed.; Cambridge University Press: Cambridge, 2012.

(88) Kubelka, P. von; Munk, F. *Z. Tech. Phys* **1931**, *12*, 593–601.

(89) Weckhuysen, B. M.; Schoonheydt, R. A. *Catalysis Today* **1999**, *49*, 441–451.

(90) Smaili, F.; Kanzari, M. *Mater. Sci. Eng., C* **2009**, *29*, 1969–1973.

(91) Helbæk, M.; Kjelstrup, S., *Fysikalsk kjemi*, 2. ed.; Fagbokforl.: Bergen, 2006.

(92) Gotsis, H. J.; Barnes, A. C.; Strange, P. *Journal of Physics-Condensed Matter* **1992**, *4*, 10461–10468.

(93) Li, S. J.; Zheng, C.; Lobring, K. C. *Zeitschrift Fur Kristallographie-New Crystal Structures* **2003**, *218*, 11–12.

(94) Brostigen, G.; Kjekshus, A. *Acta Chemica Scandinavica* **1969**, *23*, 2186.

(95) Antropov, V. M.; Pleshchev, V. G.; Garafutdinova, E. N. *Inorganic Materials* **1991**, *27*, 1289–1290.

(96) Johansson, G. *Arkiv for Kemi* **1963**, *20*, 343.

(97) Krämer, V.; Nitsche, R.; Ottemann, J. *Journal of Crystal Growth* **1970**, *7*, 285–289.

(98) Iskhakova, L. D.; Trunov, V. K.; Shchegoleva, T. M.; Ilyukhin, V. V.; Vedernikov, A. A. *Kristallografiya* **1983**, *28*, 651–657.

Appendices

A XRD: phase and refinement information

The phases identified by the EVA software and used in Rietveld and Pawley analysis are given in table A.1. The information is taken from the database PDF-4+2012, software version 4.12.0.4, database version 4.1203, the database number of each phase is given. Only the lattice parameters needed for the given crystal system are presented.

The refinement parameters used in TOPAS calculations are presented in table A.2. Since the $CuGaS_2$ phase was analysied using both Rietveld and Pawley analysis, table A.3 gives details of the refinements. The remaining structures were all refined using Rietveld analysis, details are given in table A.4. The lattice information of the structures is given in table A.1 and is not repeated here.

Table A.1: Structural information of the phases used.

Structure	Crystal system	Space group	Lattice parameters (Å)			Database nr.	Ref.
			a	c	misc.		
$CuGaS_2$	Tetragonal	I-42d	5.351	10.48		04-005-8830	69
CuS	Hexagonal	P63/mmc	3.788	16.33		04-007-1392	92
GaO(OH)	Orthorombic	Pnma	9.791	4.517	b= 2.973	04-010-9861	93
FeS_2	Cubic	Pa-3	5.418			04-003-1989	94
$CuFeS_2$	Tetragonal	I-42d	5.28	10.37		04-002-0241	95
$3\,Ga_2O_3{*}4\,SO_3{*}9\,H_2O$	Rhombohedral	R-3m	7.178	17.17		04-014-1482	96
Ga_2S_3	Monoclinic	Cc	11.04	7.02	b= 6.42 β= 121.2^o	04-003-3839	97
$CuSO_4{*}5\,H_2O$	Anorthic	P-1	6.116	5.961	b= 10.716 α= 82.36^o β= 107.31^o γ= 102.61^o	04-009-4278	98

Table A.2: Refinement parameters used in TOPAS

Emission Profile	Background	Instrument	Corrections	Miscellaneous
WL(Å)= 1.534753	Order= 10*	Prim. radius (nm)= 200.5	Sample displ.(mm): refine	Conv. steps= 1
WL(Å)= 1.540596		Sec. radius (nm)= 200.5	LP factor: fix	
WL(Å)= 1.541058		Linear PSD		
		2Th angular range of LPSD (^{o})= 4		
		FDS angle (^{o}) = 0.1		
		FDS angle (^{o}) = 0.1		

* This relatively high order is set due to the shape of the diffractograms.

Table A.3: Refinement parameters used in TOPAS; for the $CuGaS_2$ structure

Method / Ref.param	Rietveld (Add structure)	Pawley (Add hkl phase)
Space group from table A.1	Inserted	Inserted
Lattice parameters from table A.1	Refine	Refine
Scale	Refine	-
L Vol-IB (nm)	On	Off
L Vol-FWHM (nm)	On	Off
Cry size L (nm)	-	Refine
Strain L	Refine	-
Strain G	Refine	-
Cu^{+} site (x,y,z)	0, 0, 0	Not added
Ga^{3+} site (x,y,z)	0, 0, 0.5	Not added
S site (x,y,z)	0.272, 0.25, 0.125	Not added
Preferred orientation	Off	-

Table A.4: Refinement parameters used in TOPAS; Rietveld analysis of the remaining structures.

Struc. / Ref.param	$CuFeS_2$	CuS	GaO(OH)	FeS_2	Ga_2S_3	$CuSO_4$ *5 H_2O	3 Ga_2O_3 *4 SO_3 *9 H_2O
Space group from table A.1	Inserted	Inserted	Inserted	Inserted	Inserted	Inserted	Inserted
Lattice param. from table A.1	Refine	Refine	Refine	Refine	Refine	Refine	Refine
Scale	Refine	Refine	Refine	Refine	Refine	Refine	Refine
L Vol-IB (nm)	On	On	On	On	On	On	On
L Vol-FWHM (nm)	On	On	On	On	On	On	On
Cry size L (nm)	Refine	Refine	Refine	Refine	Refine	Refine	Refine
Misc.		Cry size min= 15 nm*					

* Necessary due to the high overlap of $CuGaS_2$peaks .

B SEM/EDS analysis: $CuGaS_2$ structures

There are a large range of microstructures of $CuGaS_2$, a selection is presented here. The pie chart gives atomic percent quantification based on the EDS measurements. The colours of the pie charts corresponds to that of the EDS mappings. Spheres with inner and outer shell is given in figure B.1, broken spheres in figure B.2 and irregular sphere-like structures in figure B.3.

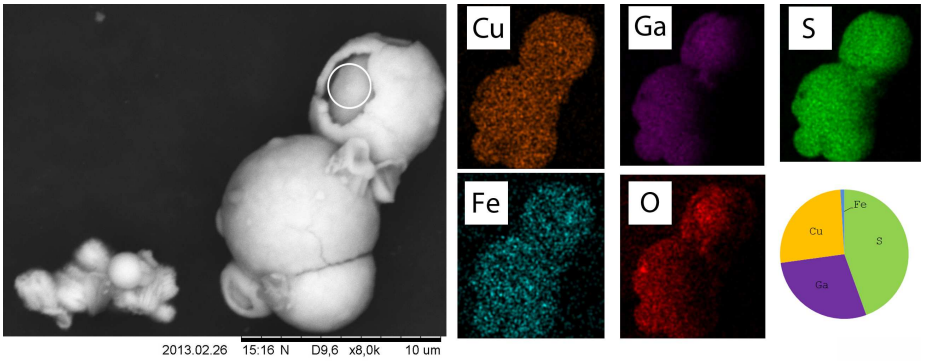

Figure B.1: Microstructures of $CuGaS_2$. The elemental composition of the inner sphere and the outer shell was approximately the same. The image is taken from sample $C_{0.9}GF_{0.1}S42$-0.15.

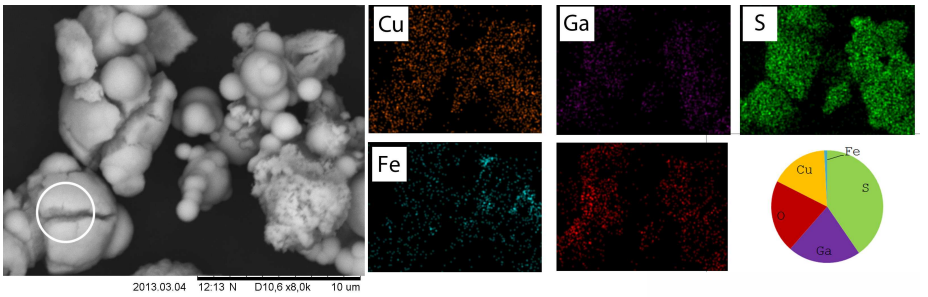

Figure B.2: Whole and broken $CuGaS_2$ spheres. The image is taken from sample $C_{0.9}GF_{0.1}S60$-0.15.

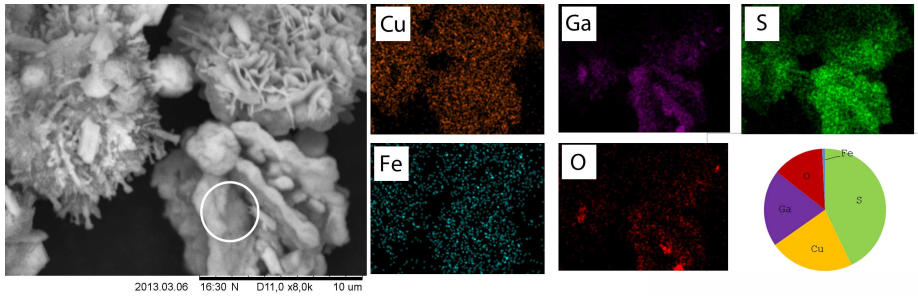

Figure B.3: Irregular sphere-like structures of $CuGaS_2$. The image is taken from sample $CG_{0.9}F_{0.1}S42$-0.03.